Computational Modeling of Oxidation Catalysis

Studies concerning Fenton's reaction

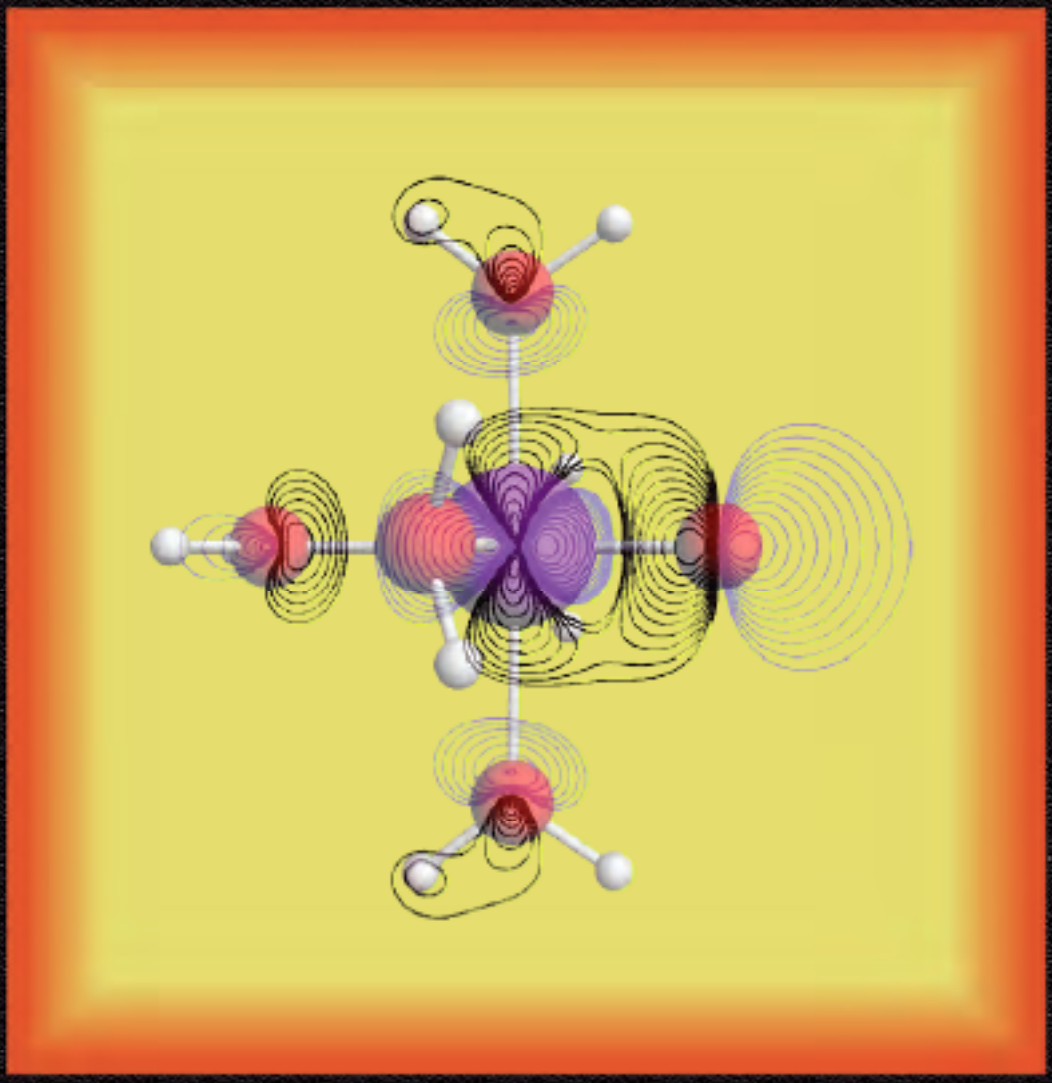

Manuel Louwerse

Computational Modeling of Oxidation Catalysis
Studies concerning Fenton's reaction.
Manuel Louwerse
ISBN: 978 90 8659 209 8
2008

Printed by Printpartners Ipskamp, Enschede

Cover illustratie: *De $3\sigma^{*\uparrow}$ orbitaal van het $[FeO(H_2O)_5]^{2+}$ deeltje. Dit deeltje is het actieve deeltje in de Fenton reactie. Het hoofdresultaat van dit proefschrift is dat de reactiviteit van dit deeltje bepaald wordt door de eigenschappen van zijn $3\sigma^{*\uparrow}$ orbitaal. Zie Hoofdstuk 5 en 6.*

VRIJE UNIVERSITEIT

Computational Modeling of Oxidation Catalysis

Studies concerning Fenton's reaction

ACADEMISCH PROEFSCHRIFT

ter verkrijging van de graad Doctor aan
de Vrije Universiteit Amsterdam,
op gezag van de rector magnificus
prof.dr. L.M. Bouter,
in het openbaar te verdedigen
ten overstaan van de promotiecommissie
van de faculteit der Exacte Wetenschappen
op dinsdag 27 mei 2008 om 13.45 uur
in de aula van de universiteit,
De Boelelaan 1105

door

Manuel Jan Louwerse

geboren te Gouda

promotor: prof.dr. E.J. Baerends

Computational Modeling of Oxidation Catalysis

Studies concerning Fenton's reaction

Manuel Louwerse

Beoordelingscommissie:

prof.dr. M. Sprik
prof.dr. M. Filatov
prof.dr. F. Neese
dr. F. Buda
dr. B. Ensing

Dit onderzoek werd financieel mogelijk gemaakt door de National Research School Combination Catalysis Controlled by Chemical Design (NRSC-Catalysis).

Contents

Introduction

Modeling of the Fenton reaction

Once upon a time, in 1876, H.J.H. Fenton discovered the reaction of hydrogen peroxide (H_2O_2) and ferrous ions (Fe^{2+}) in water with tartaric acid ($C_4H_6O_6$).[1] Later, it was found that this combination of hydrogen peroxide and ferrous ions can oxidize most organic compounds, via a catalytic process in which Fe^{2+} is the catalyst and H_2O_2 the reactant. This reaction has become known as the Fenton reaction.

The Fenton reaction is a very elegant and environmentally friendly reaction because it can be performed in water, at ambient temperature, and the only side product is water. For that reason it is used in a broad range of industrial applications, like oxidation of wastewater,[2,3] the hydroxylation of aromatic substrates,[4] and many other applications. On the other hand, Fenton's reagent is very unspecific, and this makes it unsuitable as oxidant for specific local oxidations in the production of complex molecules. Development of new specialized catalysts based on Fenton's reagent but usable for specific oxidations would be a great accomplishment.

However, the mechanism of the Fenton reaction has been a matter of long-lasting debate[5-10] and is not exactly known nor understood, obviously slowing down further development. The main point of debate is whether $OH^{\bullet}$ radicals are responsible for the oxidation of the substrates, or that alternative intermediates are formed, like FeO^{2+}. The problem is that experimentally both $OH^{\bullet}$ and FeO^{2+} are very hard to observe, and the discussion relies on indirect evidence like reaction products and reaction rates.

Nowadays, questions that meet experimental difficulties, like recognizing the mechanism of a reaction, can also be studied using computer models. Details that are hard or even impossible to observe in experiment may be straightforwardly clear in a computer simulation, and experiments that cannot be conducted in reality, for a variety of reasons, may be easily done in the computer. Computer modeling is more and more becoming a useful additional tool for chemical research. In fact, we are approaching the point that useful molecules, materials, or chemical processes may be designed completely in the computer.

Subjects in chemistry for which computational modeling is especially widely used are drug design, catalysis, and spectroscopy. In drug design, detailed knowledge of the structure of proteins and their interactions with drugs are crucial in order to design new drugs; in spectroscopy, modeling is actually the only way to interpret the spectroscopic results; and also in catalysis there is a large need for modeling, because the intermediates usually are short-lived and hard to identify experimentally.

When doing molecular modeling, several types of models can be used. In general, one can choose between Molecular Mechanics (MM) or Quantum Mechanics (QM)

models. Obviously, this depends on the process under study: When the studied process only involves molecular interactions in which no chemical bonds are broken or formed, usually a MM model suffices. But when more complex interactions (like in the presence of metals) or chemical reactions are involved, the use of a QM model is required.

Furthermore, one can study a system in vacuum or include the environment of the system in the model. When the environment may influence the process under study (as often is the case), this needs to be incorporated as well. In some cases, it suffices to use an implicit continuum model, but when the influence of the environment occurs through specific molecular interactions, an explicit model is needed, which can again be an MM (in combination with a QM model for the central system this is called QM/MM) or a QM model (thus resulting in a full QM description of the system and its environment). In fact, all combinations of these techniques are regularly used, depending on the type of systems studied.

When modeling the Fenton reaction, we realize that chemical bonds are broken and formed and metal ions (iron) are involved, so clearly a QM model is required. The environment of the Fenton reaction is a water solution, and because radicals are involved, it can be expected that the water molecules will actively participate in the reaction, also forming and breaking bonds. Therefore, it will be necessary to describe the complete system plus water solution in a full QM model. Note that modeling of a solution is done by modeling only a very small portion of it and repeating this "simulation cell" periodically, thus preventing finite size effects without having to model large amounts of water molecules. A common setup to study such a system with QM is using Density Functional Theory (DFT)[11,12] combined with Car-Parrinello Molecular Dynamics.[13]

Using these techniques, Ensing et al.[14-17] have modeled the Fenton reaction focusing on the first steps of the process, the formation of $OH^{\bullet}$ radicals or FeO^{2+} ions. They found that when H_2O_2 approaches Fe^{2+}, it breaks into two OH fragments: an $OH^{\bullet}$ radical and an OH^{-} ligand (this is an $OH^{\bullet}$ with an additional electron from iron, forming $[Fe^{III}OH]^{2+}$), but within 100 fs the unbound $OH^{\bullet}$ reacts further with the $FeOH^{2+}$, ultimately forming FeO^{2+}. This second step occurs either directly or via a short H-bond chain through the water solution. Their conclusion is that the $OH^{\bullet}$ formed is not what one would call a "free" $OH^{\bullet}$ radical that can oxidize organic substrates, but the active intermediate of the reaction must be the FeO^{2+} ion that follows immediately.

Going back to the debate on the mechanism of the Fenton reaction: The simulations of Ensing et al. confirm that, as a first step, $OH^{\bullet}$ radicals are formed, but they also show that they immediately react further to FeO^{2+}, which is thus allegedly the real active intermediate in the Fenton reaction (at least in water). At this point, the questions remain how exactly FeO^{2+} reacts with the organic substrates and whether the catalytic cycle is closed by that reaction (i.e. is Fe^{2+} regained to attack another H_2O_2 molecule?).

This thesis

In this thesis we elaborate on the simulations of Ensing et al. We study the behavior of a free $OH^{\bullet}$ radical in water and, comprising the main part of this thesis, the reaction of FeO^{2+} with organic substrates. For the reaction of FeO^{2+} with methanol different mechanisms are compared, and, subsequently, the electronic structure of FeO^{2+} is studied in detail. Finally, we try to understand the effect of the surrounding ligands on the reactivity of FeO^{2+}, and we will present handles to control the reactivity of this compound. The ultimate goal (outside the scope of this thesis) is to open the way to development of specialized catalysts for specific oxidations based on Fenton's reagent or, in fact, on the FeO^{2+} species.

In Chapter 1 of this thesis, we summarize the debate on the active intermediates in the Fenton reaction. We try to order the vast amount of literature on the subject and we will discuss that the debate may converge more quickly if authors would realize that possibly different mechanisms are active under different reaction conditions. We think experiments should focus more on understanding the conditions that determine the mechanism.

In Chapter 2, some technical aspects are discussed for the Car-Parrinello simulations as presented in Chapters 4 and 5. We discuss the sensitivity of Car-Parrinello simulations to too large fictitious masses, and we introduce new settings. We discuss the Projector Augmented Wave (PAW)[18,19] method, which we use to enable modeling of the iron ions, and again we introduce alternative settings. Finally, we explain why –unfortunately– the pressure cannot be calculated in a straightforward manner in Car-Parrinello simulations.

In Chapter 3, we present simulations of the $OH^{\bullet}$ radical in water solution. An interesting hemibonded structure is found in these simulations, and we discuss the consequences of this structure on the diffusion of an $OH^{\bullet}$ radical in a water solution.

In Chapter 4, we proceed to the reaction of FeO^{2+} with methanol. Gas phase calculations with $[FeO(H_2O)_5]^{2+}$ are combined with Car-Parrinello simulations with solvated FeO^{2+} to thoroughly study all possible mechanisms for this reaction. Some interesting results are obtained in these simulations, but also there is a striking difference in the height of the barriers between the gas phase calculations and the simulations in solution.

In Chapter 5, the electronic structure of $[FeO(H_2O)_5]^{2+}$ is studied and the forementioned difference between gas phase and solution in our specific case is examined. We conclude that the difference is caused by a shift of the one orbital that directs the reactivity of FeO^{2+} (the $3\sigma^*$ orbital), and modeling the solvent with a continuum model, we reproduce the shift of that orbital and the higher reaction barriers found in the simulations.

Finally, in Chapter 6, we discuss how the equatorial ligands control the spin state of FeO^{2+} complexes, and how the axial ligand makes the $3\sigma^*$ orbital shift, thus directly changing the reactivity of the complex. With the understanding of the solvent and the ligand effects, we come one step closer in understanding the reactivity of FeO^{2+}

complexes and in controlling the reactivity of these complexes, hopefully ultimately accelerating the development of new environmentally friendly catalysts based on FeO^{2+} complexes.

1.

The mechanism of the Fenton reaction

Abstract:

Although the Fenton reaction was discovered as early as in 1876, the debate on the mechanism of the Fenton reaction is lasting still. In the early 1930s two possible mechanisms were proposed, one with $OH^{\bullet}$ and one with FeO^{2+} as active intermediate. Ever since, many arguments have been raised to affirm either of the two mechanisms. However, on many arguments counterarguments have been raised and the resulting literature is rather chaotic.

In this chapter, we give an overview of the arguments and counterarguments that are around, and we discuss that the situation may be easier understood when it is realized that the mechanism may be different for different reaction conditions. Many variables that may determine the mechanism have been identified, and it is stressed that experiments should be focused on finding the conditions that determine the different mechanisms rather than on proving a general reaction mechanism that does not exist.

1.1. Introduction

As early as in 1876, H. J. H. Fenton discovered the reaction of Fe^{2+} and H_2O_2 with tartaric acid.[1] Only in 1894 he managed to identify the product: dihydroxymaleic acid.[20] Any understanding of the mechanism was out of reach at the time.

In the early 1930s, the first mechanisms for the Fenton reaction were proposed, purely based on the reaction kinetics and guessing. These mechanisms were based on the reaction of Fe^{2+} with H_2O_2 producing O_2, and it was assumed that the same intermediates should be responsible for the oxidation of organic substrates, when added. Haber and Weiss[21] proposed the production of $OH^{\bullet}$ radicals followed by autocatalysis:

$$Fe^{2+} + H_2O_2 \rightarrow Fe^{3+} + OH^- + OH^{\bullet} \quad (1.1)$$

$$OH^{\bullet} + H_2O_2 \rightarrow HO_2^{\bullet} + H_2O \quad (1.2)$$

$$HO_2^{\bullet} + H_2O_2 \rightarrow O_2 + OH^{\bullet} + H_2O \quad (1.3)$$

Bray and Gorin,[22] on the other hand, proposed formation of FeO^{2+}:

$$Fe^{2+} + H_2O_2 \rightarrow FeO^{2+} + H_2O \quad (1.4)$$

$$FeO^{2+} + H_2O_2 \rightarrow Fe^{2+} + H_2O + O_2, \quad (1.5)$$

combined with an additional equilibrium to explain the presence of Fe^{3+}:

$$Fe^{2+} + FeO^{2+} + 2H^+ \leftrightarrows 2Fe^{3+} + H_2O \quad (1.6)$$

In 1951, Barb et al.[23] improved the scheme of Haber and Weiss by reintroducing iron into the catalytic cycle, reasoning from the fact that reaction 1.3 was found not to occur.[8,24] Apart from side reactions of the radicals with Fe^{2+} forming additional Fe^{3+}, their reaction scheme was:

$$Fe^{2+} + H_2O_2 \rightarrow Fe^{3+} + OH^- + OH^{\bullet} \quad (1.1)$$

$$OH^{\bullet} + H_2O_2 \rightarrow HO_2^{\bullet} + H_2O \quad (1.2)$$

$$Fe^{3+} + HO_2^{\bullet} \rightarrow Fe^{2+} + O_2 + H^+ \quad (1.7)$$

For sufficiently high concentration of Fe^{3+} relative to the concentration of H_2O_2, Barb et al. also considered formation of FeO^{2+} to be likely:

$$Fe^{3+} + OH^{\bullet} \rightarrow FeO^{2+} + H^+ \quad (1.8)$$

$$FeO^{2+} + H_2O_2 \rightarrow Fe^{2+} + H_2O + O_2 \quad (1.5)$$

But because the latter reactions lead to the exact same kinetics as reactions 1.1, 1.2, and 1.7, the formation of FeO^{2+} could not be proven nor disproved. For the reaction with

organic substrates, though, still the $OH^{\bullet}$ radical was considered to be the active species.[25]

In the decades following these first attempts to understand the mechanism of the Fenton reaction, a large debate grew on what should be the correct mechanism: substrate oxidation by $OH^{\bullet}$ or by FeO^{2+}, and incidentally other intermediates were considered as well. During that debate, also other oxidants like HOCl, ROOH, and ROOR (combined with Fe^{2+}) and other solvents than water were brought into the equation and referred to as Fenton chemistry, assuming identical chemistry. Many examples were produced that supposedly proved wrong either one of the mechanisms, feeding the discussion for a long time. Many reviews of the discussion can be found in Refs. 5,6,9,10,26-31 and references therein. In some of these papers also Gif chemistry[32,33] (Fe^{3+} + H_2O_2 or related compounds + certain additives) is discussed, but for these reagents it is well accepted that the reaction proceeds via other intermediates than the Fenton reaction (probably via $FeOOH^{2+}$, possibly followed by formation of FeO^{3+}). We will not include the Gif chemistry in our discussion.

Actually, the literature on the Fenton reaction is rather chaotic. As mentioned above, different combinations of oxidants, solvents, and other reaction conditions have been discussed and compared as if they all react via the same unique mechanism, either via $OH^{\bullet}$ or via FeO^{2+}. Although some authors hint that different mechanisms may prevail under different reaction conditions, many authors tend to combine data from very different experiments as if they should be comparable, which usually is not the case. Because different authors often neglect different variations in the reaction conditions, collection of data from the literature becomes a very delicate task. To add to the confusion, there is a lot of discussion on the interpretation of experiments. While some authors state that in a certain experiment one or the other mechanism has been proven or disproved, other authors point out that the results leave room for alternative interpretations or even that the argument is plainly incorrect. Taken together, the literature on the Fenton reaction is quite chaotic and it is hard to make a clear picture out of it.

In the next section, it is tried to give a short overview of the main arguments and counterarguments that have been put forward in the debate. However, in most cases the conclusion will be that nothing has been proven or that chaos is still reigning, rather than that any real conclusions can be drawn.

1.2. Arguments for either mechanism

A first argument in favor of $OH^{\bullet}$ concerns experiments with 5,5-dimethyl-1-pyrroline-*N*-oxide (DMPO) or other so-called radical scavengers. These molecules react very quickly with freely diffusing radicals and the products of the reaction depend on the radical at hand. Several Fenton reagents have been found to react with DMPO producing the same adducts as $OH^{\bullet}$ does, supposedly proving the presence of $OH^{\bullet}$ radicals in Fenton reagents. A much referenced article is the work of Yamazaki and Piette.[34] However, as Goldstein et al.[28] and Halliwell et al.[27] point out, there is no

reason why FeO^{2+} could not react with these radical scavengers as well and produce the same adducts. As long as the reaction of FeO^{2+} produced from e.g. Fe^{2+} and ozone[35] with radical scavengers is not tested, nothing has been proven here.

The same experiment has also been performed with isotope labeled hydrogen peroxide.[36,37] It was shown that all oxygen atoms built into DMPO were labeled isotopes and thus originating from H_2O_2 and none from H_2O. This result has recently been cited by Pignatello et al.[31] as proof of $OH^{\bullet}$ formation, but Lloyd et al. themselves[36] and also Wardman et al.[5] point out that this is not at all a proof that FeO^{2+} is not involved. Interestingly, when *t*-BuOOH is used as reagent under 1 atm. O_2, all incorporated oxygen atoms seem to originate from O_2,[29] illustrating that the mechanism can be different for different "Fenton" reagents or can even be changed by the presence of molecular oxygen.

Another argument for the presence of radicals is the initiation of vinyl polymerization by Fenton reagents.[25] Although this is a clear proof that carbon radicals must be produced by the reaction with Fenton reagents, it does not mean that $OH^{\bullet}$ radicals need to be involved; reaction with FeO^{2+} can produce carbon radicals as well.[30,38,39]

An argument generally in favor of FeO^{2+} concerns reaction products. It is known that H_2O_2 irradiated by UV produces $OH^{\bullet}$, and by doing this in the presence of organic substrates, the products of reaction with $OH^{\bullet}$ can be obtained. For most organic substrates, reaction with a Fenton reagent produces the same products, but for some substrates different products have been obtained with the Fenton reagent, supposedly proving that the active intermediate cannot be $OH^{\bullet}$. However, this line of reasoning has been warned against by Halliwell et al.,[27] Goldstein et al.,[28] Walling,[38] and others, because secondary reactions and different steady state concentrations of the intermediates can cause different products to be formed,[28] and intermediate carbon radicals can also be oxidized or reduced by the metal ions, also causing the formation of different products.[27,38]

One example of differing products is the oxidation of cyclohexane. In the case of $OH^{\bullet}$, bicyclohexane dimers are the main product, while Fenton reagents produce cyclohexanol or cyclohexanon, thus suggesting that the active intermediates of these Fenton reagents cannot be $OH^{\bullet}$.[29] This experiment was alternatively explained as Fe^{3+} ions oxidizing the intermediate cyclohexane radicals; therefore, the absence of $OH^{\bullet}$ radicals was not proven by this experiment.[38]

Another example is the oxidation of 2,4–dimethylaniline in aqueous solution.[40] While oxidation by H_2O_2/UV lead to the formation of several hydroxylated aromatic amines, Fenton reactions mainly produce 2,4–dimethylphenol (specific attack of the amine group). It seems that this article has not been criticized and apparently has been accepted as proof against $OH^{\bullet}$ for the aqueous Fenton system.

The argument of differing products has also been used against FeO^{2+}, by Pestovsky et al.[41] The oxidation of $(CH_3)_2SO$ (DMSO) by FeO^{2+} produced from Fe^{2+} and ozone gives different products than oxidation of DMSO by the aqueous Fenton reagent, thus suggesting that the active intermediate in the Fenton reagent cannot be FeO^{2+}. In this

case, this conclusion has been overthrown by Kremer, who argues that the steady state concentration of FeO^{2+} is much higher in the ozone system than in the Fenton system causing the different products to be formed.[42]

Other, more divers arguments either way have been forwarded in the literature, as well. For instance, Dunford[6] and Sawyer et al.[29] mention that Fenton reagents are not powerful enough to oxidize methane, while $OH^{\bullet}$ does react with methane. However, in aqueous solution at pH = 2 oxidation of methane by a Fenton reagent has been reported,[10,43] disqualifying this argument against $OH^{\bullet}$.

Already in 1965,[44] and repeated in 2006,[41] it has been argued that while a mixture of Fe^{2+} with HOCl or O_3 produces $(FeOH)_2^{4+}$ (an instable dimer product of FeO^{2+} and Fe^{2+}), this is not produced by Fe^{2+} mixed with H_2O_2. This would suggest that in the latter mixture no FeO^{2+} is formed. However, Kremer argues that this is again a matter of lower steady state concentrations: HOCl and ozone react much faster with iron than H_2O_2 does, thus causing higher steady state concentrations of FeO^{2+} and $(FeOH)_2^{4+}$. The mixture with H_2O_2 can still produce FeO^{2+}, but because this reaction is orders of magnitude slower, the concentration of $(FeOH)_2^{4+}$ becomes too low to be observed.[42]

Walling has forwarded an interesting argument against FeO^{2+} stating that the reaction rates are unaffected by increasing ionic strength, implying that the active intermediate cannot be a charged species.[26,38,45] He explains that reactions between ions and neutral species are unaffected by ionic strength, but reactions between ions of alike charge are accelerated. He argues that the rate of Fe^{2+} ions being oxidized in a Fenton reaction is unaffected by the ionic strength, and thus the active intermediate cannot be a charged species. Of course, it should be kept in mind that most Fe^{2+} is oxidized by neutral H_2O_2. Unfortunately, Walling does not give much detail on how the relative rates were calculated, nor the concentration of RH, the organic substrate, and it is unclear why the Fe^{2+} not accounted for by H_2O_2 could not be oxidized by $R^{\bullet}$, and why oxidation of Fe^{2+} by the "active intermediate" should give a significant effect at all.

Some authors[10,29,31] have forwarded arguments involving the kinetic isotope effect (KIE), the ratio between reaction rates with substrates containing hydrogen or deuterium isotopes. When hydrogen/deuterium abstractions occur in a rate-determining step, a KIE of around 5–7 is to be expected. When no hydrogen abstractions occur or when they are not rate-determining the KIE is 1, or close to 1. The argument that is used is that with very reactive intermediates (like $OH^{\bullet}$) hydrogen abstraction will not be rate-determining and the KIE should be 1, and higher values for the KIE means that the hydrogen abstraction step is rate-determining and the intermediate must be a less reactive species (like FeO^{2+}).[10] However, most KIE values reported for Fenton-type reactions are in between 1 and 5–7, which means that the hydrogen abstraction step is only partly rate-determining; formation of the reactive intermediate or diffusion are also rate-limiting (or several intermediates are taking part at the same time). As a result, subtle changes in reaction conditions can easily change the balance of formation,

diffusion, and reaction, and are bound to influence the KIE value observed, weakening kinetic isotope effect arguments severely.

Finally, perhaps the most convincing argument in favor of FeO^{2+} as the active intermediate in Fenton reactions is conveyed by Groves.[9] He claims that oxidation of cyclohexanol and 7-hydroxynorbornane by a Fenton reagent was found to be regioselective and stereoselective. This cannot be explained if the active intermediate should be $OH^{\bullet}$, but it can be explained by metal–alcohol complexation in case of an iron-containing intermediate like FeO^{2+}. Therefore, at least for the reagent used by Groves, the active intermediate must contain iron and cannot be $OH^{\bullet}$.

Actually, advanced kinetics studies have shown that in the aqueous Fenton system two different active intermediates may be involved concurrently. Interestingly, to fit the kinetics data properly, both intermediates cannot be $OH^{\bullet}$.[30,46]

1.3. Discussion

In the previous section, the arguments for $OH^{\bullet}$ or FeO^{2+} were still discussed in a general way, as if one mechanism must be correct and the other incorrect for all or most reaction conditions. However, the picture emerging from such a discussion is confusing, with many arguments being put in doubt and other arguments leading to contradictory conclusions. A better way of looking at the situation is by realizing that most probably different mechanisms are acting in different cases. Experiments should be focused on finding the conditions that determine the different mechanisms rather than on proving a general reaction mechanism that does not exist.

Some authors of review articles have realized that the formation of $OH^{\bullet}$ or FeO^{2+} may depend on the concentrations of reactants, radical scavengers, and pH[28], or on the nature of ligands, solvents, and substrate.[10] Wardman et al. add the notion that the presence of coordinated water on the metal ion is probably an important factor for the choice of mechanism,[5] and also Kremer warns that for identifying the intermediates in his kinetics study, experiments with different reaction conditions have an uncertain value.[30] Nevertheless, the discussion still is polarized and little agreement has been reached yet.

We give a few examples of important reaction conditions that certainly influence the mechanism and can easily be overlooked. The first one is the presence of molecular oxygen. It is known that molecular oxygen increases the oxidative strength of Fenton reagents; apparently an additional mechanism is active when reactions are performed under air.[29,31] Sawyer et al. very cleverly add that systems with excess H_2O_2 produce their own oxygen atmosphere, and the mechanism may change during the reaction.[29] Another example is the presence of light. Of course it is common knowledge that UV breaks down H_2O_2 into 2 $OH^{\bullet}$ and can photo-enhance Fenton reactions, introducing additional mechanistic pathways. But Pignatello et al.[31] report that photo-enhancement will be observed even in the presence of ordinary overhead fluorescent light used to illuminate laboratory space, possibly complicating the interpretation of many experiments.

Table 1.1 *O_2 evolution for different Fe^{2+}/Fe^{3+} to H_2O_2 ratios in water and in acetonitrile. Adapted from Ref. 47.*

		Number of moles O_2 found per mol of H_2O_2 (n_{O_2} / $n_{H_2O_2}$)				
Solvent	Iron source	[Fe]/[H_2O_2]:	4/1	2/1	1/1	1/10
H_2O	$Fe^{II}(ClO_4)_2$		0.04	0.04	0.34	0.46
	$Fe^{III}(ClO_4)_3$		0.44	0.50	0.50	0.49
MeCN	$Fe^{II}(ClO_4)_2$		0.28	0.36	0.38	0.17
	$Fe^{III}(ClO_4)_3$		0.92	0.92	0.61	0.14

Overall, there are quite some variables that may influence the mechanism, namely the concentrations of Fe^{2+}, the oxidant, and the substrate, the nature of the oxidant (H_2O_2, HOCl, ROOR, etc.), the solvent, the pH, the nature of ligands, the presence of O_2, light, the presence of other chemicals, and the nature of the substrate. All of these variables should be handled carefully and systematically if one wishes to make any progress in the understanding of the mechanisms of different Fenton reagents.

A very nice example of an article in which the researchers did approach the subject in a systematic manner is the work of Paczésniak and Sobkowiak.[47] They performed cyclovoltametric experiments with mixtures of Fe^{2+} with H_2O_2 and Fe^{3+} with H_2O_2 in different concentrations and solvents, and they measured precisely the amount of oxygen that evolved from the reactions. Their results are gathered in Table 1.1, which has been copied from Ref. 47. In Table 1.1, the amount of molecular oxygen produced per degraded mol of hydrogen peroxide is given. The amount of degraded H_2O_2 that is not accounted for by produced O_2 is consumed by net oxidation or reduction of iron ions. For example, for Fe^{2+} and H_2O_2 in water, it can be seen that at high concentrations of Fe^{2+} the reactive intermediates attack the Fe^{2+} ions (hardly any O_2 is produced) and at high concentrations of H_2O_2 the reactive intermediates attack the H_2O_2 molecules (every H_2O_2 molecule produces 1/2 O_2 + H_2O). However, for Fe^{3+} or, more importantly, in acetonitrile, the situation is completely different, and it is clear that there must be different mechanisms active.

The explanations Paczésniak and Sobkowiak come up with are still rather uncertain, but at least they provide good systematic data. When more of such systematic work were done and added to their results, the conditions that determine the mechanism and the mechanisms themselves may become much clearer for the different Fenton reagents.

Finally, we discuss some simulations of free Fe^{2+} with H_2O_2 in water, the original Fenton reagent, performed by Ensing et al.[14-17] In their simulations, they found that at coordination of H_2O_2 to Fe^{2+} first an $OH^{\bullet}$ radical is formed. However, the energy it costs to break the O–O bond is more than the energy released by the formation of the Fe–OH bond. As a result, the produced $OH^{\bullet}$ radical is not a free radical but stays bound to the $FeOH^{2+}$ complex just formed. Consequently, the $OH^{\bullet}$ reattacks the iron center

and FeO^{2+} is formed. Apparently, in water solution and in the conditions modeled by Ensing et al., FeO^{2+} is the active intermediate and not free $OH^{\bullet}$.

Because $OH^{\bullet}$ is initially formed and its reaction with $FeOH^{2+}$ in some cases was observed to occur via short H-bond chains, the presence of a substrate or other changes in reaction conditions may influence the course of events and may cause the $OH^{\bullet}$ radical to act as a free reactant after all. Therefore, we have repeated one simulation of Ensing et al. and added respectively an H^{+} ion, a methanol molecule, and even a DMPO molecule to the water solution. In all three cases, the added molecules were ignored and the exact same thing happened: an $OH^{\bullet}$ radical was shortly formed and reattacked the $FeOH^{2+}$ to form FeO^{2+}. This behavior was actually anticipated by Kremer in 1999.[30] Kremer mentions that if $OH^{\bullet}$ can react with Fe^{3+}, it is plausible that the pair of Fe^{3+} and $OH^{\bullet}$ does not become separated at all but forms FeO^{2+} instead, and that is exactly what is found in the simulations.

Overall, it seems that for the original (aqueous) Fenton reaction the active intermediate is FeO^{2+}, but with different reaction conditions of any type matters may be different. These other conditions should be studied in a systematic way instead of adding more random experiments to the confusion that is present already. Also, some of the arguments listed in Section 1.2 should be further established, so that they can be used to differentiate between conditions that lead to one mechanism or the other.

Finally, we want to stress that the difference between the $OH^{\bullet}$ and the FeO^{2+} mechanisms is not necessarily a difference between a radical and a non-radical mechanism. Both in the formation of FeO^{2+} and in the reaction of FeO^{2+} with substrates radicals are temporarily formed and radical mechanisms may still occur subsequently or as a rare alternative, a warning that has also been expressed before.[38]

1.4. Conclusion

There has been a long-lasting debate on the mechanism of the Fenton reaction. In most literature discussing Fenton reagents it is assumed that in different systems resembling the original aqueous Fenton reagent the same active intermediate has to be present. However, considering the facts that have been found up to now, we think it is very likely that the mechanism will differ in different systems and under different reaction conditions. There are many variables that may determine the mechanism and approaching all Fenton systems as reacting via one general unique mechanism is not appropriate. The systematic work of Paczésniak and Sobkowiak confirms the presence of different mechanisms under different conditions, and more research should be done in such a systematic manner. More experiments should be focused on finding the conditions that determine the mechanism.

For the original Fenton reagent, that is aqueous solution of catalytic amounts of Fe^{2+} at low pH and mixed with hydrogen peroxide, however, we consider it likely that the active intermediate is FeO^{2+}. The simulations of Ensing et al. show that at first an $OH^{\bullet}$ radical is formed but that this reacts further to form FeO^{2+}. Therefore, further on, we consider FeO^{2+} to be the alleged intermediate in the Fenton reaction, meaning the original aqueous Fenton reaction. For other Fenton systems more research is needed.

2.

Technical aspects

Abstract:

In this chapter, some technical aspects for the simulations in later chapters are discussed. Improved Car-Parrinello parameters are introduced, the PAW method is discussed and projectors are optimized, and a derivation is given that explains why in Car-Parrinello simulations the pressure cannot be calculated with the virial equation for pressure.

It is well known that the fictitious mass parameter in Car-Parrinello simulations is very critical for quality and efficiency of the simulations. Recently, the fictitious mass parameter in liquid water simulations has been re-examined, and it was concluded that masses above 800 a.u. should not be used, limiting the timesteps to 5.5 a.u. Here, we show that small values like 100 a.u. are better to use, and, more importantly, that nevertheless large timesteps of 6.5 a.u. can be used.

The description of the electronic density close to the atomic cores has been augmented in our simulations using the Projector Augmented Wave (PAW) method. In principle, this method could be exact; in practice, the method proves to be approximate, and the choice of projectors influences the results. We have optimized sets of projectors for oxygen, hydrogen, carbon, and iron that give results that compare to all electron benchmark values within 8 kJ/mol.

Finally, because small deviations in the volume of a system in a condensed phase can have large effects on the pressure and thus on free energy differences in the system, the pressure in simulations of liquids should always be monitored and kept around the desired value. In classical simulations with pair-additive forcefields, the pressure would be calculated with the virial equation for pressure. However, we show that this equation is not correct for extended systems with periodic boundary conditions when non-pair-additive forces are used, as is the case in Car-Parrinello simulations.

2.1. Car-Parrinello parameters for the simulation of liquid water

The simulations presented in Chapter 3 and 4 have been performed with the Car-Parrinello method,[13] an advanced ab initio Molecular Dynamics (MD) method. In ab initio MD, classical Newtonian dynamics are calculated for the atomic nuclei using forces derived from ab initio electronic calculations within the Born-Oppenheimer approximation. In the Car-Parrinello method, expensive minimization of the electronic configuration for each timestep is circumvented by introducing fictitious Newtonian dynamics for the electronic variables, so that the electrons are able to follow the atomic nuclei and stay on the Born-Oppenheimer surface. Some theory and foundation for the Car-Parrinello method is given in Ref. 48.

In order to define the electronic Newtonian dynamics, a fictitious mass, μ, is introduced and associated to the wavefunction coefficients, which determines the acceleration of these coefficients due to the forces acting on them. The main challenge in performing Car-Parrinello simulations is to find good values for the fictitious mass, μ, and the timestep, Δt, to optimize the efficiency while still guaranteeing correct results: It is important that the electronic configuration stays close to the Born-Oppenheimer surface, implying that the (fictitious) temperature of the wavefunction coefficients should be as low as possible, and, therefore, the electronic dynamics should not be energetically coupled to the atomic dynamics. Small values for the fictitious mass prevent such coupling but also require small timesteps –in order to ensure correct time integration–, making the simulations inefficient. Larger fictitious masses and timesteps increase the efficiency, but a too large fictitious mass causes coupling to the atomic dynamics, and leads to large artifacts and incorrect results.

The optimum value for the fictitious mass depends on the mass of the lightest atoms in the system and the band gap of the system.[48] Traditionally,[49-54] for liquid water (with the hydrogen atoms replaced by deuterium atoms to increase the smallest mass) fictitious masses were used ranging from 900 to 1100 a.u. with corresponding timesteps of 6 to 7 a.u. However, recently it was shown that these values for the fictitious mass are too high and lead to deviations in the structure and increased diffusion.[55] In Ref. 55 it is suggested that for pure water the ratio μ/M (M being the mass of the lightest atoms in the system) should be at maximum 1/3 (resulting in $\mu \leq 650$ a.u. for D_2O). In Ref. 56, the situation was further investigated, and it was concluded that for values for μ up to 800 a.u. no significant errors caused by energetic coupling occur, provided that thermostats are used on both the atomic and electronic dynamics. The corresponding allowed timestep to simulate the electronic dynamics correctly is 5.5 a.u.

However, as put forward by Tangney,[57] there is another reason why the fictitious mass should be low: the (fictitious) weight of the electrons exhibits a drag on the nuclei, at best only scaling the atomic masses but in non-rigid structures also influencing structural and thermodynamic properties. Tangney writes: “It is as though the ions move through a viscous, inhomogeneous, and time-varying medium.” Note that in our simulations the mass of the atoms is corrected for the added weight of the

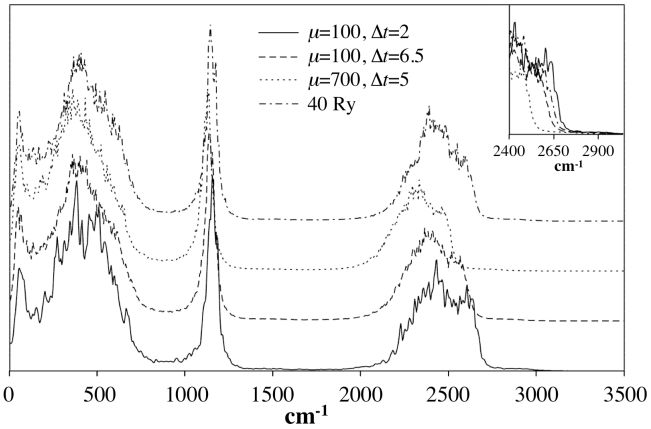

Figure 2.1 *Vibrational power spectrum for liquid D_2O of 300 K with varying Car-Parrinello parameters: μ = 100 a.u. and Δt = 2 a.u. (solid line), μ = 100 a.u. and Δt = 6.5 a.u. (dashed line), μ = 700 a.u. and Δt = 5 a.u. (dotted line), and one simulation with a cutoff of 40 Ry (and μ = 100 a.u. and Δt = 6.5 a.u.; dash-dotted line) instead of 30 Ry. In the inset graph, the O–D stretch region is drawn in one single y-axis in order to demonstrate the shift when μ = 700 a.u. is used.*

wavefunctions,[18] so the effects shown in the current section are purely caused by the inhomogeneous and time-varying nature of the drag.

Because of this drag effect, in our simulations, we have made a different choice of parameters than commonly used. The fictitious mass was chosen rather small, namely 100 a.u., but the timestep was nevertheless chosen to be 6.5 a.u. (0.157 fs.). This choice of parameters implies that the drag on the nuclei is minimized, but the electronic high frequency dynamics, associated with such a small fictitious mass, are not integrated correctly because of the large timesteps. We argue, though, that the electronic high frequency dynamics are of no importance other than to enable the electronic configuration to oscillate around the electronic ground state. The exact path of the electronic coefficients is not important, and, in fact, not physical anyway. In the current section, it will be shown that this choice of parameters gives correct simulations, and indeed gives better results than when larger fictitious masses (and smaller timesteps…) are used.

All simulations are performed with 32 D_2O molecules in a periodic box of 9.865 Å.

First, we have tested that despite the approximate integration of the electronic dynamics the total energy is conserved correctly: A simulation in the NVE ensemble was performed using the values μ = 100 a.u. and Δt = 6.5 a.u. In this simulation of 2 ps in length, the total energy was conserved within 0.005 a.u.

Next, in an NVT setup and over long 16-24 ps runs, our small mass and large timestep parameters were compared to more conventional parameters (Figure 2.1 and Figure 2.2). The simulation to beat is the one with μ = 700 a.u. and Δt = 5 a.u., parameters that have been generally agreed to give correct results for liquid water.[55,56]

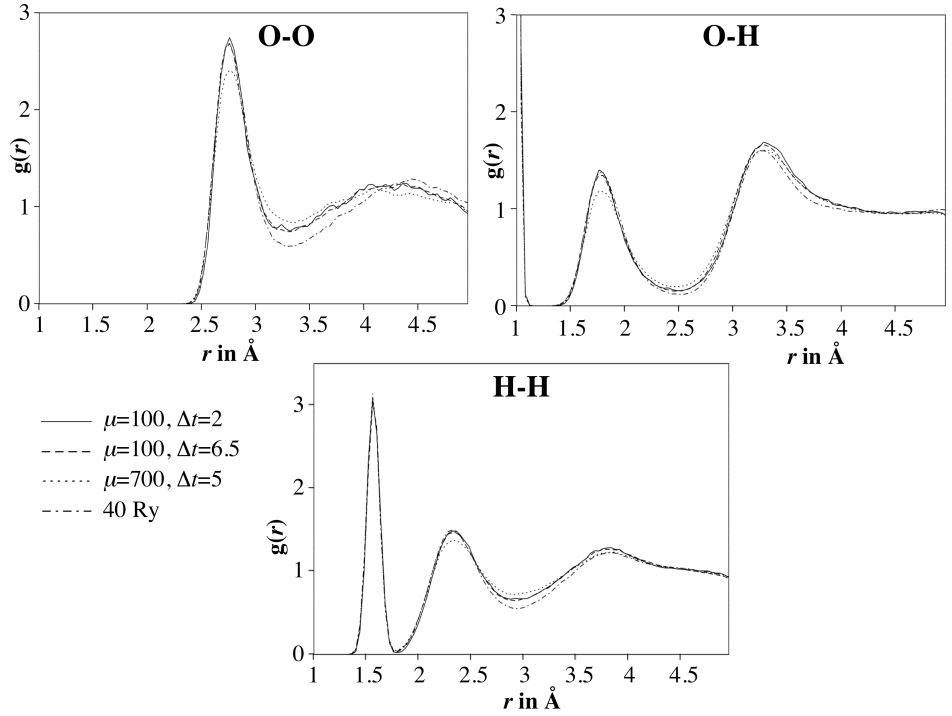

Figure 2.2 *Radial distribution functions for liquid D_2O of 300 K with varying Car-Parrinello parameters: μ = 100 a.u. and Δt = 2 a.u. (solid line), μ = 100 a.u. and Δt = 6.5 a.u. (dashed line), μ = 700 a.u. and Δt = 5 a.u. (dotted line), and one simulation with a cutoff of 40 Ry (and μ = 100 a.u. and Δt = 6.5 a.u.; dash-dotted line) instead of 30 Ry. The simulation with μ = 100 a.u. and Δt = 6.5 a.u. agrees perfectly with the benchmark Δt = 2 a.u. simulation.*

As a benchmark, we use a simulation with μ = 100 a.u. and Δt = 2 a.u., a simulation that should exhibit close to perfect atomic and electronic integration, but is, obviously, very inefficient; therefore, it was only pursued for 3 ps. Finally, a simulation was included with a plane wave cutoff of 40 Ry, whereas the other simulations had a cutoff of 30 Ry. This simulation was performed with the new parameters: μ = 100 a.u., Δt = 6.5 a.u. The plane wave convergence is discussed later in the text.

In Figure 2.1, the vibrational powerspectrum is shown for the four simulations mentioned. It is clear from this plot that in the simulation with μ = 700 a.u. the dynamics are altered by the drag exerted by the fictitious mass. The simulation with μ = 100 a.u. and Δt = 6.5 a.u., on the other hand, does agree closely to the benchmark simulation. The frequencies are slightly shifted as well, but much less than with the higher μ, while the simulation is more efficient.

In Figure 2.2, radial distribution functions (RDFs) are shown. For the μ = 700 a.u. simulation, again, small deviations are visible, whereas the μ = 100 a.u., Δt = 6.5 a.u. results agree perfectly with the Δt = 2 a.u. results. Focussing on the 40 Ry simulation

we also see some small differences, mainly in the minima of the RDFs. This suggests somewhat increased diffusion at 30 Ry as discussed below, but otherwise the interactions are correct (the first peaks are well reproduced). For the μ = 700 a.u. run, however, the deviations are in the first intermolecular peak (the first peak in the H–H RDF is the intramolecular H–H distance), suggesting that really the molecular interactions are corrupted by the drag of the electrons, even though just a little.

The important observation is that both the dynamics (Figure 2.1) and the structure (Figure 2.2) are perfectly reproduced in the simulation with μ = 100 a.u. and Δt = 6.5 a.u., showing that the use of small fictitious masses and relatively large timesteps give correct results and is a better way to perform Car-Parrinello simulations than with a larger fictitious mass, even when the fictitious mass is chosen such that there is no energetic (adiabatic) coupling.

Related to structure and dynamics is the self-diffusion of the water molecules. To obtain good statistics in simulations, it is important that there is enough diffusion and structures are not glass-like. It is known that diffusion is very sensitive to subtle variables like the fictitious mass, box size, DFT functionals, use of pseudopotentials, and temperature.[55,56,58] Experimentally, the self-diffusion coefficient of D_2O at 298 K is 0.19 Å^2/ps.[59] For water modeled with the BLYP functional, values have been found of 0.006 Å^2/ps at 300 K (with μ = 340 a.u.),[55] 0.06 Å^2/ps at 315 K (with μ = 400 a.u.),[56] and 0.05 Å^2/ps at 325 K (with Born-Oppenheimer MD).[58] The inconsistency between the latter two values has been explained by the fact that different types of pseudopotentials were used.[56]

In our simulations, a self-diffusion coefficient was found of 0.11 Å^2/ps at 300 K, both with μ = 100 a.u. and μ = 700 a.u. The length of the simulation with Δt = 2 a.u. (3 ps) is too short to get a proper diffusion coefficient (see also Ref. 55), but comparison with short parts of the Δt = 6.5 a.u. simulation suggests that the self-diffusion is equal in these two simulations. Thus, again, we observe that the simulation with Δt = 6.5 a.u. does not introduce any artifacts.

We note that the self-diffusion coefficient found is considerably higher than the literature values for simulations with the BLYP functional. This is caused by two factors: First of all, we do not use pseudopotentials but PAW projectors (see section 2.2). As noted above, the small effect of pseudopotentials is enough to alter the self-diffusion coefficient. Thus, it is no surprise that with the PAW projectors we find a different value. A priori, there is no reason to trust one method over the other; practically, in view of statistics, it is very convenient that we have a high diffusion rate.

The second factor causing relatively fast diffusion is that at 30 Ry the plane wave basis is not yet completely converged: In the 40 Ry simulation we find a somewhat lower self-diffusion coefficient of 0.07 Å^2/ps (at 300 K), as already predicted from the deeper minima in the radial distribution functions (Figure 2.2). With the PAW method the plane wave basis converges faster than with pseudopotentials, and at 40 Ry for the wavefunctions (and 120 Ry for the electron density) it is practically converged, as will be shown in Section 2.2. At 30 Ry (and 90 Ry for the electron density), the results are acceptable as well with only a slightly increased diffusion.

To conclude, we have observed that Car-Parrinello simulations can best be performed with a low fictitious mass and nevertheless large timesteps. We have shown that liquid heavy water modeled with μ = 100 a.u. and Δt = 6.5 a.u. reproduces a simulation with μ = 100 a.u. and Δt = 2 a.u. perfectly, while the commonly used mass, μ = 700 a.u., introduces small artifacts in vibrational frequencies and radial distribution functions.

In the simulations of FeO^{2+} and methanol in Chapter 4, the band gap becomes very small close to the reaction barrier, and it was necessary to increase the friction on the wavefunction coefficients in some simulations. Also in these simulations the vibrational power spectra for the water molecules of the solution agree with the spectra of Figure 2.1, proving our Car-Parrinello parameters to be robust.

2.2. The Projector Augmented Wave method

2.2.1. Introduction and theory

In Car-Parrinello simulations, usually plane waves are used as basis set to expand the DFT wavefunctions. Plane waves have the advantage of being computational very convenient and can describe the valence regions of the orbitals rather efficiently. For the regions close to the atomic nuclei, however, plane waves are not very efficient, because orbitals tend to exhibit rather strongly curved wiggles in these "core" regions (and cusps at the nuclei). Therefore, usually pseudopotentials are used to improve the efficiency for the core regions, however sacrificing a bit of quality.

An alternative method to enhance the plane wave expansion is the Projector Augmented Wave (PAW) method.[18,19] The PAW method is supposed to be more accurate than pseudopotential methods; however, as will be shown here, it suffers from similar problems. Nevertheless, the PAW method is the best option for modelling iron ions. In this section, we will explain the theory of the PAW method, including the origin of the fore-mentioned problems. Next, we will introduce a set of projectors specifically tested for our application.

Both in pseudopotential methods and in the PAW method, the true wavefunction, Ψ, is transformed to a pseudowavefunction, $\tilde{\Psi}$, that is much smoother so that it can be described with plane waves of lower energy. Next, $\tilde{\Psi}$ is optimized instead of Ψ, and the result is corrected for the transformation used: following Ref. 18, when the transformation from $\tilde{\Psi}$ to Ψ is called T, for any operator A, (including the Hamiltonian) a pseudo-operator, $\tilde{A}$, can be defined such that $\langle \tilde{\Psi} \mid \tilde{A} \mid \tilde{\Psi} \rangle = \langle \Psi \mid A \mid \Psi \rangle$:

$$\tilde{A} = T^{\dagger} A T \tag{2.1}$$

In pseudopotential methods, the pseudowavefunction is obtained by adding a potential to the Hamiltonian, such that the solutions of the Schrödinger equation for the new (pseudo-) Hamiltonian have the desired smooth character. The potential that gives this result is constructed using atomic all electron calculations. However, for adding arbitrary potentials to the Hamiltonian, no generally exact correction can be defined, and the corrections always are chosen based on certain reference systems (atoms or

specific molecules). As a result, these corrections are not exact for any other system than the reference system used. This is called the transferability problem of pseudopotentials.

For the PAW method, on the other hand, care is taken to define the transformation from Ψ to $\tilde{\Psi}$ such that the reverse transformation *is* well-defined.

In the PAW method, the true wavefunction, Ψ, is locally expanded in a set of so-called partial waves, $|\phi_i\rangle$, that are substituted by pseudo partial waves in order to obtain the pseudowavefunction $\tilde{\Psi}$:

$$\Psi = \sum_i c_i \phi_i \quad \text{within } \Omega_R \tag{2.2}$$

and

$$\tilde{\Psi} = \sum_i c_i \tilde{\phi}_i \quad \text{within } \Omega_R, \tag{2.3}$$

with identical coefficients c_i. Outside the augmentation region, Ω_R, the partial waves and the pseudo partial waves match exactly, so that the transformation only takes effect inside the augmentation region. Note that at this point a complete set of partial waves is assumed; the effect of using an incomplete set is discussed below.

Because the partial waves are not orthogonal, an additional set of local functions (with $\langle \tilde{p}_i | \tilde{\phi}_j \rangle = \delta_{ij}$) is needed to find the coefficients c_i, the so-called projector functions $\tilde{p}_i$:

$$c_i = \langle \tilde{p}_i | \tilde{\Psi} \rangle \tag{2.4}$$

Note that for each partial wave there is one pseudo partial wave and one projector function. The partial waves are constructed such that the true wavefunction expansion is efficient; the pseudo partial waves are constructed such that the pseudowavefunction is smooth; and the projector functions are constructed such that the correct coefficients c_i are found. In principle, the partial waves and pseudo partial waves are arbitrary functions; the way they have been constructed in practice can be found in Ref. 18. There, the partial and pseudo partial waves and projector functions are constructed as radial functions multiplied with spherical harmonics.

Now, the true wavefunction can be found from the pseudowavefunction by:

$$|\Psi\rangle = |\tilde{\Psi}\rangle + \sum_i \left(|\phi_i\rangle - |\tilde{\phi}_i\rangle \right) \langle \tilde{p}_i | \tilde{\Psi} \rangle, \tag{2.5}$$

and vice versa using the same coefficients c_i. This equation means that outside the augmentation region, Ψ is identical to $\tilde{\Psi}$, and inside this region, the pseudo partial waves are subtracted and substituted by the "true" partial waves (in the correct amounts as dictated by the coefficients c_i). Note that when the partial and pseudo partial waves do not form a complete set, a part of the (pseudo-) wavefunction is not covered by the expansions in partial and pseudo partial waves. This part of the wavefunction is thus not transformed but it is covered directly by the $|\tilde{\Psi}\rangle$ term in Equation 2.5.

For the calculation of the energy with a pseudo-Hamiltonian following Equation 2.1, we refer again to Ref. 18.

In Ref. 18, it is stressed that the PAW method is still exact when the partial waves do not form a complete set. As explained above, the part (*within* the augmentation regions) of the true wavefunction that is in that case not covered by the partial wave expansion just goes unaugmented into the $|\tilde{\Psi}\rangle$ term, which is expanded in the underlying plane wave basis set. Thus, for an infinite plane wave basis, the true wavefunction will converge to the exact result, irrespective of the partial waves and projectors used. For that reason, the precise choice of partial and pseudo partial waves is arbitrary, although, obviously, important for the efficiency.

However, in practice the plane waves are not included till infinity. The parts of the wavefunction that are in the valence regions or that are truly augmented, can easily be described with plane waves of a relatively low cutoff, but the part of the wavefunction that is in the augmentation region *and* that is missed by the augmentation due to the incomplete partial wave expansion will have similar wiggles and cusps as the true wavefunction itself. Therefore this part of the pseudowavefunction converges very slowly in terms of plane wave convergence.

At this point we have to conclude that the wavefunction does not converge towards the exact result properly: part of the wavefunction converges rather well as result of the augmentation, but the part that is missed by the augmentation follows much slower, even to such an extent that the results may appear converged while the "missed" part of the wavefunction is not even starting to become described. The point to which the wavefunction converges at first is thus strongly dependent on the set of partial waves and projectors that is chosen.

In order to correct for the effect of an incomplete set of partial waves, an additional potential $\bar{v}$ is introduced in the PAW method.[18] This $\bar{v}$ only enters the equation for the part of the wavefunction that is missed by the augmentation, and it is constructed as the difference between the potentials of augmented and all electron atomic calculations. However, just as for the pseudopotential methods, such a correction is only correct for the atomic reference system and incorrect for any other system; because of $\bar{v}$, also the PAW method is not transferable. Moreover: because of $\bar{v}$, the result for an infinite set of plane waves is not correct anymore, because it becomes doubly corrected (remember that the method *was* exact for an infinite plane wave basis).

Decreasing the effect of incomplete partial wave sets would better be done by simply using many more partial waves. In the current implementation, however, use of too many partial waves leads to instabilities due to overcompleteness problems, probably caused by the fact that neither the partial waves nor the pseudo partial waves are orthogonal. Imposing orthogonality for both the partial waves and the pseudo partial waves may solve the instability for large sets of partial waves. In my opinion, such an approach of increasing the partial wave sets would be better than the introduction of $\bar{v}$ in the current implementation.

2.2.2. Practical tests with several sets of partial waves and projectors

For our simulations with the PAW method, we take a pragmatic approach and vary the parameters until we at least obtain correct results for our applications. In the systems we study, many open shell and high-spin species occur, and for these systems some problems may arise when the default partial waves and projectors are used. Indeed, we find that with the default settings incorrect results are produced, when comparing with benchmark ADF[60-63] calculations. For that reason, we did extensive testing with different sets of partial waves and projectors until the results did agree acceptably with the benchmark calculations. Note that we do not claim that our sets of partial waves and projectors are transferable to other types of systems, but for our applications they can be trusted within the error reported in this section.

After describing the methods used for the testing, we will first show that different sets of partial waves indeed give different results, and then we will introduce the sets of partial waves for oxygen, hydrogen, carbon, and iron that we will use. In this section, the term projector is sometimes used for the triad of one partial wave, pseudo partial wave, and projector function.

The ADF benchmark calculations were all done with the largest basis set available (QZ4P), the ZORA[64] relativistic correction and without any frozen core. The basis set superposition error (BSSE) using this basis set is below 1.2 kJ/mol for the calculations in which iron is involved and below 0.2 kJ/mol when iron is not involved. All calculations were performed with the BLYP[65,66] functional.

For the construction of the partial waves and projector functions, we used the PAW atomic setups generation program distributed with the PAW software package. This program constructs the partial waves by radially integrating the Schrödinger equation at fixed values for the energy, for which the energy of atomic solutions can be used or any other value.[18] The parameters that can be varied for the construction of a new set of partial waves and projectors are the augmentation radius, a separate augmentation radius for the frozen core electrons, the number of partial waves per angular momentum, and the energy fixing each partial wave (also fixing the related pseudo partial wave and projector function). The number of partial waves per angular momentum is written in this section as, for example, 110, denoting that one partial wave is used for $l = 0$, one for $l = 1$, and zero partial waves for $l = 2$. For the energy values, we always first use the atomic energies of the valence electrons; only for higher partial waves the energy is reported (e.g. for hydrogen 200 only the energy of the second s partial wave is reported; the first s partial wave is constructed with the energy of the 1s orbital). Finally, there is an option in the PAW software to use only a subset of a previously constructed larger set of partial waves. However, because this option results in a different potential $\bar{v}$, we do not use it; the partial wave sets tested in the current section are meant for use without the subset option.

Because the ADF benchmark calculations are performed in vacuum, the PAW test calculations have also been performed in a vacuum setup: a periodic box of 10 Å was used in combination with a multipole correction to isolate the molecule from its periodic copies. For neutral polar molecules this method is found to be correct within

Table 2.1 *Plane wave Basis set convergence with different projector radii (in a.u.) for hydrogen and oxygen. Reaction energies in kJ/mol are given for the reaction $H_2O_2 \rightarrow 2\ OH^{\bullet}$. Different sets of projectors are clearly not converging to the same value. The benchmark energy for this reaction is 236.5 kJ/mol. The density cutoff is twice the wavefunction cutoff reported in the table.*

$H_2O_2 \rightarrow 2\ OH^{\bullet}$				
H:	100 r = 0.354, 0.454[a]	100 r = 0.3[b]	100 r = 0.5[b]	100 r = 0.8[b]
O:	110 r = 0.935, 1.035[a]	110 r = 0.8[b]	110 r = 1.0[b]	110 r = 1.3[b]
60 Ry	205.97	176.11	210.69	186.92
90 Ry	206.46	160.86	211.16	186.92
120 Ry	206.48	161.16	211.19	186.90
150 Ry	206.49	161.30	211.20	186.90

[a] Core radius and augmentation radius as copied from the default setups distributed with the software.

[b] The same value is used for the core and the augmentation radii.

0.1 kJ/mol for our reaction energies, and for species bearing a net charge within 1 kJ/mol. Finally, note that in a plane wave method, which the PAW method is, there is no basis set superposition error.

In Table 2.1, we show that different sets of partial waves can indeed give rather different results. These calculations are performed with minimal sets for hydrogen and oxygen, only using different radii. The unpleasant truth revealed in this table is that each series *seems* to converge well in terms of plane wave convergence, but the different series do not converge to the same point, with differences from the benchmark value of up to 70 kJ/mol! This is a clear example that the parts of the wavefunction (*within* the augmentation regions) that are missed by the augmentation cannot be described properly by plane waves, and the partial waves bias the results.

It should be mentioned here that the parameters used in Table 2.1 are a bit extreme, using only one p projector for oxygen. Adding one more p projector for oxygen makes the differences smaller, but does not solve the problem.

Constructing new sets of projectors, we reached acceptable results for hydrogen and oxygen when the default augmentation radii were scaled with a factor of 1.225, resulting in 0.557 a.u. for hydrogen and 1.267 a.u. for oxygen. The core radii were left to the default values (0.354 a.u. and 0.935 a.u., respectively). In Table 2.2, for these radii a comparison is made between different numbers of partial waves per angular momentum for oxygen, while for hydrogen the minimal set was used (H_100). The second p partial wave for oxygen was made as orthogonal to the first p partial wave as possible in the current software. To this effect, the optimal energy value for this partial wave was found to be 0.27777 a.u. Based on Table 2.2, the O_120 set with E_p = 0.27777 a.u. is selected; adding a third p projector or a d projector does not improve the results.

Table 2.2 *Comparison between several projector sets for oxygen using the new radii for oxygen and hydrogen. For hydrogen, the minimal set (H_100) is used. Reaction energies are given in kJ/mol and the density cutoff is twice the wavefunction cutoff.*

		O_110	O_120 (E_p=0)	O_120 (E_p=0.27777)	O_130 (E_p=0.27777, 2)	O_121 (E_d=0.5)	ADF
$H_2O_2 \rightarrow 2\ OH^\bullet$	40 Ry	207.1	236.7	236.8	236.6	241.3	
	60 Ry	206.5	236.0	236.1	236.5	240.7	236.5
	120 Ry	206.9	236.3	236.4	236.8	241.0	
$H_2O \rightarrow OH^\bullet + H^\bullet$	40 Ry	492.8	508.9	509.2	509.9	512.2	
	60 Ry	495.8	511.5	511.7	512.4	514.8	514.6
	120 Ry	496.3	511.9	512.1	512.8	515.2	
$H_2O–H_2O \rightarrow 2\ H_2O$	40 Ry		18.3	18.2	17.4	17.3	
	60 Ry		15.6	15.6	15.9	14.7	17.2
	120 Ry		15.7	15.7	15.9	14.8	

Table 2.3 *Comparison between PAW and ADF benchmark calculations in order to test the selected projector sets for hydrogen, oxygen, and carbon. Energies are given in kJ/mol, and the wavefunction and density cutoffs are 60 Ry and 120 Ry, respectively.*

	PAW	ADF	ΔE
$H_2O–H_2O \rightarrow 2\ H_2O$	15.6	17.2	–1.6
$HO^\bullet–H_2O \rightarrow H_2O + OH^\bullet$	24.5	29.4	–4.9
$H_2O_2 \rightarrow 2\ OH^\bullet$	236.1	236.5	–0.4
$H_2O_2 \rightarrow H^\bullet + OOH^\bullet$	359.9	367.2	–7.3
$H_2O \rightarrow H^\bullet + OH^\bullet$	511.7	514.6	–2.9
$OOH^\bullet \rightarrow H^\bullet + O_2$	226.8	221.6	5.2
$H_2 \rightarrow 2\ H^\bullet$	456.1	458.1	–2.0
$CH_3OH \rightarrow CH_3O^\bullet + H^\bullet$	440.4	444.4	–4.0
$CH_3OH \rightarrow CH_3O^- + H^+$	1601.8	1609.0	–7.2
$^\bullet CH_2OH \rightarrow CH_3O^\bullet$	33.5	31.4	2.1
$C_2H_6 \rightarrow 2\ CH_3^\bullet$	380.2	377.8	2.4
$CH_4 \rightarrow CH_3^\bullet + H^\bullet$	458.0	459.6	–1.6
$C_2H_6 \rightarrow C_2H_4 + H_2$	135.2	143.2	–8.0
$CH_3OH \rightarrow CH_2O + H_2$	99.8	99.3	0.5
$CH_3OH \rightarrow CH_4 + 1/2\ O_2$	111.1	109.5	1.6

For carbon the same recipe was followed to obtain a consistent set of partial waves: the default augmentation radius was scaled by 1.225, resulting in a radius of 1.33 a.u., the core radius was left at the default value of 0.991 a.u., and a C_120 projector set was constructed with E_p = 0.27777 a.u. Using these parameters, the same quality is obtained for carbon as for hydrogen and oxygen. In Table 2.3, a comprehensive set of reactions is tested that may be of importance for our calculations. The maximum deviation of the

Table 2.4 *Comparison between iron projector sets with different radii and numbers of partial waves per angular momentum. Energies are in kJ/mol and the density cutoff is three times the wavefunction cutoff. In brackets the differences with the ADF results are given.*

Setups		$[Fe(H_2O)_5]^{2+} + H_2O_2 \rightarrow [Fe(H_2O)_5OH]^{2+} + OH^{\bullet}$	$Fe^{2+} + 5\ H_2O \rightarrow [Fe(H_2O)_5]^{2+}$	$[FeH_2O]^{+}$ (S=1.5) $+ OH^{\bullet} \rightarrow [FeOH]^{+}$ (S=2) $+ H_2O$	$[FeH_2O]^{+}$ (S=2.5) $+ OH^{\bullet} \rightarrow [FeOH]^{+}$ (S=2) $+ H_2O$
r = 1.1, 1.5					
Fe_222 (E_p = 2.226) (E_d = 0.32717)	30 Ry	–29.7 (–11.6)	–1282.0 (–28.3)	–227.6 (+4.4)	–267.9 (+17.2)
	60 Ry	–35.7 (–17.6)	–1277.7 (–24.0)	–232.8 (–0.8)	–268.0 (+17.1)
Fe_323 (E_s = 1) (E_p = 2.226) (E_d = 0.32717, 2)	30 Ry	–30.2 (–12.1)	–1280.3 (–26.6)	–229.1 (+2.9)	–268.9 (+16.2)
	60 Ry	–35.8 (–17.7)	–1279.0 (–25.3)	–232.6 (–0.6)	–269.1 (+16.0)
r = 1.368, 1.468					
Fe_222 (E_p = 2.226) (E_d = 0.32717)	30 Ry	–33.7 (–15.6)	–1278.8 (–25.1)	–230.7 (+1.3)	–264.3 (+20.8)
	60 Ry	–33.2 (–15.1)	–1278.5 (–24.8)	–231.3 (+0.7)	–268.6 (+16.5)
Fe_323 (E_s = 1) (E_p = 2.226) (E_d = 0.32717, 2)	30 Ry	–34.2 (–16.1)	–1280.8 (–27.1)	–231.1 (+0.9)	–265.1 (+20.0)
	60 Ry	–33.6 (–15.5)	–1278.6 (–24.9)	–231.5 (+0.5)	–268.2 (+16.9)
r = 1.458, 1.658					
Fe_222 (E_p = 2.226) (E_d = 0.32717)	30 Ry	–26.5 (–8.4)	–1261.4 (–7.7)	–226.6 (+5.4)	–259.8 (+25.3)
	60 Ry	–24.9 (–6.8)	–1260.6 (–6.9)	–226.7 (+5.3)	–263.3 (+21.8)
Fe_223 (E_p = 2.226) (E_d = 0.32717, 2)	30 Ry	–27.4 (–9.3)	–1262.3 (–8.6)	–227.1 (+4.9)	–260.2 (+24.9)
	60 Ry	–25.4 (–7.3)	–1261.4 (–7.7)	–226.8 (+5.2)	–263.8 (+21.3)
Fe_323 (E_s = 1) (E_p = 2.226) (E_d = 0.32717, 2)	30 Ry	–28.0 (–9.9)	–1261.9 (–8.2)	–227.1 (+4.9)	–259.1 (+26.0)
	60 Ry	–25.6 (–7.5)	–1260.4 (–6.7)	–227.1 (+4.9)	–262.6 (+22.5)
r = 1.2, 1.85					
Fe_223 (E_p = 2.226) (E_d = 0.32717, 2)	30 Ry	–15.3 (+2.8)	–1243.9 (+9.8)	–220.0 (+12.0)	–256.3 (+28.8)
	60 Ry	–15.4 (+2.7)	–1241.6 (+12.1)	–222.8 (+9.2)	–257.6 (+27.5)
ADF (BSSE-corrected)		–18.1	–1253.7	–232.0	–285.1

PAW results from the ADF benchmark values for these reactions is 8 kJ/mol, with a root mean square deviation (RMSD) of 4 kJ/mol.

For iron the approach was a bit different. The default setups for iron use a frozen core with the 3s and 3p electrons included in the frozen core, while it is known that for first-row transition metals this should not be done. Therefore, we use a frozen core with only the 1s, 2s, and 2p orbitals frozen, and because using a smaller frozen core can be expected to affect the optimum augmentation radius, we did not just scale the radii with the same factor as before, but varied them again. We did tests for several choices of core radius, augmentation radius, and numbers of partial waves. The default radii for iron are 1.558 a.u. for the core radius and 1.658 a.u. for the augmentation radius.

Now that the 3s and 3p electrons are considered as valence electrons (along with the 4s and 3d electrons), the minimal set of projectors for iron is a Fe_211 set. For second p and d partial waves, we again maximized the orthogonality with the first p and d partial waves by tuning the energy value, resulting in the values of 2.226 a.u. and 0.32717 a.u., respectively.

In Table 2.4, the results are shown of the tests we did with different radii and numbers of partial waves. These tests include reaction of H_2O_2 with $[Fe(H_2O)_5]^{2+}$ (which changes the oxidation state of iron), solvation of Fe^{2+}, and a gas phase reaction of $[FeH_2O]^+$ with $OH^\bullet$ (also changing the oxidation state of iron). The latter reaction was done for two different spin states; for the S = 2.5 case, however, we did not succeed to reproduce the ADF benchmark energies. For the reactions representative for the systems we study, though, again an accuracy of 8 kJ/mol was reached. The projectors chosen for the rest of the work is the Fe_223 set with a core radius of 1.458 a.u., an augmentation radius of 1.658 a.u., E_p = 2.226 a.u., $E_{d,2}$ = 0.32717, and $E_{d,3}$ = 2 a.u.

Finally, we have tested whether possible overlap of augmentation radii from different atoms leads to errors. Since we chose the augmentation radii relatively large, overlap could very well occur, especially during molecular dynamics. In optimized geometries, it only occurs for double bonds. We tested the effect of overlapping augmentation radii by selecting one bond in several molecules and shortening it to the point the augmentation radii start to overlap. For these series of geometries we again compared to benchmark ADF calculations (Table 2.5). Note that for the iron complexes the optimized distances differ slightly between the PAW and ADF calculations. For these molecules, the comparison is made for equal distortion, thus different bond lengths are compared. In Table 2.5, we do not find any anomalous effects when the augmentation radii start to overlap, so we can conclude it is save to use the relatively large radii that we use.

Also, the plane wave convergence with the now selected projectors has been studied. Since Car-Parrinello simulations are very costly, it is necessary to choose the plane wave cutoff as low as possible. At too low plane wave cutoffs, however, the PAW code does not converge at all, and the calculations crash. In Table 2.6, a

Table 2.5 *Test of the effect of overlapping augmentation radii. For several molecules one bond is shortened such that the projectors overlap, and the energies are compared to ADF benchmark values. For the bond lengths at which the projectors overlap, the PAW energies are printed in bold. Energies are given in kJ/mol, and the wavefunction and density cutoffs are 60 Ry and 120 Ry, respectively.*

Molecule	Shortened bond	Distance where overlap starts (Å)	Bond length (Å)	PAW	ADF
CH_4	C–H	0.999	1.094	0.0	0.0
			1.03	5.9	7.0
			0.98	**22.9**	24.8
			0.9	**83.0**	85.5
FeO^{2+}	Fe=O	1.548	PAW: 1.639 / ADF: 1.608	0.0	0.0
			PAW: 1.57 / ADF: 1.54	9.2	8.7
			PAW: 1.53 / ADF: 1.50	**25.4**	23.7
			PAW: 1.45 / ADF: 1.42	**95.1**	86.3
$[FeH_2O]^+$	Fe---O	1.548	PAW: 1.990 / ADF: 1.958	0.0	0.0
			PAW: 1.85 / ADF: 1.82	10.6	10.1
			PAW: 1.75 / ADF: 1.72	38.6	38.3
			PAW: 1.70 / ADF: 1.67	57.1	63.0
CH_2O	C=O	1.374	1.211	**0.0**	0.0
			1.35	**52.9**	53.7
			1.38	74.3	74.6

Table 2.6 *Plane wave convergence with the present projector sets. All energies are in kJ/mol, and the differences with the ADF results are given in brackets.*

Plane wave cutoff	Ratio in cutoffs	$[FeH_2O]^+ + OH^\bullet \rightarrow [FeOH]^+ + H_2O$	$[Fe(H_2O)_5]^{2+} + H_2O_2 \rightarrow [Fe(H_2O)_5OH]^{2+} + OH^\bullet$	$H_2O_2 \rightarrow 2\ OH^\bullet$
30 Ry	2	*several calculations crashed*		259.2 (+22.9)
30 Ry	3	–227.1 (+4.9)	–27.4 (–9.3)	236.3 (+0.0)
40 Ry	2	–225.8 (+6.2)	–24.2 (–6.1)	236.7 (+0.4)
40 Ry	3	–228.8 (+3.2)	–25.1 (–7.0)	236.0 (–0.3)
50 Ry	2	–226.2 (+5.8)	–24.9 (–6.8)	236.0 (–0.3)
50 Ry	3	–226.7 (+5.3)	–25.0 (–6.9)	236.3 (+0.0)
60 Ry	2	–226.4 (+5.6)	–25.2 (–7.1)	236.1 (–0.2)
60 Ry	3	–226.8 (+5.2)	–25.4 (–7.3)	236.3 (+0.0)
ADF (BSSE-corrected)		–232.0	–18.1	236.3

comparison is given for different plane wave cutoffs and different ratios between the density cutoff and the wavefunction cutoff. We find the energies are acceptably converged already at 30 Ry when the density cutoff is chosen three times higher (90 Ry). Note that when pseudopotentials are used, the required cutoff is higher (typically 50-70 Ry as a minimum).

2.2.3. Conclusion

Although the PAW method is the best option for modeling iron in plane wave based simulations, it is not as transferable and exact as one would hope for. In the PAW method, partial and pseudo partial waves are used to transform the true wavefunction to a pseudowavefunction, such that also the reverse transformation is well-defined, in principle making the method transferable: no corrections need to be added that are only exact for specific cases. Moreover, when the partial and pseudo partial waves do not form complete sets, the part of the wavefunction (*within* the augmentation regions) that is missed by the augmentation is transferred unaugmented to the pseudowavefunction and is still described by the underlying plane wave basis set. However, we have noted that the plane waves converge very slowly for this part of the wavefunction, even to such an extent that this part of the wavefunction is effectively missed in the calculations. In practice, this causes the partial waves to strongly bias the results.

To correct for the effect of incomplete sets of partial waves, an additional potential $\bar{v}$ has been introduced in Ref. 18, but this potential only corrupts the elegant approach of the PAW method: the potential $\bar{v}$ causes the PAW method to become non-transferable; it makes the results at infinite plane wave cutoff incorrect; and, in fact, it does not remove the bias of the partial wave sets satisfactorily.

Regardless of the shortcomings of the PAW method, we have taken a pragmatic approach and we optimized and tested new sets of partial waves ("projectors") that give correct results for our applications. New projectors were constructed for hydrogen, oxygen, carbon, and iron that give results that compare to ADF benchmark calculations within 8 kJ/mol for reactions representative to our applications.

2.3. Calculation of pressure in the case of periodic boundary conditions*

2.3.1. Introduction

In Molecular Dynamics (MD) or Monte Carlo (MC) simulations it is common practice to calculate the pressure in the system, either in order to perform constant pressure (NPT) simulations, or simply to monitor it. Especially in our simulations of systems containing positively charged iron ions and no counter ions, it would be a good idea to check the pressure, as no experimental densities can be available for such systems. However, unfortunately, the standard method to calculate the pressure, namely

* This section is based on: M.J. Louwerse and E.J. Baerends, *Chem. Phys. Lett.* **421** (2006) 138-141; we thank Prof. Daan Frenkel for useful discussions.

using the virial equation, cannot be used for our case. This section is meant to explain why, and to warn readers not to use the virial equation in cases where it does not apply.

For our simulations, we are left to the pragmatic approach: we can observe that the self-diffusion of the water molecules is normal in our simulations. And thus the pressure must be reasonably close to 1 atm.

The standard method for calculating the pressure is using the virial equation, which is basically a sum over the forces on all atoms:

$$P = \frac{Nk_BT}{V} + \frac{1}{3V}\left\langle \sum_{i=1}^{N} \mathbf{r}_i \cdot \mathbf{f}_i \right\rangle, \tag{2.6}$$

where k_B is Boltzmann's constant, $\mathbf{f}_i$ is the force on atom i due to all other atoms, and <…> denotes the statistical average over time. However, we will show this method breaks down when periodic boundary conditions are applied.

For pair-additive forcefields the virial equation is usually written as:

$$P = \frac{Nk_BT}{V} + \frac{1}{6V}\left\langle \sum_{i=1}^{N}\sum_{j\neq i}^{N} \mathbf{r}_{ij} \cdot \mathbf{f}_{ij} \right\rangle, \tag{2.7}$$

where $\mathbf{f}_{ij}$ is the force on atom i due to atom j and $\mathbf{r}_{ij} \equiv \mathbf{r}_i - \mathbf{r}_j$. Fortuitously, Equation 2.7 continues to hold when using periodic boundary conditions, so for many classical simulations there is no problem, because most simulations are still performed with pair-additive forcefields. However, whenever non pair-additive forcefields or ab initio energies are used in combination with periodic boundaries, the virial equation should *not* be applied to calculate the pressure in the system.

We will first give a derivation of Equation 2.6 and explain why Equation 2.6 is incorrect for systems with periodic boundaries. Next, we will show how Equation 2.7 for pair-additive forcefields is usually derived from Equation 2.6, and why this derivation is flawed under periodic boundary conditions. We will then give a correct derivation for the pressure for pair-additive forcefields, and show that Equation 2.7 still holds. A compensation of errors in the flawed scheme leads –by coincidence– to the correct outcome. This has led to unjustified confidence in Equation 2.6, and applications of the virial equation in cases where it does not hold. Although examples of correct pressure calculations are also available in the literature,[67,68] we feel an explicit warning is warranted. A first warning that the virial equation is not complete for periodic systems was published in 1983.[69]

Finally, because readers may find it hard to believe that the virial equation does not apply in all cases, we give a simple example for which it fails.

2.3.2. Derivation of the virial equation

From thermodynamics, it is known that the pressure is equal to the derivative of the Helmholtz free energy, A, with respect to the volume, V, at constant temperature, T (see any physical chemistry textbook):

$$P = -\left(\frac{dA}{dV}\right)_T \tag{2.8}$$

This equation can be split into terms for the kinetic energy, K, and the potential energy, U; additionally taking a statistical average gives:

$$P = \frac{Nk_BT}{V} - \left\langle \frac{dU}{dV} \right\rangle \tag{2.9}$$

The first term on the right hand side is the kinetic energy derivative term, which is given by the ideal gas law. In order to evaluate the potential energy derivative term, we use that for periodic systems the potential energy per unit cell is a function of the atomic positions $(\mathbf{r}_1, \mathbf{r}_2, \ldots \mathbf{r}_N) \equiv \mathbf{r}^N$ of the N atoms in the unit cell, and the box length L:

$$U = U\left(\mathbf{r}^N, L\right) \tag{2.10}$$

With the positions of the atoms in a single unit cell given, the box length can be used to establish the positions of atoms in all periodic images of the unit cell, and hence the potential energy. For simplicity, we assume a cubic periodic box with length L that is scaled uniformly; obviously a similar derivation could be performed for differing lattice vectors, and a generalization to the various terms of the stress tensor is also straightforward.

The derivative of U with respect to V has contributions due to the variation of U with respect to L with the atom positions fixed (bringing the atoms in one cell closer to the atoms in another cell), and the variation of U due to the scaling of atom positions with L: $\mathbf{r}_i = \mathbf{s}_i L$. Using the chain rule we obtain:

$$\frac{dU}{dV} = \frac{dL}{dV}\left(\frac{\partial U}{\partial L} + \sum_{i=1}^{N} \frac{d\mathbf{r}_i}{dL} \cdot \frac{\partial U}{\partial \mathbf{r}_i}\right) = \frac{1}{3L^2}\left(\frac{\partial U}{\partial L} + \sum_{i=1}^{N} \frac{\mathbf{r}_i}{L} \cdot \frac{\partial U}{\partial \mathbf{r}_i}\right) = \frac{1}{3V}\sum_{i=1}^{N} \mathbf{r}_i \cdot \frac{\partial U}{\partial \mathbf{r}_i} + \frac{1}{3L^2}\frac{\partial U}{\partial L} \tag{2.11}$$

Now using the definition of the force on atom i, $\mathbf{f}_i$:

$$\mathbf{f}_i = -\frac{\partial U}{\partial \mathbf{r}_i}, \tag{2.12}$$

and substituting Equations 2.11 and 2.12 into Equation 2.9, we obtain the correct form of the virial equation:

$$P = \frac{Nk_BT}{V} + \left\langle \frac{1}{3V}\sum_{i=1}^{N} \mathbf{r}_i \cdot \mathbf{f}_i - \frac{1}{3L^2}\frac{\partial U}{\partial L} \right\rangle \tag{2.13}$$

In these equations, the full derivatives of U (dU/dV and dU/dL) denote the dependence of U on the box length L with scaling of the atomic coordinates included, and the partial derivative $\partial U/\partial L$ is the dependence on L *without* scaling of atomic coordinates. For non-periodic systems, for which the potential energy does not depend on the size of an enclosing box, the term containing $\partial U/\partial L$ is zero. Changing the box length without also changing the atomic coordinates has no effect in a non-periodic system, and we arrive back at the standard virial equation (Equation 2.6). However, when periodic boundary conditions are used, the additional term is not zero. Increasing the box length without varying the atomic coordinates would still lead to an increase in the distance between the particles in different copies of the box, and the partial derivative $\partial U/\partial L$ will have a finite value. As a result, we conclude that under periodic boundary conditions Equation 2.6 does not hold.

2.3.3. The special case of pair-additive forcefields

In the special case of pair-additive forcefields, the virial equation is usually written in a pair wise manner (Equation 2.7). This is probably the most commonly used form of the virial equation. Although Equation 2.6 is incorrect under periodic boundary conditions, Equation 2.7 is correct even for periodic boundary conditions.

We will now first give the common derivation of Equation 2.7 from Equation 2.6 for non-periodic systems, and explain why this derivation does not hold for periodic systems. Then, we will give the correct derivation and show that Equation 2.7 does apply. Apparently, errors in the flawed derivation cancel out to give the correct result.

The standard derivation begins by writing the force on atom i due to all other atoms:

$$\mathbf{f}_i = \sum_{j \neq i}^{N} \mathbf{f}_{ij} \tag{2.14}$$

When we substitute this into Equation 2.6, we get:

$$P = \frac{Nk_BT}{V} + \frac{1}{3V}\left\langle \sum_{i=1}^{N}\sum_{j \neq i}^{N} \mathbf{r}_i \cdot \mathbf{f}_{ij} \right\rangle \tag{2.15}$$

In this equation we can permute the indices i and j resulting in:

$$P = \frac{Nk_BT}{V} + \frac{1}{3V}\left\langle \sum_{j=1}^{N}\sum_{i \neq j}^{N} \mathbf{r}_j \cdot \mathbf{f}_{ji} \right\rangle \tag{2.16}$$

Now using $\mathbf{f}_{ij} = -\mathbf{f}_{ji}$, and adding the two equivalent right hand sides of Equations 2.15 and 2.16, and dividing by 2, we arrive at Equation 2.7:

$$P = \frac{Nk_BT}{V} + \frac{1}{6V}\left\langle \sum_{i=1}^{N}\sum_{j \neq i}^{N} \mathbf{r}_{ij} \cdot \mathbf{f}_{ij} \right\rangle \tag{2.7}$$

For periodic systems, however, this derivation is not correct, because the assumption going from Equation 2.15 to Equation 2.16 no longer applies. With periodic boundary conditions, the total force on atom *i* is not only due to all other atoms in the original unit cell, but to *all* other atoms, including those in the periodic copies of the unit cell. If we now introduce the number of periodic copies *M* (which is, in principle, infinite) into Equation 2.14, we get:

$$\mathbf{f}_i = \sum_{j \neq i}^{MN} \mathbf{f}_{ij} \tag{2.17}$$

The equivalent of Equation 2.15 then becomes:

$$P = \frac{Nk_BT}{V} + \frac{1}{3V}\left\langle \sum_{i=1}^{N}\sum_{j \neq i}^{MN} \mathbf{r}_i \cdot \mathbf{f}_{ij} \right\rangle, \tag{2.18}$$

and we see that the indices *i* and *j* are no longer equivalent and thus cannot be permuted.

To perform a correct derivation of the pressure in periodic systems for pair-additive forcefields, we begin with the potential energy per unit cell:

$$U = \frac{1}{2}\sum_{i=1}^{N}\sum_{j \neq i}^{MN} U_{ij}\left(\mathbf{r}_{ij}\right), \tag{2.19}$$

where U_{ij} is the contribution to the energy *U* of the interaction between the atoms *i* and *j*. Note that in this relation there is no explicit dependence on *L*; the only dependence on *L* is implicit via scaling of $\mathbf{r}_{ij}$. When atoms *i* and *j* are in the same unit cell, it is evident that the derivative of interatomic distance with *L* is $d\mathbf{r}_{ij}/dL = \mathbf{r}_{ij}/L$, but this is true even when they are in different cells. For instance, if atom *j* is in the cell with its origin at position $\mathbf{R_n} = (n_x\mathbf{e}_x + n_y\mathbf{e}_y + n_z\mathbf{e}_z)L \equiv \mathbf{n}L$, then $\mathbf{r}_{ij} = (\mathbf{s}_i - \mathbf{s}_j - \mathbf{n})L$, and again $d\mathbf{r}_{ij}/dL = \mathbf{r}_{ij}/L$. Therefore, the derivative of *U* is:

$$\frac{dU}{dV} = \frac{1}{2}\frac{dL}{dV}\sum_{i=1}^{N}\sum_{j \neq i}^{MN}\frac{d\mathbf{r}_{ij}}{dL}\cdot\frac{\partial U}{\partial \mathbf{r}_{ij}} = \frac{1}{6L^2}\sum_{i=1}^{N}\sum_{j \neq i}^{MN}\frac{\mathbf{r}_{ij}}{L}\cdot\frac{dU_{ij}}{d\mathbf{r}_{ij}} = \frac{-1}{6V}\sum_{i=1}^{N}\sum_{j \neq i}^{MN}\mathbf{r}_{ij}\cdot\mathbf{f}_{ij} \tag{2.20}$$

Now we can substitute Equation 2.20 into Equation 2.9, and we arrive at Equation 2.7, suitably modified for the energy per unit cell in a periodic system. So Equation 2.7 proves to be correct after all, even when periodic boundary conditions are applied. Apparently, the error introduced in the derivation of Equation 2.7 from the erroneous Equation 2.6 leads to the correct result. Because of the erroneous derivation, however, this correct result does not prove the starting point, Equation 2.6, to be correct.

It is very fortunate that Equation 2.7 is correct for periodic systems, because this form of the virial equation has been used in a vast number of simulations. However, since Equation 2.6 is not correct for periodic systems, any simulation code that uses

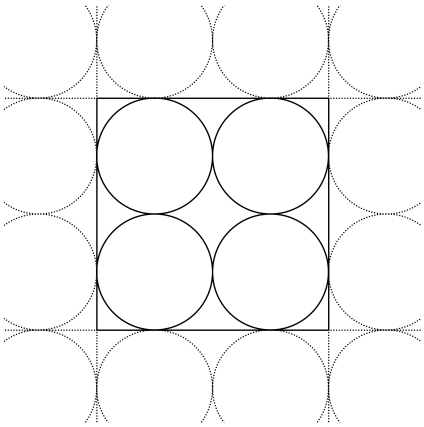

Figure 2.3 *Example of a system for which the error in the virial equation is obvious: an infinite perfect lattice.*

that form of the virial equation to calculate the pressure in a periodic system will give an incorrect pressure.

2.3.4. A simple example

We have shown that the virial equation (Equation 2.6) is not correct for systems with periodic boundary conditions, but for the special case of pair-additive forcefields (Equation 2.7) the equation can be applied to periodic systems. Thus, whenever the energy calculation is not pair-additive the virial equation should not be used for periodic systems. To demonstrate this, we will now give a simple example that shows that indeed Equation 2.6 cannot be applied under periodic boundary conditions.

Consider a small periodic box with four atoms on a perfect lattice (Figure 2.3), with a purely repulsive pair wise interaction between the atoms. Take the system to be at zero temperature (i.e. there is no thermal motion), and suppose that it is strongly compressed. The pressure in this system is highly positive because of the repulsion between the atoms. Now, when we calculate the force on an atom, it will be zero because of the infinite perfect lattice. Substituting these zeros in Equation 2.6, we would find only the ideal gas term, i.e. $P = 0$ at $T = 0$, which is obviously not correct.

When Equation 2.7 is used to calculate the pressure in this example, we do obtain a high positive value for the pressure. We conclude that Equations 2.6 and 2.7 are indeed different, and that Equation 2.6 is giving incorrect results for periodic systems. Adding the $\partial U/\partial L$ term (Equation 2.13) will lead to the correct result.

2.3.5. Discussion

We have shown that the virial equation in its original form (Equation 2.6) is not applicable when periodic boundary conditions are used. Our intent is firstly to warn readers for this, and secondly, to point out that there is no simple method to calculate

the pressure in periodic systems. The only way to calculate the pressure in a periodic system is either to directly evaluate Equation 2.9 numerically, or to take the analytical derivative of the potential energy, using Equation 2.13. Either way requires much effort.

Fortunately, for most classical simulations pair-additive forcefields are used, and for these simulations there is no problem. Nevertheless, there is a potential pitfall: because in Molecular Dynamics the net forces on the atoms are calculated in order to facilitate Newtonian dynamics, one might be tempted to use these atomic forces to calculate the pressure via Equation 2.6.

An example of a situation where real problems could be expected is when polarizable forcefields are used. In that case, the energy is not pair wise additive and the only way to calculate the pressure is to use Equation 2.9 or Equation 2.13. Note that even when the implementation is such that, after evaluating the polarization, the energy is calculated in a pair wise manner (i.e. calculating the Coulombic interactions with the induced dipoles), Equation 2.7 cannot be used. This is because the induced dipoles depend on all atomic positions, and U_{ij} is not a function of only $\mathbf{r}_{ij}$ but depends on all $\mathbf{r}^N$, so Equation 2.20 is not applicable.

Another area for which our conclusions apply is ab initio calculations with periodic boundary conditions. To calculate the pressure it is necessary to evaluate the full derivative of the energy with respect to the volume. This demands a huge effort, but there are a few examples where it has been done.[70-73] Readers who might be tempted to calculate the pressure in a classical way, using just the forces $\mathbf{f}^N$ on the nuclei, should be warned again that the virial equation as it is written in Equation 2.6 is not correct for periodic systems. One should use Equation 2.13, which contains the $\partial U/\partial L$ term.

An alternative that is as simple as the virial equation, but which also holds for periodic boundary conditions, would be very welcome.

3.

The hydroxyl radical and hydroxide ion in liquid water: a comparative study*

Abstract:

Car-Parrinello Molecular Dynamics (CPMD) simulations of the solvated states of the hydroxyl radical and the hydroxide ion have been performed using the BLYP exchange-correlation functional. The structures of the solvation shells of the two species were examined, and it was found that the $OH^{\bullet}$ radical forms a relatively well-defined solvation complex with four neighboring water molecules. Three of these molecules are hydrogen bonded to the $OH^{\bullet}$, while the fourth is hemibonded via a three-electron two-centered bond between the oxygen atoms of the $OH^{\bullet}$ and water. The activity and the diffusion mechanism of the $OH^{\bullet}$ radical in water are discussed in comparison with the OH^{-} ion. Although the results may be partially influenced by the tendency of the BLYP density functional to overestimate hemibonded structure, the present simulations suggest that the widely accepted picture of rapid diffusion of $OH^{\bullet}$ radical in water through a hydrogen exchange reaction may need to be reconsidered.

* This chapter is based on: P. Vassilev, M.J. Louwerse, and E.J. Baerends, *Chem. Phys. Lett.* **398** (2004) 212-216 and P. Vassilev, M.J. Louwerse, and E.J. Baerends, *J. Phys. Chem. B* **109** (2005) 23605-23610.

3.1. Introduction

The first step in the Fenton reaction is the splitting of hydrogen peroxide in two hydroxyl ($OH^{\bullet}$) radicals, of which one is coordinated to the Fe ion and becomes an OH^- ligand. The other $OH^{\bullet}$ radical could attack other species present in the solution or react with the $FeOH^{2+}$ forming FeO^{2+}, either via a chain mechanism involving one or more water molecules or directly by reaction with the OH^- ligand. This has been discussed in Chapter 1. In the present chapter, we study the solvation of the $OH^{\bullet}$ radical in water and its possibilities to diffuse via hydrogen exchange reactions with the water molecules.

The hydroxyl radical in general, and its hydrated state in particular, is an important entity playing a major role in numerous biochemical, electrochemical, and atmospheric reactions. As a derivative of hydrogen peroxide, $OH^{\bullet}$ is also a powerful oxidizing and bleaching agent with an industrial application. Finally, the formation and presence of $OH^{\bullet}$ in biological cells is recognized as the cause of numerous cell diseases (see for example Ref. 74 and references therein). The majority of these processes occur in liquid water or, as in the case of the earth's atmosphere, in liquid water droplets. The structure and the transport properties of the hydroxyl radical in water are decisive then for the kinetics of these reactions and detailed knowledge of the solvation shell and bonding with the hydrating water molecules is vital for understanding the mechanisms of these processes.

Several computational studies at different levels of the theory have investigated the $OH^{\bullet}$ radical and the formation of $OH^{\bullet}(H_2O)_n$ clusters,[74-82] but only a few have also considered the hydrated hydroxyl radical in liquid water.[74,79] The latter simulations of the solvated state however were performed using classical or hybrid solvation model methods.

With the development of the Density Functional Theory[11,12] (DFT) and the Car-Parrinello[13] approach in particular, it became feasible to perform computer simulations of relatively small (but still representative for the real systems) models with quantum mechanics. One of the first subjects under study was liquid water.[49-51,83] The successful application of this computational scheme to reproduce and predict the experimentally observed data proved the applicability and efficiency of the DFT-based molecular dynamics (MD) and now an increasing number of publications are based on the same approach.

The hydronium H_3O^+ and the hydroxide OH^- ions have also been intensively studied.[84-88] It was shown that both H_3O^+ and OH^- introduce the so-called charge defect within the hydrogen bond network of liquid water and display anomalously high mobilities realized via a proton exchange reaction with a neighboring water molecule. This is known as the Grotthuss diffusion mechanism[89] or as “structural diffusion”.

Being a radical, the $OH^{\bullet}$ is generally recognized as a highly active species and it is widely anticipated that the hydroxyl radical would also rapidly diffuse in liquid water via a *hydrogen* exchange reaction, analogously to the proton exchange reaction in the case of the H_3O^+ and OH^- ions:

$$OH^{\bullet} + H_2O \rightarrow H_2O + OH^{\bullet} \qquad (3.1)$$

Due to difficulties in detecting the $OH^{\bullet}$ species in liquid water, however, this process cannot be observed and characterized experimentally, leaving computer simulations as the only available approach to investigate the system. The processes of proton or hydrogen exchange involve the breaking and formation of the rather strong internal O–H bond of the water molecule in a complex interplay with the much weaker hydrogen bonds governing the structure of the solvent. For such a system the DFT-based ab initio molecular dynamics simulations is the most suitable and today perhaps the only applicable method to study the system appropriately.

Despite the importance of the hydroxyl radical in liquid water, to the best of our knowledge no ab initio molecular dynamics simulations of hydrated $OH^{\bullet}$ have been published prior to the work presented in this chapter. The previously mentioned theoretical studies[74,79] were performed using classical MD or hybrid solvation models, and apart from radial distribution functions (RDFs) no detailed structural information for the hydration complex of the $OH^{\bullet}$ was provided. The $OH^{\bullet}(H_2O)_n$ complexes have been studied in detail using DFT and high-level ab initio methods.[74-82] It was shown that the hydroxyl radical can take part in hydrogen bonds with water molecules as H-bond donor (with an interaction energy of 23-25 kJ/mol) or as H-bond acceptor using its sp^2 lone pairs (14-15 kJ/mol per H-bond).[76,77] The singly occupied p_π orbital can accept a supposedly weaker H-bond, or can be involved in a direct (hemi-) bond between the oxygen of the $OH^{\bullet}$ and the oxygen of a neighboring water molecule. However, comparing DFT results using the BLYP functional with those of high-level ab initio methods, it was concluded that the BLYP functional erroneously favors the formation of such a hemibond.[74] A similar type of interaction, the so-called two-centered three-electron hemibond, was also found for other open-shell systems with a single unpaired electron.[90,91] The strength of the interaction was again overestimated by the BLYP functional compared to the post-Hartree-Fock results and these findings put forward the question whether the BLYP density functional can be used for these systems and for the hydrated $OH^{\bullet}$ in particular. Nevertheless, Hamad et al.[74] reported that for $OH^{\bullet}(H_2O)_n$ clusters, n = 1, 2, …, 5, the differences between the BLYP-DFT and post-Hartree-Fock MP2 simulations vanish with the increase of the number of complexing water molecules n. This indicates that despite the overestimated hemibond interaction, the BLYP density functional, which was proven to be one of the best for liquid water,[50] may still be suitable for MD simulations of $OH^{\bullet}$ in liquid water.

In this chapter, we present a DFT-based ab initio molecular dynamics study of the hydrated $OH^{\bullet}$ using the BLYP exchange-correlation density functional. We will concentrate on the structural, dynamical, and electronic properties of the hydroxyl radical $OH^{\bullet}$ in comparison with the hydroxide ion OH^{-}. In the following analysis of the simulation data, O* will denote the oxygen center of the $OH^{\bullet}$ or OH^{-} as appropriate. To locate the OH species, all hydrogen atoms are assigned to the closest oxygen atom, and the oxygen to which just one H atom has been assigned as being the one of $OH^{\bullet}$ or OH^{-}.

In Section 3.5, we will discuss the results of some more recent ab initio MD simulations of $OH^{\bullet}$ in liquid water.

3.2. Computational details

The molecular dynamics (MD) simulations were performed using the Car-Parrinello[13] Density Functional Theory[11,12] package PAW implementing the Projector Augmented Wave Method.[18] We used the BLYP exchange-correlation density functional.[65,66]

The computational models consist of (i) 32 water molecules (spin-restricted calculation), (ii) 31 water molecules and one OH^- species (total charge of –1, spin-restricted calculation), and (iii) 31 water molecules and one $OH^\bullet$ species (spin-polarized calculation) for the (i) pure liquid water, (ii) hydrated OH^-, and (iii) hydrated $OH^\bullet$ MD simulations. The size of the periodic cubic box in all three cases was 9.865 Å. The starting configurations for the hydroxyl radical and hydroxide ion simulations were prepared using a configuration taken from the pure liquid water simulation and taking away a hydrogen atom or a proton, respectively. The MD time step was 0.157 fs (6.5 a.u.) and the fictitious mass for the electronic degrees of freedom was 100 a.u. The simulation lengths after equilibration were 2 ps, 15 ps, and 32 ps respectively for (i), (ii), and (iii). NVE molecular dynamics was performed for liquid water at a mean temperature T = 291 K (i), for the hydroxide ion (ii) and hydroxyl radical (iii) simulations the temperature was set to T = 300 K, controlled by a thermostat on the ionic degrees of freedom with an oscillation period of 30000 a.u. (approximately 0.7 ps) and 60000 a.u., respectively for (ii) and (iii). Additionally frictions of 0.0004 and 0.001 for (ii) and (iii) were applied on the Nosé variable, and 0.00005 in either (ii) and (iii) on the electron wave function, as defined in the PAW code. In order to decrease the coupling between the electronic and ionic degrees of freedom, for the hydrogen atoms we used the deuterium isotope.

The cutoffs for the plane wave basis for the electron pseudo-wave function and the pseudo-charge density were 408 eV (30 Ry) and 1225 eV (90 Ry), respectively. We used one s-projector for the H atoms and one s- and two p-projectors for the O atoms with only the valence electrons included in the calculation. For the construction of the H projector we used a partial wave energy of E = –0.24001 a.u. and a radius of R_c = 0.557 a.u., as defined in the PAW atomic setups generation program. For the O atom we used E = –0.87577 a.u. for the s-projector and E = –0.33159 a.u. and 0.27777 a.u. for the p-projectors with R_c = 1.267 a.u. This set of parameters, including the fictitious mass and the time step for the MD, were tested for liquid water and can produce a stable NVE MD simulation conserving the total energy within less than 0.005 a.u. for 2 ps. For the radial distribution functions we used a bin size of 0.04 Å. The projection scheme for calculating the projected density of states is based on the set of PAW projectors as implemented in the program PAW.

3.3. Results and discussion

The ab initio molecular dynamics (MD) simulations of the hydrated states of $OH^\bullet$ and OH^- reveal that although the difference is "just" one electron, the two systems display rather dissimilar and in the case of $OH^\bullet$ unexpected structural and dynamical properties. The most appealing result is the lack of hydrogen exchange in the case of

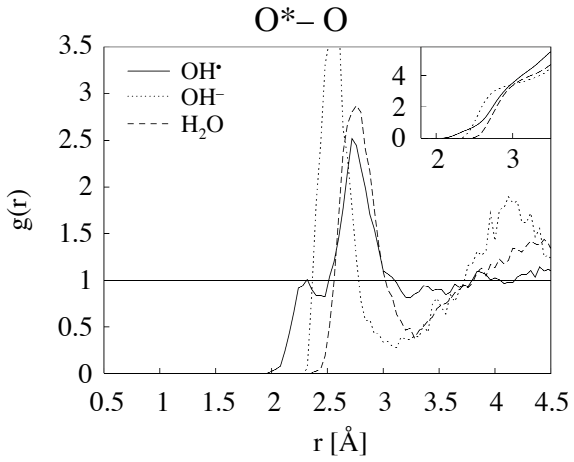

Figure 3.1 *Oxygen–oxygen radial distribution functions (RDF): O*–O RDF of hydroxyl radical (solid line), O*–O RDF of hydroxide ion (dotted line), and O–O RDF of pure liquid water (dashed line). O* denotes the oxygen atom from the OH species, O denotes the oxygen atoms from the water molecules. The integrated RDFs are given in the inset graph.*

the radical. Contrary to the generally accepted picture for highly active OH• species, we did not observe even a single hydrogen jump between the OH• and the hydrating water molecules during the MD simulation of a length of 32 ps. This suggests that the widespread anticipation for rapid diffusion of the OH• via a hydrogen exchange reaction with the surrounding water molecules may need to be reconsidered.

The origins of this behavior are in the specific structural characteristics of the solvation shells of the radical. In this chapter, we give a detailed description of the solvation complex of hydroxyl radical in comparison with the hydroxide ion as found from the MD simulation. We will first look into the distribution functions characterizing the solvated states of the OH^- and OH• and we will continue examining the electronic structure of the hydrated OH•. Finally the oxidative properties and the diffusion mechanism of the OH• radical in water are discussed.

3.3.1. Radial distribution functions

The comparison between the O*–O radial distribution functions (RDF) of the hydroxyl radical and hydroxide ion, O* being the oxygen atom from OH, reveals that in both cases the coordination shells are characterized with a major peak at around 2.75 and 2.6 Å, for OH• and OH^- respectively (Figure 3.1). The integrated values of the RDFs up to the minimum at ca. 3 Å is in either case around four, i.e. at first approximation four water molecules constitute the coordination shells of both species. However, in the case of the radical there is an additional peak at around 2.3 Å with an integrated value of one, which indicates the presence of one water molecule in a rather close contact with the central OH•. The distance of 2.3 Å is much shorter than the O–O

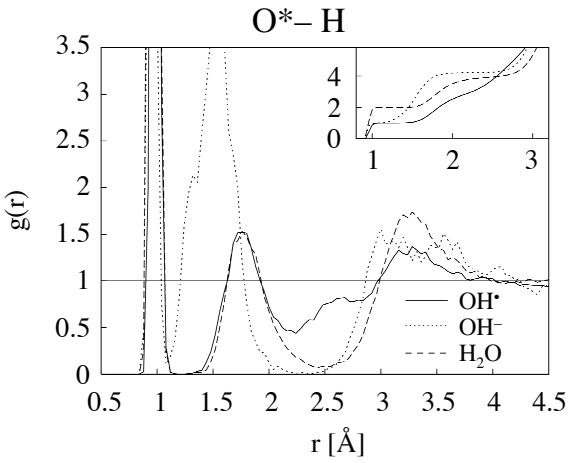

Figure 3.2 *Oxygen–hydrogen radial distribution functions (RDF): O*–H RDF of hydroxyl radical (solid line), O*–H RDF of hydroxide ion (dotted line), and O–H RDF of pure liquid water (dashed line). O* denotes the oxygen atom from the OH species, O denotes the oxygen atoms from the water molecules, and H denotes hydrogen atoms regardless if they are from the OH species or water molecules. The integrated RDFs are given in the inset graph.*

separation of around 2.8 Å for a hydrogen bond. Neither liquid water nor the hydroxide ion exhibit a similar peak in their RDFs and this suggests that the first coordination shell of the $OH^{\bullet}$ has a rather different and unique composition. However, the O–O radial distribution function alone does not provide sufficient information to resolve the origin of this peak and to determine in detail the structure of the $OH^{\bullet}(H_2O)_4$ hydration complex. A more thorough analysis of the simulation data is presented in the next section, introducing two-dimensional distribution functions.

From the oxygen–hydrogen RDFs it is noticeable that at short distances (Figure 3.2, $r < 2$ Å) the distribution function corresponding to the hydroxyl radical is comparable to the one of pure water. This suggests that analogous to H_2O, the $OH^{\bullet}$ is hydrogen bonded with *at least* 2 of the 4 hydrating water molecules, as indicated from the integrated values of the peak in the O*–H RDF at around 1.8 Å. However, an additional feature of the radical, which just as in the case of the O–O distribution function cannot be explained only from the RDFs, is the presence of a peak at around 2.5 Å. We will come back to these data later. Note that the first peak in the O*–H RDF for $OH^{\bullet}$ is very well defined, corresponding to the fact that no hydrogen transfers were observed.

Considering the second coordination shells (Figure 3.1, $r > 3$-3.5 Å), we see that while they can be easily identified in the case of OH^- and H_2O, for the $OH^{\bullet}$ the radial distribution function approaches the unity value. This is equivalent to a random distribution of the water molecules with respect to the $OH^{\bullet}(H_2O)_4$ hydration complex itself, suggesting that the presence of $OH^{\bullet}$ results in a disruption of the hydrogen bonding network of liquid H_2O and the radical cannot be considered as being

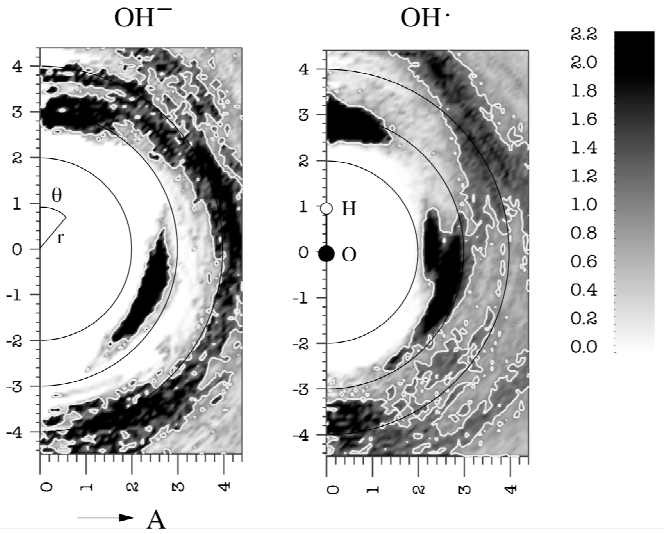

Figure 3.3 *OH–O distribution function P(r, θ) for the hydroxide ion (left panel) and hydroxyl radical (right panel). The single white isoline has a value of 1.0.*

embedded in the structure of water, as for example OH^- is. Quite on the contrary, the hydroxide ion appears strongly bound to the hydrating water molecules leading to shortened O–O and O–H separations in the first coordination shell and enhanced structure of the solvent, reflected in the relatively more pronounced peaks in the distribution functions, especially in the O*–O RDF.

3.3.2. Detailed structure of the solvation complexes of OH^- and $OH^•$

For the purpose of characterizing the solvation shells of the OH species we employ a two-dimensional OH–X distribution function $P(r, \theta)$, where r is the distance between the oxygen atom O* of the hydroxyl radical and an atom of interest X, X being either O or H from the solvent (see also Figure 3.3). θ is the angle H*–O*–X, with H* being the hydrogen atom from the OH. The OH species is then along the vertical axes ($\theta = 0$) with the oxygen atom O* in the origin of the graph. For example in the case of the OH^- in liquid water (left panel of Figure 3.3) the two-dimensional OH–O radial distribution function shows a rather broad peak around r = 2.6-2.7 Å and θ in the range of 90-120º, corresponding to the O atoms from the first coordination shell. Additionally there is a peak at around r = 3 Å and $\theta = 0$º.

The structure of the hydrated OH^- has been determined previously by Tuckerman et al.[87,92] and therefore will not be discussed here. We will only recall that one can distinguish between two solvation states of the OH^-. The first one is characterized with 4 water molecules in the equatorial plane of the OH^- with the hydroxide ion being acceptor of the H-bonds. An additional fifth water molecule, which is further away and weakly bound with its O to the H atom of the OH^- ($\theta = 0$), was also found.[87,92] This complex was identified as the inactive state of the OH^- with respect to the proton

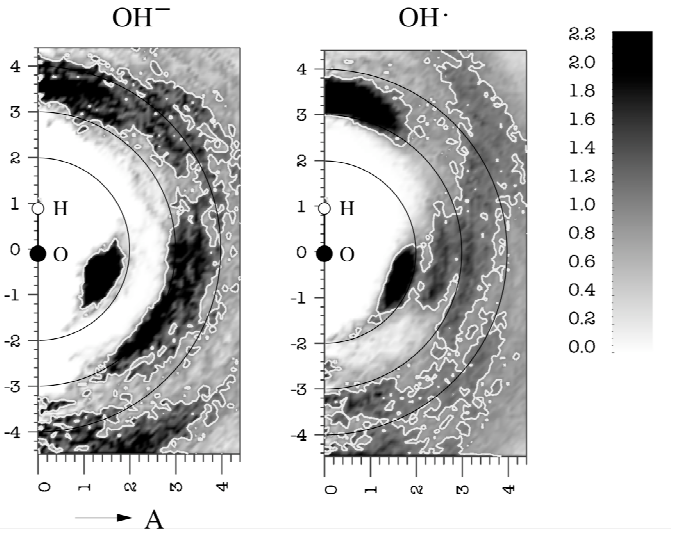

Figure 3.4 *OH–H distribution function P(r, θ) for the hydroxide ion (left panel) and hydroxyl radical (right panel). The single white isoline has a value of 1.0.*

exchange reaction with a neighboring H_2O. The second solvation complex is characterized with a tetrahedral configuration of the solvating H_2O, i.e. with 3 neighboring water molecules at θ around 104° as H-bond donors and a fourth water molecule acting as H-bond acceptor in a hydrogen bond with the H of OH^-. This complex was determined to be the active state for the proton transfer reaction leading to the diffusion of the ion. In the course of this process the two states transform from one to the other.[87,92] In Ref. 92, it is shown that the balance between these two states can change rather strongly when different density functionals are used, leading to large differences in the diffusion coefficient.

Without carrying out a full analysis of the simulation data as proposed by Tuckerman et al., we conclude that the integrated radial distribution function (Figure 3.2) and the current two-dimensional (2D) distribution functions suggest that in our simulation the tetrahedral configuration is mostly present. The broad distribution peak at r = 2.6-2.7 Å and θ around 105° agrees well with this observation. The water molecules accounting for this peak are H-bond donors for the OH^-, which can also be seen in the 2D OH–H distribution function representing the hydrogen atoms distribution around the central OH^- species (left panel in Figure 3.4). The peak at around r = 1.5 Å represents the corresponding hydrogen atoms. The distance of r = 1.5 Å is shorter than the O*–O distance meaning that the O–H bonds point towards the O* center.

The 2D distribution function used in this work also shows the formation of the elongated hydrogen bond with the OH^- being H-bond donor, as already suggested in Ref. 87. The corresponding oxygen atom of the water molecule appears as a peak in the 2D distribution function at separation distances r on the order of 3 Å and θ = 0-20°.

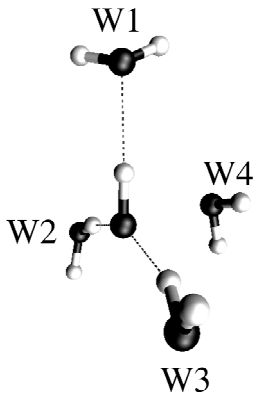

Figure 3.5 *Snapshot of the $OH^{\bullet}(H_2O)_4$ hydration complex in liquid water. The $OH^{\bullet}$ radical and the oxygen atoms from W1, W2, and W3 water molecules are approximately in one plane.*

Using a one-dimensional RDF, i.e. after integration over θ, this feature of the solvation shell would be undetectable (compare Figure 3.1 at r = 3 Å).

Considering the hydroxyl radical, being an H-bond *acceptor* analogous to the hydroxide ion, it forms hydrogen bonds with the neighboring water molecules (right panel in Figure 3.3, the broad peak at r = 2.8 Å and θ in the order of 90-120°). However, the peak in the distribution function only integrates to two, i.e. only two water molecules instead of the three found in the case of OH^-. As opposed to the hydroxide ion, the hydroxyl radical as an H-bond *donor* forms a strong hydrogen bond with a third water molecule, accounting for the well pronounced peak at around r = 2.8 Å and θ = 0° (see also Figure 3.5). In the original one-dimensional O–O RDF (Figure 3.1) these three water molecules account for the single peak at around 2.8 Å. The additional peak at 2.3 Å is now easily recognizable in the 2D distribution function at θ = 90°. The water molecule accounting for this peak is *not hydrogen bonded* to the $OH^{\bullet}$ and its hydrogen atoms account for the additional features around r = 2.5 Å with relatively broad distribution around θ = 90° in the OH–H 2D distribution function (Figure 3.4) and the additional peak in the O*–H RDF in Figure 3.2 mentioned before.

Thus the structure of the $OH^{\bullet}(H_2O)_4$ solvation complex can be illustrated in Figure 3.5 with the three (W1, W2, W3) water molecules being hydrogen bonded and the "additional" (W4) water molecule in close contact with the $OH^{\bullet}$. It can also be shown, that the O* and the H* atoms of the $OH^{\bullet}$ and the three oxygen atoms from W1, W2, and W3 are approximately in one plane. The connection line between O* and the oxygen atom of W4 is then perpendicular to this plane. The orientation of W4 itself is such that the molecule is approximately parallel to the plane containing the other three molecules.

The $OH^{\bullet}(H_2O)_4$ solvation complex displays rather different structural characteristics compared to the usual tetrahedral configuration of H_2O in liquid water and is rather stable in the course of the ab initio MD simulation (throughout the course

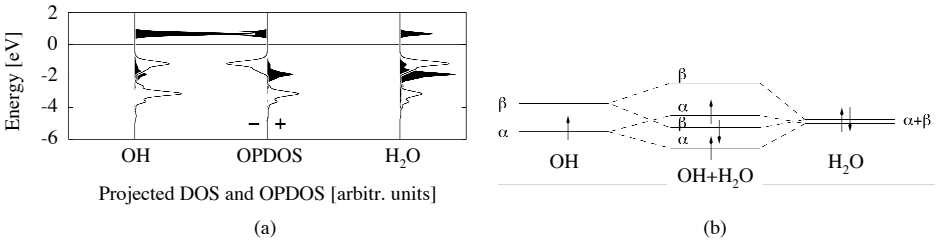

Figure 3.6 *Formation of a hemibond between OH• and a water molecule. (a) Projected density of states and OPDOS (Overlap Population Density of States). Solid lines correspond to the α electron states; filled curves correspond to the β electron states. The OPDOS data indicates the character of the corresponding state and is positive if the state is bonding for the interaction between the OH• (left) and H_2O (right), and negative if the state is antibonding. (b) Schematic representation of the formation of the hemibond.*

of our 32 ps simulation the same four water molecules form the first coordination shell in the described orientations). As already mentioned above, its formation causes disruption in the arrangement of liquid water. While the $OH^{\bullet}(H_2O)_4$ is internally well structured, it forms rather weak hydrogen bonds with the surrounding solvent molecules. Although the finite box size may have an effect on these results for the second solvation shell, we do note that this effect does not inhibit enhanced structure of the solvent, as in the case of OH^- this happens.

3.3.3. Bonding within the $OH^{\bullet}(H_2O)_4$ solvation complex

The flat arrangement of the three water molecules (W1, W2, and W3) around the OH• radical suggests that the central O* atom is in an sp^2 hybridization state with the two lone pair hybrid orbitals oriented towards the W2 and W3 molecules and taking part in hydrogen bonds as H-bond acceptors. The p_π molecular orbital (MO) is then perpendicular to this plane and points towards the W4 water molecule. From projected density of states and spin-density data (difference between up and down spin density) it can be shown that the p_π orbital is the singly occupied molecular orbital of the hydroxyl radical in this solvated state.

The short distance between the central O* atom and the W4 water molecule as well as the stability of this configuration suggest possible direct interaction between the two oxygens. To test this, for a selected configuration from the MD run we calculated the projected density of the Kohn-Sham electron states on local (atomic) p-projectors centered in either of the oxygen atoms of the OH• and of W4. The p-projectors are oriented along the axis connecting the two atoms, i.e. they coincide with the p_π MO of the OH• and the p_π ($1b_1$) MO of W4. The data presented in Figure 3.6 reveal the formation of a three-electron two-centered σ bond between the two oxygens. Of the resulting four spin-polarized molecular orbitals, three are occupied (2 bonding and 1 antibonding) and one is unoccupied (antibonding).

The relatively large split in the eigenvalues of more than 2 eV suggests a strong interaction. It has been shown however that the bond energy using the BLYP-DFT method is relatively small and comparable to the energy of a hydrogen bond (see for example Ref. 74 and references therein). This is because one of the occupied molecular orbitals is antibonding and destabilizes the system. It has to be stressed that the singly occupied p_{π} MO of the hydroxyl radical is tied down in this hemibond and this may have consequences for the activity of the $OH^{\bullet}$ and the process of the $OH^{\bullet}$ diffusion via hydrogen exchange reaction.

3.3.4. Diffusion and activity of the hydroxyl radical in liquid water

The structure and electronic properties of the solvated hydroxyl radical are of crucial importance for understanding the oxidation processes involving $OH^{\bullet}$ as an intermediate. If the unpaired electron in the p_{π} molecular orbital of the $OH^{\bullet}$ is tied down in a hemibond, this effectively inhibits the oxidative properties of the radical. The supposed mechanism of diffusion of $OH^{\bullet}$ in liquid water via a hydrogen exchange reaction can also be no longer efficiently operative.

It has to be pointed out that the diffusion mechanisms of hydroxyl radical and hydroxide ion in water are fundamentally very different. While for the OH^{-} the diffusion takes place via a *proton* exchange reaction with hydrating H_2O molecules, in the case of the $OH^{\bullet}$ radical the analogous process would be *hydrogen* exchange. In either case the necessary condition for the reaction to take place is that the hydrating H_2O taking part in the exchange process should have its O–H bond pointing towards the hydroxide, respectively hydroxyl species. As was shown by Tuckerman et al.,[87] OH^{-} forms (in its active state) three hydrogen bonds satisfying this condition. On the contrary, in the case of the $OH^{\bullet}$ radical only two bonds (those of W2 and W3, Figure 3.5) point towards the $OH^{\bullet}$, but neither of them can take part in a *hydrogen* exchange reaction. A hydrogen exchange reaction, which involves the transfer of a proton and an electron, could only take place if the associated water molecule forms a –presumably rather weak– H-bond via the singly occupied p_{π} MO of the radical. However, as seen from the current simulation, this event never occurs during the MD run because the p_{π} MO takes part in a hemibond with W4.

It is interesting to compare our results to previous studies comparing BLYP-DFT results with high level ab initio calculations[74-79] for small gas phase clusters of $OH^{\bullet}$ with a few water molecules. These cluster calculations raise two issues. In the first place they do not show the solvation pattern depicted in our Figure 3.5. For instance, with 4 or 5 water molecules surrounding $OH^{\bullet}$ in the gas phase cluster, the structure of Figure 3.5 is not formed, but with either BLYP or MP2 the $OH^{\bullet}$ forms only 2 or 3 hydrogen bonds to neighboring water molecules, and no hemibond.[74] So if the solvent molecules from the bulk liquid water surrounding the complex were not present, the structure of Figure 3.5 would rearrange, the hydrating water molecules W1, W2, W3, and W4 forming hydrogen bonds among themselves. Such rearrangement of the molecules would result in the destruction of the hydration complex of Figure 3.5. This

means that although the $OH^{\bullet}(H_2O)_4$ hydration complex does not posses an identifiable second coordination shell (see above), the presence of the solvent is still quite essential for the local structure of the hydrated $OH^{\bullet}$ and its stability over time. In the liquid phase the "unsaturated" hydrogen bonds of the complexing H_2O can be realized with water molecules from the second coordination shell. This can explain the differences between the current periodic DFT simulation and the previous cluster DFT data.[74]

In the second place calculations on small systems have shown that the BLYP density functional overestimates the strength of the three-electron two-center hemibonds.[74,77-79,91] However, on the basis of cluster calculations it has been argued that the differences between the two methods (DFT and high-level ab initio) diminish with increasing size of the system.[74] For instance, in the largest gas phase cluster considered, with 5 H_2O molecules, BLYP and MP2 yield very similar structures and hydration energies. However, this is not yet conclusive evidence that in very large clusters, or for $OH^{\bullet}$ in bulk water, the difference between BLYP and MP2 would also be negligible. In fact, in small clusters the geometry of the cluster is dictated by the requirement of forming as many internal hydrogen bonds as possible, which in liquid water would normally be formed with water molecules of the second coordination shell. As long as no hemibond is present, which is the case in the gas phase clusters with 4 or 5 water molecules surrounding $OH^{\bullet}$, there will not be a marked difference between BLYP and MP2, since the H-bonds in BLYP and MP2 are very similar. When in a larger cluster a hemibond *is* present, BLYP may still overestimate its strength and the equilibrium between hemibonded and hydrogen bonded (to the unpaired electron) structures may be biases towards the hemibonded one –we indeed find the hemibonded structure exclusively on the time scale of our simulation. Nevertheless, we feel our bulk simulation has revealed a solvent coordination of the $OH^{\bullet}$ radical (see Figure 3.5) that is quite plausible for at least a large portion of the time, and will hinder the structural diffusion of the hydroxyl radical in water. To what extent, the BLYP functional overestimates the strength of the hemibond in bulk solvation is a question that remains open.

3.4. Conclusion

The presented results of Car-Parrinello molecular dynamics of $OH^{\bullet}$ in liquid water reveal the formation of a relatively stable first solvation shell of the radical. The $OH^{\bullet}$ species is bound to three neighboring water molecules via hydrogen bonds. The unpaired electron of the radical is tied up in a three-electron two-center hemibond with a fourth neighboring water molecule. This suggests that the supposed diffusion mechanism of $OH^{\bullet}$ via a hydrogen exchange reaction may not be efficiently operative in these conditions. The extent of this effect may be partially overestimated, though, by the tendency of the BLYP exchange-correlation density functional to overestimate the strength of the hemibond. Nevertheless, we believe this is an important finding with large implications on the diffusion mechanism of the hydroxyl radical.

Further examination of the structural properties and bond strength in this system in comparison with post-Hartree-Fock calculations is necessary. With such information

available it may be possible to construct an accurate model for the hemibonding. Constrained dynamics along a reaction coordinate from the water molecule hemibonded to H-bonded via the singly occupied π MO of the radical could then provide crucial information on what should be the first step in the diffusion mechanism by H abstraction from the water molecule.

3.5. Epilogue

Shortly after we finished this work, comparable work was published by Khalack et al.[93], also using the BLYP functional. They also observed a hemibonded water molecule, but in their simulation (using a simulation box of 9.8486 Å instead of 9.865 Å) this structure seems to be somewhat less stable and only present about half the simulation time. In a simulation of 72 ps, they observed one hydrogen transfer to the $OH^{\bullet}$, for which a hydrogen bond was formed with the singly occupied orbital in a tetrahedral configuration. Also Khalack et al. stress that this is a very rare event.

Because the overestimation of the strength of hemibonds by DFT methods is believed to be caused by self-interaction errors, shortly later VandeVondele et al.[94] studied the $OH^{\bullet}$ in water system with Self-Interaction Corrected (SIC) DFT. They found that indeed the abundance of the hemibonded structure is overestimated by the BLYP functional. In their self-interaction corrected simulations, the hemibond was hardly formed, but also hydrogen bonds with the unpaired electron were hardly formed. The $OH^{\bullet}$ radical would accept between one and two hydrogen bonds at the sp^2 lone pairs (cf. W2 and W3 in Figure 3.5), and the unpaired electron is, in fact, avoided by the solvent water molecules: a hydrophobic interaction occurs. As a result, again, hydrogen transfers to the $OH^{\bullet}$ radical are rare: at most once in simulations of 10 ps.

The conclusion is that, indeed, the strength of the hemibond is overestimated by the BLYP functional, and so is its abundance. Nevertheless, our conclusion that the structural diffusion of the $OH^{\bullet}$ radical is very slow because no hydrogen bonds are formed with the unpaired electron has been confirmed. Hydrogen transfer can only occur when this hydrogen interacts with the unpaired electron of $OH^{\bullet}$.

4.

Oxidation of methanol by FeO^{2+} in water: gas phase calculations with microsolvation and MD simulations in solution*

Abstract:

We have investigated the mechanism of methanol oxidation to formaldehyde by ironoxo (FeO^{2+}), the alleged active intermediate in the Fenton reaction. The most likely reaction mechanisms have been explored with Density Functional Theory (DFT) calculations, using the BLYP functional. Calculations were performed on microsolvated clusters in the gas phase, and, for a selected set of mechanisms, constrained Car-Parrinello Molecular Dynamics (CPMD) simulations in water solution were performed. Helmholtz free energy differences have been calculated using thermodynamic integration in a simulation box with 31 water molecules at 300K.

The mechanism of the reaction was investigated with an emphasis on whether FeO^{2+} attacks methanol at a C–H bond or at the O–H bond. We conclude that the most likely mechanism is attack by the oxo oxygen at the C–H bond ("direct CH mechanism"). This is related to the special electronic structure of FeO^{2+}(aq): The FeO^{2+} moiety does not accept hydrogen bonds at the oxo oxygen, but acts as electron acceptor by way of its very low-lying LUMO. The C–H bond of methanol, more than the O–H bond, is activated by the electron donor–acceptor interaction with FeO^{2+}. We have calculated an upper bound for the reaction free energy barrier in solution of 50 kJ/mol for the CH hydrogen transfer, after which transfer of the OH hydrogen proceeds spontaneously. An alternative mechanism, starting with coordination of methanol directly to Fe ("coordination OH mechanism"), cannot be ruled out, as it involves a reaction free energy barrier in solution of 44 ± 10 kJ/mol. However, this coordination mechanism has the disadvantage of requiring a prior ligand substitution reaction, to replace a water ligand by methanol.

Because of the strong acidity of $[FeO(H_2O)_5]^{2+}$, we have also investigated the effect of deprotonation of a first-shell water molecule. However, this was found to increase the barriers for all mechanisms.

---

* This chapter is based on: M.J. Louwerse, P. Vassilev, and E.J. Baerends, *J. Phys. Chem. A* **112** (2008) 1000-1012. Reproduced with permission; Copyright 2008 American Chemical Society.

4.1. Introduction

As early as in 1876, H.J.H. Fenton discovered the strongly accelerating effect of Fe^{2+} ions on oxidation by hydrogen peroxide,[1] which later turned out to be a catalytic process. Since then, this mixture of hydrogen peroxide and ferrous ions in water has become known as Fenton's reagent, and it can efficiently oxidize most organic compounds. Nowadays, Fenton's reagent is used in a broad range of industrial applications, like the oxidation of wastewater,[2] the hydroxylation of aromatic substrates,[4] and many other reactions.

Despite the wide variety of applications, however, the mechanism of the Fenton reaction remains controversial.[5-9] Experimentally it has been very difficult to determine whether free $OH^{\bullet}$ radicals are the exclusive intermediates in the reaction, whether they play an important but non-exclusive role, or whether the organic substrate is attacked by another intermediate altogether. The prime candidate for an alternative intermediate is the FeO^{2+} ion.[22] Using both calculations on the microsolvated system in the gas phase and Car-Parrinello Molecular Dynamics (CPMD) simulations of $Fe^{2+} + H_2O_2$ in water solution (periodic systems with 31 water molecules per unit cell), Ensing et al.[14-17] have provided evidence that the most important active intermediate is the FeO^{2+} species. It is commonly assumed (and confirmed in these simulations) that the first step of the reaction is the homolytic dissociation of the O–O bond of a coordinated H_2O_2, producing an OH^- ligand (taking one electron from iron) and an $OH^{\bullet}$ radical. However, as Ensing et al. have emphasized, the formation of a free $OH^{\bullet}$ radical is energetically unfavorable: the bond dissociation energy of H_2O_2 of ca. 250 kJ/mol is only partly compensated by the stronger bonding of the OH left behind to the Fe center (formally OH^- to Fe^{3+}), which is only ca. 160 kJ/mol stronger than the coordination of H_2O_2 to Fe^{2+}.[16] Instead, the $OH^{\bullet}$ radical immediately (either directly or through a H-bond chain) extracts a hydrogen from a neighboring coordinated water, creating another OH^- ligand. Since this uses another electron from iron, Fe^{IV} is created. The two OH^- ligands rearrange to a water ligand and an oxo ligand, creating the FeO^{2+} ion:

$$Fe^{2+} + H_2O_2 \rightarrow [Fe^{III}OH]^{2+} + OH^{\bullet} \rightarrow [Fe^{IV}O]^{2+} + H_2O \qquad (4.1)$$

Iron(IV)oxo species are also found in other types of systems. In heme-containing enzymes like P450,[95] ironoxo species have long been accepted as intermediates, and such intermediates are also regularly found in non-heme iron enzymes.[96-98] The literature covering these enzyme processes is extensive, and includes many calculations.[e.g.99-102] Inspired by these biochemical FeO systems, some specific multidentate ligands have been designed to form ironoxo compounds, and indeed ironoxo formation has been found in these systems.[103-105] However, we note that all synthetic ironoxo compounds have a low-spin ground state, unlike the aqueous FeO^{2+} studied in this thesis ($S = 1$ vs. $S = 2$). Recently though, the high-spin $[FeO(H_2O)_5]^{2+}$ studied here has also been characterized experimentally.[41]

In that paper, [41] Pestovsky et al. claim that FeO^{2+} cannot be the active species in Fenton chemistry, because the resulting products differ, but it has been counter argued by Kremer that the experimental evidence is consistent with an FeO^{2+} intermediate.[42]

Whether or not the ironoxo group is the key intermediate in the Fenton reaction, the reactivity of the FeO^{2+} moiety is of considerable interest. In the current chapter, we study the reactivity of FeO^{2+} in water solution, using DFT and Car-Parrinello simulations. Ensing et al. already studied the reaction with methane,[106] as a prototype for aliphatic hydroxylations, which occur via an H-abstraction/oxygen rebound mechanism as proposed by Groves et al. for aliphatic hydroxylations.[107,108] However, as is also experimentally known, the C–H bond in methane is too strong to make this an efficient reaction. We now investigate the mechanism of another typical reaction for the Fenton reagent: the oxidation of an alcohol to an aldehyde, taking as prototype the oxidation of methanol to formaldehyde. In experimental conditions the reaction continues after the oxidation to formaldehyde eventually producing CO_2,[109] but in our setup we only concentrate on the first step. In our simulations, there is only one H_2O_2 molecule available and the reaction stops at formaldehyde:

$$FeO^{2+} + CH_3OH \rightarrow Fe^{2+} + CH_2O + H_2O \qquad (4.2)$$

Most theoretical studies of the oxidation by simple ironoxo systems have focused on the related FeO^{+} species, using the bare (gas phase) species.[110-116] Also the oxidation of methanol to formaldehyde by the bare FeO^{+} has been studied.[112] Recently, the electronic structure of FeO^{2+} has been studied for a variety of complexes,[117-124] including $[FeO(H_2O)_5]^{2+}$.[117] Here, we study oxidation by FeO^{2+}, including first-shell water ligands, both in the gas phase and in water solution. The gas phase calculations are especially useful for precise analyses of the electronic structure aspects of the reaction with FeO^{2+}, and for comparison with other gas phase calculations and experiments. The combination of gas phase calculations and simulations in solution give a remarkable insight into the solvent effects in this reaction.

4.1.1. Possible mechanisms

For the oxidation of methanol to formaldehyde by FeO^{2+} two steps are required: The OH hydrogen atom and one CH hydrogen atom need to be abstracted from the methanol molecule. The possible mechanisms can roughly be divided into four groups: The first distinction between these groups is that the first step may either be an O–H bond breaking or a C–H bond breaking. The second distinction is whether the first step in the reaction involves direct complexation of methanol to, and reaction with, the oxo oxygen of the FeO^{2+} moiety, or whether the first step is a ligand substitution reaction, in which a coordinated water ligand is replaced by methanol. We thus differentiate between a “direct OH mechanism”, a “direct CH mechanism”, a “coordination OH mechanism”, and a “coordination CH mechanism”.

These four possibilities are depicted in Figure 4.1: In the direct OH mechanism (**1a**) and the direct CH mechanism (**1b**) an H is first transferred to the oxo group, forming a coordinated OH^{-} and an intermediate radical. Next, the other hydrogen is transferred to the coordinated OH^{-} to form an H_2O ligand. In the coordination mechanisms the methanol molecule first coordinates to the iron, replacing a coordinated water molecule. Note that in the coordination OH mechanism (**1c**) the intermediate structure

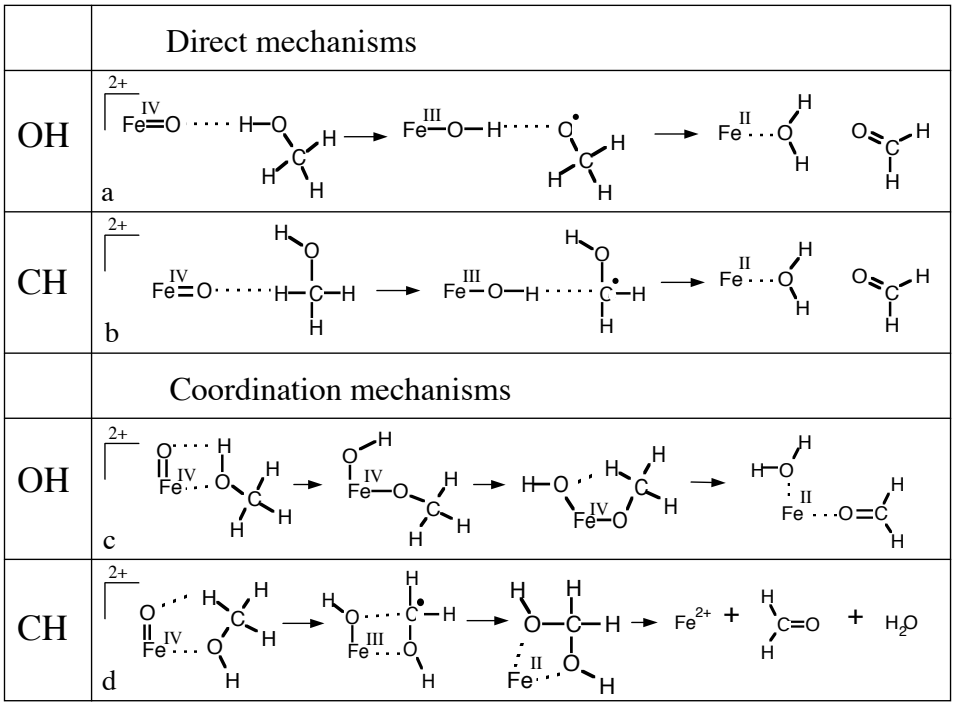

Figure 4.1 *The four groups of possible mechanisms for the reaction of FeO^{2+} with methanol. For some mechanisms variations are possible because of the influence of the solvent.*

does not involve a radical, because the unpaired electron on the $CH_3O^{\bullet}$ fragment combines with an unpaired electron from the Fe ion resulting in a CH_3O^- ligand. Finally, in the coordination CH mechanism (**1d**) the second hydrogen (the OH hydrogen) cannot be transferred directly. In this case, a bond between the just formed OH ligand (bound as OH^- to the now formally Fe^{III} ion) and the C atom of the $^{\bullet}CH_2OH$ fragment may be formed (cf. the oxygen rebound mechanism in the oxidation of methane to methanol), so that a di-alcohol is formed. This disintegrates in water solution to yield formaldehyde and H_2O.

Actually, in the *direct* CH mechanism the di-alcohol could also be formed via an oxygen rebound mechanism. However, we find that in the direct CH mechanism, there is a barrierless second step transfer of the OH hydrogen to the just formed OH ligand with which no alternative mechanism could compete.

Some additional variations on the mechanisms could occur when the solvent water molecules are taken into account, because in some cases the hydrogen abstraction can take place via a H-bond chain through the water (as in Ref. 15-17), or the solvent water molecules can have other bridging functions. Because of these possible chain mechanisms, it is important to include the solvent water molecules explicitly; simpler models for water like a continuum model or a representation of water–water and

water–solute interactions with model potentials, as in MM or QM-MM simulations, can never model such chain reactions correctly.

Finally, there could also be a pH effect on the reaction, because $[FeO(H_2O)_5]^{2+}$ is rather acidic. It is known that the optimal pH range for the Fenton reaction is around pH = 3-5,[2,109] and the pK_a of FeO^{2+} is around pK_a = 2,[125] so deprotonation of a first-shell water molecule may occur during the process. Therefore, we also studied the effect deprotonation of $[FeO(H_2O)_5]^{2+}$ has on the reaction mechanisms.

We first study all of these mechanisms in the gas phase, with the first coordination shell of water molecules around the iron ion included in the calculations (microsolvation). Each mechanism that appears viable according to the gas phase calculations has been studied with large-scale Car-Parrinello simulations at 300 K with 31 water molecules in a periodic box, in addition to FeO^{2+} and methanol. We performed thermodynamic integration for each mechanism by doing simulations for a series of fixed (constrained) values of the reaction coordinate, in order to obtain free reaction energies. Finally, the effect on the mechanisms of deprotonation of $[FeO(H_2O)_5]^{2+}$ is studied.

Comparing the gas phase calculations to the simulations in solution we find rather large differences. The physical origin of this interesting phenomenon, which is related to differential dielectric screening effects on the one-electron levels of the charged (FeO^{2+}) and neutral (CH_3OH) reactants, has been further explored in Chapter 5.

4.2. Methods

Both the microsolvated gas phase calculations and the Car-Parrinello simulations were performed with Density Functional Theory (DFT), using the BLYP[65,66] density functional. This functional was chosen because it performs well for liquid water,[50] and it has been shown to be a good choice for calculating reaction energies and transition states for transition metal complexes.[126] Although it has been shown that most functionals of this type tend to underestimate the relative stability of high spin states,[124,127,128] this is not a problem here, because the spin state is constant (S = 2) throughout all our calculations.

The (microsolvated) gas phase calculations were performed with the ADF (Amsterdam Density Functional) package,[60-63] with all electrons included in the calculations, and using large Slater type orbital (STO) basis sets: a quadruple-ζ basis set with four sets of polarization functions (QZ4P) for iron, and triple-ζ basis sets with two sets of polarization functions (TZ2P) for the other atoms. The calculations were corrected for relativistic effects using the Zero-Order Regular Approximation (ZORA)[64] approach.

In the gas phase calculations the first coordination shell of water around the iron ion was included in the calculations (microsolvation). The iron ion is six-fold coordinated, so 5 water molecules were taken into account in the calculations of the direct mechanisms, and 4 water molecules in the coordination mechanisms.

All geometries were fully optimized, and the transition states were determined and characterized in the usual way. Reaction coordinates were also calculated for the transition states, for comparison with the simulations in solution.

The Car-Parrinello molecular dynamics simulations were performed with the PAW package, using the Projector Augmented Wave Method.[18] We used a system consisting of one FeO^{2+} ion, one methanol molecule, and 31 water molecules in a periodic cubic box of 10.1 Å, with all hydrogen atoms replaced by deuterium isotopes. The MD time step was 6.5 a.u. (0.157 fs), and the fictitious mass for the wavefunction dynamics was 100 a.u. At each time step, the time derivatives (fictitious velocities) of the wavefunction coefficients were scaled down with 0.005%, and in some simulations this was increased to 0.01% or 0.02% in order to keep the system on the Born-Oppenheimer surface. The cutoff for the plane wave basis set was 30 Ry (408 eV) for the wavefunctions and 90 Ry (1225 eV) for the charge density.

The PAW projectors for the atoms were constructed with the PAW atomic setups generation program with the 1s electrons of oxygen and carbon, and the 1s, 2s, and 2p electrons of iron selected as frozen cores. We constructed the following projectors: for hydrogen one s-projector with E = –0.24001 a.u. and R_c = 0.557 a.u.; for oxygen one s- and two p-projectors with E_s = –0.87577 a.u., $E_{p,1}$ = –0.33159 a.u., $E_{p,2}$ = 0.27777 a.u., and R_c = 1.267 a.u.; for carbon one s- and two p-projectors, with E_s = –0.50018 a.u., $E_{p,1}$ = –0.19248 a.u., $E_{p,2}$ = 0.27777 a.u., and R_c = 1.33 a.u.; and for iron two s-, two p-, and three d-projectors with $E_{s,1}$ = –3.44446 a.u., $E_{s,2}$ = –0.19193 a.u., $E_{p,1}$ = –2.19899 a.u., $E_{p,2}$ = 2.226 a.u., $E_{d,1}$ = –0.272 a.u., $E_{d,2}$ = 0.32717 a.u., $E_{d,3}$ = 2.0 a.u., R_{core} = 1.458 a.u., and R_c = 1.658 a.u.

This set of parameters (without using friction on the wavefunction dynamics) was tested for liquid water and produced a stable constant energy (NVE) simulation, conserving the total energy to within 0.005 a.u. for a simulation length of 2 ps. The frictions on the wavefunction dynamics were necessary because in the current system the band gaps are often much smaller than in liquid water. The same settings have been used previously in the simulation of the $OH^{\bullet}$ radical in water (Chapter 3).

To obtain Helmholtz free energy differences in solution, we performed thermodynamic integrations[129] with the relative position of the abstracted H atom between the methanol and the oxo oxygen as the constrained reaction coordinate, ξ. For instance, for the CH mechanisms:

$$\xi = \frac{R_{CH}\cos\theta}{R_{CO}}, \qquad (4.3)$$

where R_{CH} is the C–H bond distance, R_{CO} the C–O bond distance, and θ the angle between these bonds (Figure 4.2). Note that the C–O distance itself is not constrained, and the hydrogen atom can still move freely in the plane perpendicular to the C–O bond. Typically, the value for this constraint changes

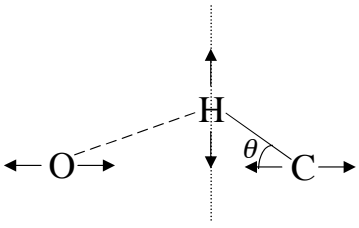

Figure 4.2 *Degrees of freedom at reaction coordinate* ξ.

from 0.3 to 0.7 during the first reaction step. We did constrained simulations at all intermediate values of ξ with steps of 0.05, and integrated over the constrained force to obtain Helmholtz free energies.

This type of calculation is very sensitive to hysteresis: the force of constraint at a specific value of the reaction coordinate is often different along the forward path (stepwise increase of the reaction coordinate) to that along the reverse path (stepwise decrease of the reaction coordinate);[130] this is caused by the tendency of the solvent to respond very slowly to changes in the reaction coordinate. To minimize the hysteresis we used relatively long equilibration periods after each change in the reaction coordinate. To be able to estimate the hysteresis properly, we did the simulations strictly in consecutive order: the equilibration at $\xi = 0.5$ was started from the endpoint of the equilibration at $\xi = 0.45$, which was started from the endpoint of the equilibration at $\xi = 0.4$, and so on. Furthermore, we simulated one series (the direct OH mechanism) in both forward and backward order to quantify the hysteresis by comparing the two series.

The scheme used for the equilibration was as follows: Each new constraint value was reached by slowly changing the reaction coordinate, ξ, during 1000 time steps (0.157 ps). The temperature was restored to $T = 300$ K by employing a thermostat on the ionic degrees of freedom with an oscillation period of 7500 a.u. and a friction on the Nosé variable of 0.05. This thermostat was used for 4 ps, followed for 2 ps by a thermostat with an oscillation period of 60000 a.u. and a friction of 0.001. The latter thermostat was also used for the data collection in simulations ranging from 3 to 14 ps in length.

Strictly speaking constrained simulations are not sampling a true NVT ensemble, but a *constrained* NVT ensemble, which can slightly bias the constraint force. Therefore, we corrected for this bias with the method of Refs. 131 and 132 before calculating the statistical averages.

Standard errors were estimated using the method given in Ref. 133: In molecular dynamics simulations most fluctuations are caused by thermal movement, so the standard error cannot directly be calculated from the standard deviation. The method used is to take block averages over 1, 2, 4, 8, 16, etc. data points and then the standard deviation of these block averages is calculated. When the resulting standard errors are plotted against the size of the blocks, the curve forms a plateau and the value of this plateau gives the correct statistical standard error.

4.3. Results for microsolvated FeO^{2+} in the gas phase

First, we will discuss the microsolvated ironoxo species $[Fe^{IV}O(H_2O)_5]^{2+}$ and its propensity for complexation with reactants. A full analysis of the orbitals and the orbital energies in $[Fe^{IV}O(H_2O)_5]^{2+}$ can be found in Ref. 117. A schematic picture for FeO^{2+} is shown in Figure 4.3.

The ironoxo species, with its 2+ charge, has a very low-lying LUMO (the $3\sigma^{*\uparrow}$ orbital), which makes it a very strong electron acceptor. Although the empty $3d^{\downarrow}$ (1δ) orbitals are even lower in energy, they are not as important because they are shielded

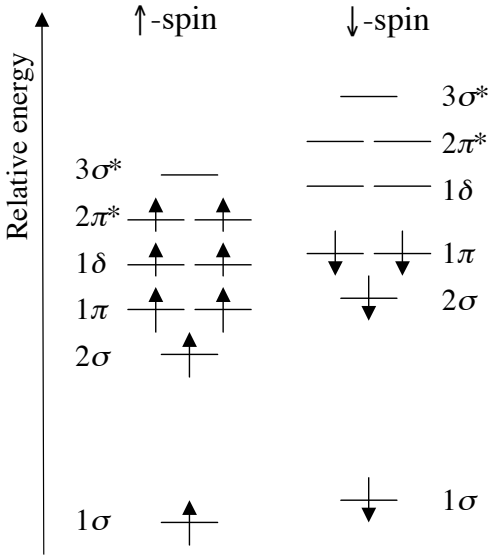

Figure 4.3 *Qualitative molecular orbital scheme for FeO^{2+}.*

by the water ligands, and, thus, not accessible for interactions. The up-spin $3\sigma^*$ orbital, the σ^* antibonding combination of the Fe-$3d_{z^2}$ orbital and the O-$2p_z$ orbital (with the Fe–O bond chosen as the z-axis), reaches spatially beyond all the occupied orbitals on the oxygen side. Therefore, it is of particular interest when any molecule approaches the ironoxo oxygen. Normally, one would expect the oxygen atom to act as a hydrogen bond acceptor, but when a potential hydrogen bond donor approaches, its O–H σ bond orbital will start to overlap with the strongly electron-withdrawing FeO^{2+} LUMO. As a result, a $\sigma(OH) \rightarrow 3\sigma^*(FeO^{2+})$ charge transfer interaction will occur rather than the formation of a hydrogen bond, which is characterized by the reverse charge transfer (O-lp $\rightarrow \sigma^*(OH)$).

As a result, complexation to the oxo oxygen does not show any preference for H-bond donating groups, and, moreover, the interactions are much stronger than for hydrogen bonds. Strong charge transfer interactions with the $3\sigma^*$ orbital occur even more readily for C–H bonds or oxygen lone pairs than for the lower lying O–H bond orbitals: For water we find an interaction energy via an oxygen lone pair (so not in H-bonding orientation) of 43 kJ/mol, and methanol binds via its OH group with 57 kJ/mol (see Figure 4.4), and via a C–H bond even with 70 kJ/mol (see Figure 4.5). These interaction energies already suggest that $[FeO(H_2O)_5]^{2+}$ will indeed abstract hydrogen atoms very easily, and can be expected to have a preference for C–H bonds over O–H bonds. In Chapter 5 we perform a detailed investigation of these electronic structure features of the interaction of $[FeO(H_2O)_5]^{2+}$ with organic substrate molecules.

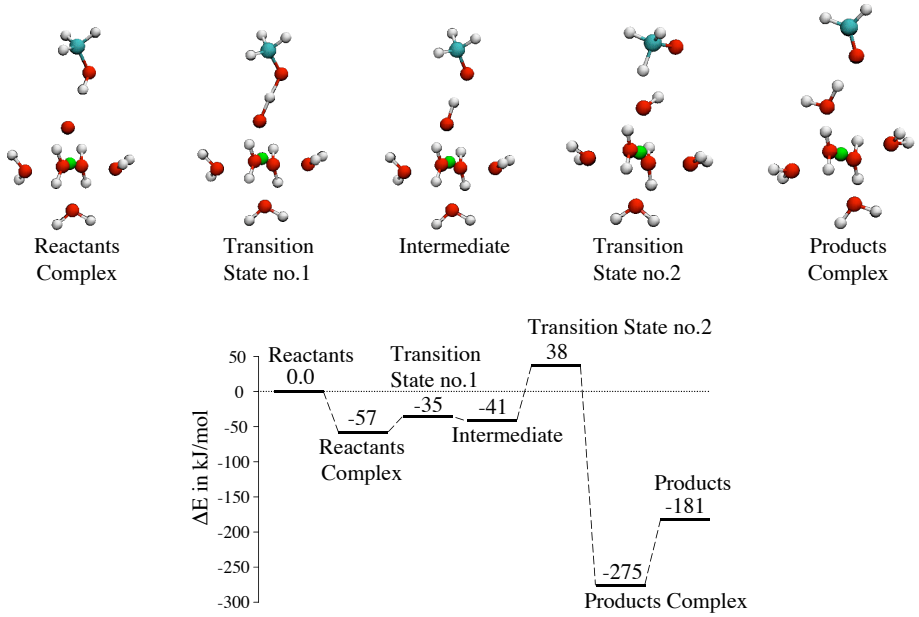

Figure 4.4 *Microsolvated gas phase results for the direct OH mechanism.*

4.3.1. The direct mechanisms in the gas phase

The results for the direct OH mechanism in the microsolvated gas phase are given in Figure 4.4, and for the direct CH mechanism in Figure 4.5. The first step of the direct OH mechanism, the abstraction of the OH hydrogen, has a relatively small barrier of 22 kJ/mol relative to the reactants complex, with the transition state at reaction coordinate ξ = 0.51. However, the intermediate product, a $CH_3O^{\bullet}$ radical complexed to $[FeOH(H_2O)_5]^{2+}$, is only stable by 6 kJ/mol with respect to the transition state, and is still unstable by 16 kJ/mol with respect to the reactants complex. Furthermore, the barrier of the second step, the abstraction of the methyl H, is rather high (79 kJ/mol), rendering the direct OH mechanism in the gas phase unlikely, though not impossible.

The direct CH mechanism, on the other hand, hardly shows any barrier in the microsolvated gas phase calculations. The first step, the abstraction of a methyl hydrogen atom, has a barrier of less than 2 kJ/mol (at reaction coordinate ξ = 0.45). In the transition state the incipient formation of the flat $^{\bullet}CH_2OH$ radical is visible (see Transition State no. 1 in Figure 4.5). After crossing this low barrier the energy goes down by some 54 kJ/mol and the flat $^{\bullet}CH_2OH$ radical is formed; however, a stable intermediate structure is not reached because the second step, the abstraction of the hydroxyl hydrogen, appears to have no barrier at all: When the intermediate structure with the $^{\bullet}CH_2OH$ radical is optimized, the hydroxyl H rotates towards the FeOH, and it is abstracted spontaneously, even in a regular geometry optimization calculation. The energy and geometry of the intermediate structure presented here are thus only estimates based on the region of phase space where the energy surface is almost flat.

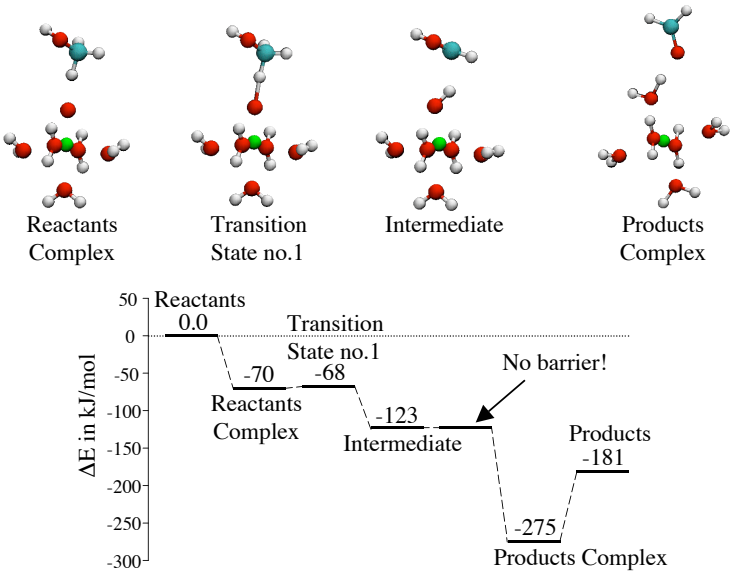

Figure 4.5 *Microsolvated gas phase results for the direct CH mechanism. The second step has no barrier, so the intermediate structure is not a fully optimized minimum but a configuration where the energy surface is almost flat. Energies are given in kJ/mol.*

It should be noted that this second step is different from the so-called oxygen rebound type mechanism, which is familiar from heme iron oxidation catalysis and also operates in methane oxidation by the FeO^{2+} ion.[106] That mechanism also starts with the abstraction of an aliphatic H. However, the newly formed OH group then binds to the carbon atom of the organic radical, retaining a (weaker) coordination bond to the Fe by way of the oxygen lone pair of the formed alcohol. In the current case, in which an OH group is already present, this would mean that a di-alcohol would be formed (which would yield formaldehyde by splitting off a water molecule). However, from our findings it appears that for the oxidation of a primary alcohol, after the formation of the $^{\bullet}$CRHOH fragment, it is easier to transfer the hydroxyl H to FeOH to form a water ligand and the RCHO product.

In the products complex, the formaldehyde molecule binds rather strongly (93 kJ/mol) to the newly formed water ligand, much stronger than by a simple hydrogen bond. This phenomenon has been observed before[14] for complexation by "hydrogen bonding" of a second sphere molecule to a first sphere water ligand of the strongly positive charged $[Fe(H_2O)_6]^{2+}$ complex. The bond is much stronger than a normal hydrogen bond because both the electrostatic contribution and the donation into the O–H σ^* orbital of the coordinated H_2O become much larger.

In conclusion, based on our microsolvated gas phase calculations, the direct CH mechanism seems to have high probability, with a spectacularly low barrier. This very low barrier (strikingly lower than for H abstraction from the hydroxyl group) is caused by the strong charge transfer from the C–H bond orbital into the FeO^{2+} LUMO. This

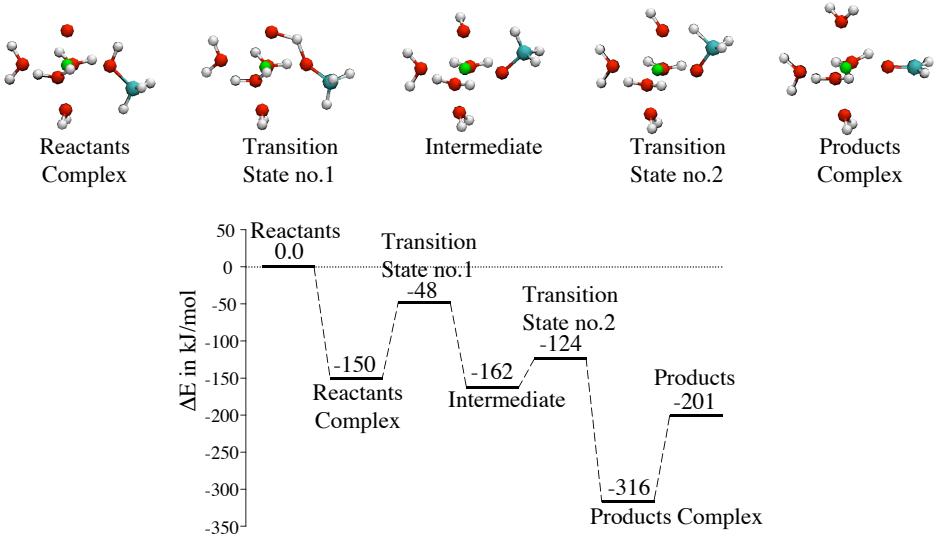

Figure 4.6 *Microsolvated gas phase results for the coordination OH mechanism. Note that the zero-level (the free reactants) includes a vacant coordination site.*

charge transfer already exists in the reactants complex, and increases strongly as the C–H bond lengthens, since the σ(C–H) orbital rises in energy. The charge transfer interaction of σ(C–H) with the FeO^{2+} LUMO is then enhanced, which compensates for much of the strain energy of stretching the C–H bond. This is a typical orbital mechanism for bond breaking/forming.

4.3.2. The coordination mechanisms in the gas phase

For the complexation of methanol to the oxo oxygen in the direct mechanisms we found unexpectedly strong charge transfer interactions, in particular for approach with a C–H bond. For coordination to the iron, however, it is no surprise to find strong coordinative bonds. In fact, the coordination to Fe is much stronger than the complexation to the oxo oxygen: When the methanol molecule coordinates with its OH group next to the oxo oxygen, which is the right configuration for the coordination OH mechanism (Figure 4.1c), the coordinative bond energy is 150 kJ/mol. When the methanol coordinates with the CH_3 group next to the oxo oxygen, the configuration for the coordination CH mechanism (Figure 4.1d), it is 154 kJ/mol. However, to make coordination to the iron ion possible, a strongly bound water molecule first needs to be removed, which costs 110 kJ/mol in the gas phase (N.B. these three gas phase values were calculated with 4 additional water ligands coordinated to the iron).

The results for the coordination OH mechanism in the microsolvated gas phase are given in Figure 4.6. The first step (after coordination) is again the abstraction of the hydroxyl hydrogen, but in the case of coordinated methanol this abstraction has a high barrier of 103 kJ/mol. In the coordination CH mechanism the first step also has a high barrier, namely 95 kJ/mol. Apparently, in both cases, coordinated methanol cannot

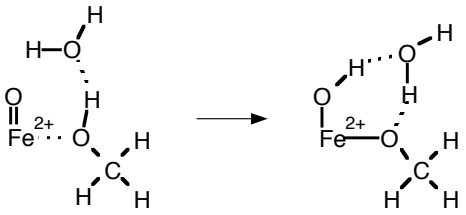

Figure 4.7 *The first step of the coordination OH mechanism can be facilitated by an additional bridging water molecule. The barrier is lowered considerably by the bridging function of the water molecule, from 103 kJ/mol to 31 kJ/mol. In this case it is not a hydrogen atom but a proton that is transferred.*

make the right angle with the Fe–O bond, and does not have sufficient overlap with the LUMO, which is a σ orbital along the FeO axis, to become activated for hydrogen abstraction. As a result, these barriers are too high to give reasonable mechanisms.

However, in the case of the coordination OH mechanism a bridging water molecule, which is hydrogen bonded to the methanol hydroxyl group, could lower the barrier via a concerted reaction (Figure 4.7): When the coordinated methanol molecule makes a hydrogen bond to a water molecule from the solution, this water molecule could in turn interact with the LUMO, with its high amplitude at the oxo site. Then, while the ironoxo abstracts an $H^{\bullet}$ from the water, the water could in turn abstract the hydrogen of the methanol OH group. This would be facilitated by the coordination of the methanol OH group to the iron, since a strong coordinative bond to the resulting $CH_3O^{\bullet}$ radical could be formed (forming a (formally) CH_3O^- ligand). We find, however, that the reaction occurs in two discernable steps, and starts at the coordinated methanol: first an H is transferred to the intermediary water, and then the transfer of (another) H from the water to the oxo takes place. The two barriers have practically the same height, with a very shallow minimum in between. The height of the barriers is only 31 kJ/mol, much reduced compared to the 103 kJ/mol of the direct transfer of the hydroxyl H to the oxo.

The end result of this step is formally an Fe^{IV} ion with an OH^- ligand and a CH_3O^- ligand. This situation can be reached simply by heterolytic splitting of the O–H bond of methanol, the resulting H^+ being transferred to the formally 2– oxo group to form OH^-, leaving CH_3O^- behind. Alternatively, a homolytic splitting would result in $CH_3O^{\bullet}$ and a hydrogen atom. The latter would supply an additional electron to the oxo group. In order for the OH^- ligand to be formed, the electron would have to move to the Fe center and then to $CH_3O^{\bullet}$ to generate the CH_3O^- ligand. On the Born-Oppenheimer surface such electron redistributions do not occur in time but simultaneously with the changes of the atomic positions. Since the electron density is easily redistributed in the complex during the reaction, it is not easy to establish which one of these two pictures is more accurate. We find that the transferred hydrogen (from methanol to the water molecule) bears no spin polarization (0.03), but also does not have a full positive charge: The charge increase of the $H_3O^{\delta+}$ compared to the charge of the water molecule before the reaction (+0.2) is only +0.5 according to Mulliken[134] and +0.3 according to Hirshfeld[135] and Voronoi[136] charge analyses. When the (other) H of $H_3O^{\delta+}$ moves on

to the oxo oxygen, the charge on the H_2O molecule drops to +0.2 again. It appears that the picture of H^+ dissociation from methanol is not wrong. It should be kept in mind that the redistribution of charge (due to small changes in the many orbitals that build the total charge density) prevents the development of full (almost integer) charges. In fact, precisely the same happens if we put a proton in a water solution. We have found in Car-Parrinello simulations of a proton in water that the proton continuously forms an $H_3O^{\delta+}$ ion, with $\delta^+ = +0.43 \pm 0.02$. The present charge analyses therefore suggest that heterolytic splitting of the O–H bond takes place.

The second step in the coordination OH mechanism is the transfer of a methyl H to the just formed OH^- ligand. Since a neutral H_2O ligand is formed, and a neutral formaldehyde ligand, formally two electrons go to Fe, changing Fe^{IV} into Fe^{II}. The barrier for this methyl H transfer is not very high (38 kJ/mol at reaction coordinate ξ = 0.46).

In conclusion, the microsolvated gas phase calculations suggest that, with a bridging water molecule facilitating the first step, the coordination OH mechanism is possible. This mechanism is thus also considered in the Car-Parrinello simulations.

For the coordination CH mechanism it is not possible to lower the H abstraction barrier with a bridging water molecule, because the C–H bond does not form hydrogen bonds with the water molecules. The coordination CH mechanism is therefore not considered any further.

For easy reference we collect all the results for the microsolvated system in the gas phase in Table 4.1, as well as the Car-Parrinello results and the results for the deprotonated system to be discussed in a later section.

Table 4.1 *Reaction barriers and (free) energy differences for all direct and coordinated mechanisms (see Figure 4.1). (Free) energies are given as difference with the previous state and are given in kJ/mol. Note that there may be rounding differences when comparing to the absolute energies.*

	Reactants complex	Transition state no.1	Intermediate	Transition state no.2	Products complex	Products
Gas phase						
Direct CH mechanism	-70	2	–54	0	–152	93
Direct CH mechanism in deprotonated state	–5	39	–23	202	–	–
Direct OH mechanism	–57	22	–6	79	–313	93
Direct OH mechanism in deprotonated state	–24	82	–10	49	–	–
Coordinated CH mechanism	–154	95	–	–	–	–
Coordinated OH mechanism	–150	103	–114	38	–192	115
Coordinated OH mechanism with bridging water	–	31	–30	(38)	(–192)	–
Aqueous phase						
Direct CH mechanism	–	< 50	–	0	–	–
Direct OH mechanism	–	84	≈ 0	–	–	–
Direct OH mechanism in deprotonated state	–	> 60	0	–	–	–
Coordinated OH mechanism	–	–	–	44	– 163	–

4.4. Car-Parrinello results

For the fully solvated systems in solution, first the stability of the reactant complexes for the direct mechanisms was studied. We equilibrated the solvent and the reactant complexes while constraining the distance between the methanol molecule and the ironoxo molecule, and followed this by unconstrained simulations to investigate whether the complexes are stable in solution. We did two simulation runs: one starting with the hydroxyl oxygen constrained at 2.92 Å from the oxo oxygen, and another starting with the carbon atom constrained at 2.96 Å from the oxo oxygen. Interestingly, we found that when the constraints are removed, the methanol molecule diffuses slowly away from the FeO^{2+} molecule, into the solution. This happens both when the methanol is interacting with FeO^{2+} via its OH group and when it interacts via its CH_3 group.

Apparently, the FeO^{2+}–methanol complex is not stable in solution, in spite of the very strong interaction in the gas phase. Of course, the FeO^{2+}–methanol bond now has to compete with an FeO^{2+}–water bond (minus the difference between hydrated methanol and hydrated water), and the entropy will favor the methanol going into the

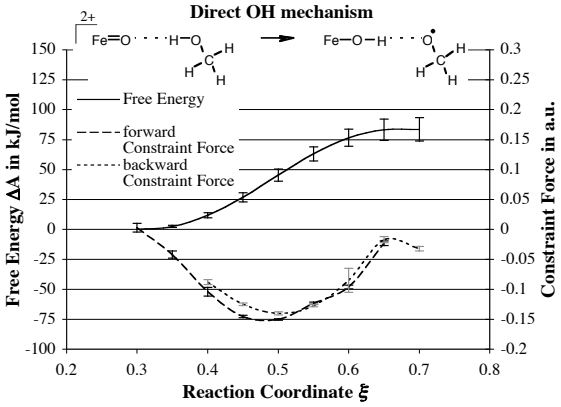

Figure 4.8 *Thermodynamic integration results for the first step of the direct OH mechanism. There is a small hysteresis effect that adds up to an error of about 10 kJ/mol. The barrier is estimated to be 84 kJ/mol and there is almost no barrier for the backward reaction, so the intermediate product is not stable.*

solution. Still, in view of the strong bond (70 kJ/mol) of the methyl group to ironoxo in the gas phase, one would expect this bond to prevail (the FeO^{2+}–water bond is "only" 43 kJ/mol in the microsolvated gas phase). It seems that the solvent effects cannot be understood simply in terms of the (gas phase) strengths of water–solute bonds that are formed and broken, but there must also be an electronic effect of the solvent, changing the strengths of these bonds compared to the gas phase. This fits in with the finding that the solvent diminishes the strong charge transfer bond to FeO^{2+} that is observed in the gas phase, as discussed more fully in Chapter 5.

We selected the following mechanisms and reaction steps for treatment by thermodynamic integration: the first step of the direct OH mechanism, the direct CH mechanism, and the second step of the coordination OH mechanism (see Figure 4.1).

The most interesting mechanism is the direct CH mechanism, as it has almost no barriers in the gas phase. The direct OH mechanism was also selected, even though the second barrier in that mechanism (79 kJ/mol in the gas phase) is relatively high. The series of simulations on the first step of the direct OH mechanism was used to obtain an estimate of the precision of the calculated barriers by quantifying the amount of hysteresis in our simulations.

Of the coordination mechanisms, the coordination CH mechanism was found in the gas phase calculations to be too unlikely to warrant further study. For the coordination OH mechanism, however, we observed that the first barrier could be lowered by a bridging water molecule. Analogously, a coordinated methanol molecule in solution can easily undergo hydrolysis, as would be expected in view of the natural acidity of methanol coordinated to the Fe^{IV} center. As a consequence, the facile hydrolysis of coordinated methanol, leading to transfer of the OH hydrogen to the oxo oxygen, leaves only the second step of the coordination OH mechanism, the transfer of a methyl

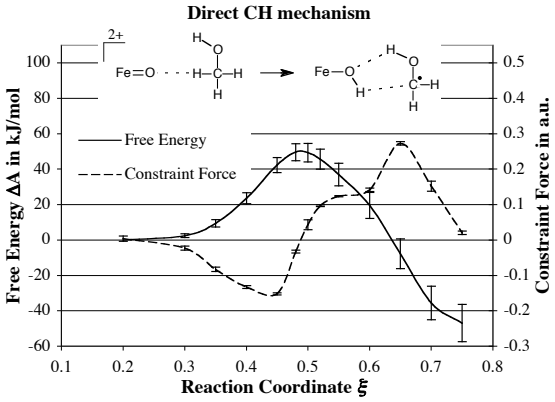

Figure 4.9 *Thermodynamic integration results for the direct CH mechanism. At ξ= 0.65, the second step of the reaction spontaneously occurs, and there is a large change in the constraint force. In the backward series, the second step is not reverting and the constraint forces remain very different. The free energy curve is based on the forward series and sampling over the equilibrium between both states would certainly lower this curve. The error bars in the free energy curve are based on the hysteresis in the direct OH mechanism and are only indicative.*

hydrogen, for thermodynamic integration. To model the starting point of this second step, we placed the H from the methanol OH group on the oxo oxygen, creating a (formally) $[Fe^{IV}(CH_3O^-)(OH^-)]^{2+}$ system.

4.4.1. The direct OH mechanism in solution

The results of the thermodynamic integration of (the first step of) the direct OH mechanism are shown in Figure 4.8. A Helmholtz free energy barrier of 84 kJ/mol is found, which is much higher than the 22 kJ/mol in the gas phase. Also, there is hardly any barrier for the reaction back to the reactants: When at ξ = 0.7 the constraint is switched off, the reaction goes back within a few picoseconds. Even with the constraint switched on, in some simulations the reaction went backwards, via a chain mechanism in which a hydrogen atom of a coordinated water molecule was abstracted by the $CH_3O^\bullet$ radical via a chain of solvent water molecules. As a consequence, the second step of this reaction cannot be simulated without constraining the products of the first step. However, from the height of the first barrier and the instability of the intermediate product, which is prone to react back to the reactants, it is already clear that the direct OH mechanism is very unlikely.

The direct OH H-abstraction reaction was used to estimate the hysteresis effects in our simulations. The statistical errors in the constraint forces are very small, but, despite the extensive equilibration, there is still some hysteresis present. Therefore, the free energy is calculated as the average of the forward and the backward series, and the standard error is estimated from the differences between the two curves. In this way the

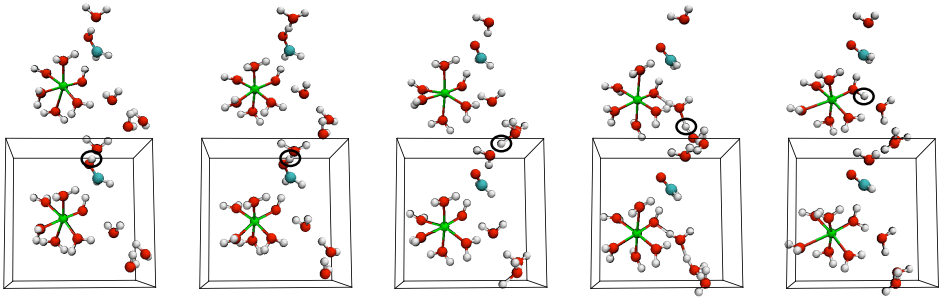

Figure 4.10 *Snapshots from the simulation at ξ = 0.65 in the direct CH mechanism. As visible in the snapshots a reaction coordinate ξ = 0.65 corresponds to almost complete transfer of the H to the oxo oxygen. In this simulation the OH hydrogen of methanol moves into the solution and travels via a chain mechanism to the iron complex. This second step occurs spontaneously already while the first step of the reaction has not finished yet. In the pictures the unit cell is shown plus one periodic image. The water molecules that are not taking part in the proton transfer and that are not coordinated to the iron are left out of the pictures. The hydrogen of interest has been circled.*

barrier is estimated to be 84 ± 10 kJ/mol. For the other mechanisms we performed only a forward integration, and the standard error is assumed to be the same.

4.4.2. The direct CH mechanism in solution

For the direct CH mechanism we have performed a thermodynamic integration along the reaction coordinate describing methyl H transfer to the oxo group, see Equation 4.3. The free energy profile, exhibiting a barrier of 50 ± 10 kJ/mol, and the force of constraint are shown in Figure 4.9. In the gas phase it was determined that a structure corresponding to the resulting intermediate radical $^{\bullet}CH_2OH$ complexed to the $FeOH^{2+}$ group could not be optimized, since transfer of the hydroxyl H to form $[Fe(H_2O)]^{2+}$ occurred spontaneously. We found something similar in the MD simulations of the process in solution. At ξ = 0.65, which is well beyond the transition state for C–H bond breaking, see Figure 4.9 (i.e. the transfer of the CH hydrogen to the FeO^{2+} is almost complete), the OH hydrogen leaves into the solution. It travels through the solvent via a chain mechanism (Figure 4.10) to end up on the former oxo oxygen (now the O of the OH ligand), resulting in $[Fe(H_2O)_6]^{2+}$ and formaldehyde. As a result of the occurrence of this "second step", the constraint force required to keep the CH hydrogen in the position dictated by the reaction coordinate value (ξ = 0.65) suddenly increases, because beyond this point a completely different situation is modeled.

The OH hydrogen (the “second step”) diffuses through the solvent by a Grotthuss diffusion mechanism (Figure 4.10) until it ends up at the oxo in a neighboring cell (as periodic image of the H that ends up at the oxo of the central unit cell, see last snapshot of Figure 4.10). In the periodic system used in these simulations, the diffusion path runs

to the OH ligand in the neighboring cell, but it could also have formed a loop to the OH ligand at its own Fe ion. In dilute solutions that would certainly be the case. This is actually very similar to the situation we have found in the O–O bond breaking of a coordinated H_2O_2 molecule, where an OH ligand is formed and the $OH^{\bullet}$ radical that is produced reacts through a H-bond wire either with a water ligand at the neighboring Fe or at the same Fe.[15,16] The statistics for these processes are an issue in these Car-Parrinello simulations with relatively small unit cells, a point that has been extensively investigated using the transition path sampling technique.[17]

It is interesting to consider in what nature the hydrogens are transferred: as proton, hydrogen atom, or hydride ion. The atomic charges and spin densities have been analyzed in the two different ways offered in the software package. The atomic charges are followed during the simulations using a built-in function of the PAW package that fits the charge density with Gaussian functions located at the atomic centers. A reasonable description of the atomic charges is obtained with 2 Gaussians per atom and a fitting cutoff of 5 Ry. The resulting charges should not be interpreted quantitatively, but they do provide a good opportunity to monitor changes in the electronic charge distribution in the system. Because the atomic charges are available for each MD step, the fluctuations in the charges can be analyzed as well.

For the atomic spin densities, the (delocalized) orbitals are expanded in spherical harmonics, and separated into up- and down-spin. The difference yields the local spin densities, recovering around 90% of the total spin.

The charge and spin density analyses do not lead to clear-cut, (almost) integer values for electron and spin densities on the transferring hydrogens, as was observed previously for the coordination OH mechanism in the gas phase. When the methanol binds to the ironoxo ($\xi = 0.3$) it obtains a small charge of $+0.139 \pm 0.008$ and a very small net spin of +0.005. During the transfer of the CH hydrogen a more significant (negative) spin *and* a positive charge start to accumulate on the CH_2OH moiety that is left behind. At $\xi = 0.65$ the CH_2OH has a charge of $+0.347 \pm 0.015$ and a net spin of –0.32. So there is a tendency to form a $^{\bullet}CH_2O$ radical, but there is, apparently, still considerable interaction with (charge transfer to) the $FeOH^{2+}$ group, leading to a net charge of +0.35. The build up of a full –1 spin is counteracted by reorganization of the "spectator" orbitals (not directly involved in the bond breaking process) and by the extent to which the charge transfer (from the $^{\bullet}CH_2O$ radical) consists more of β spin density than α spin density. When next the OH hydrogen leaves into the solution, the charge and the spin on the formed CH_2O drop again to $+0.09 \pm 0.02$ (charge) and –0.13 (spin), leaving a practically closed shell CH_2O moiety complexed to the FeOH (still at $\xi = 0.65$). Finally, the H_3O molecules that are formed during the H transfer through the solvent (Figure 4.10) have a net spin of 0.000 and a charge of $+0.36 \pm 0.08$ (for comparison: not reacting water molecules in this simulation have a charge of $+0.03 \pm 0.05$).

Although these results are not unequivocal, they justify in our view the interpretation that in the "first step", indeed, an $H^{\bullet}$ radical is transferred and a $^{\bullet}CH_2OH$ radical is formed. The interaction of the $^{\bullet}CH_2OH$ with FeOH apparently still involves

considerable charge transfer. Subsequently, the second H seems to transfer as an H^+. It should be kept in mind that in the solvent there will always be considerable charge flow into the 1s orbital of the H^+, as well as other charge rearrangements, compensating much of the formal +1 charge. As mentioned before, CPMD simulations of a proton in water solution yield a charge of +0.43 ± 0.02. Of course, when H^+ leaves, an (almost) neutral CH_2O is left behind, so an additional electron must be transferred from CH_2O to the Fe complex. The calculated charge and spin densities show that the charge rearrangements are rather subtle and we should beware of over simplistic interpretations.

In our simulations the "second step" of H dissociation from $^{\bullet}CH_2OH$ occurs spontaneously. This is reminiscent of situations where, owing to an improper choice of reaction coordinate, one first climbs too strongly uphill out of the reactants basin along the chosen reaction coordinate only to "escape" suddenly to the products basin along an orthogonal coordinate. Typically, a lower transition state could then be found if the intrinsic reaction coordinate were to be followed. It is not so clear whether this circumstance applies here. In theory, rather than pushing the system along the chosen reaction coordinate (i.e. transferring the methyl H to oxo) until the spontaneous transfer of the hydroxyl H occurs, a different reaction coordinate, which would start to deviate from the chosen reaction coordinate at a smaller value of the present ξ and entail transfer of the two H's in a concerted (or "nonsynchronous concerted"[137]) process, could lead to an overall lower reaction barrier. In particular this would be the case if the intrinsic reaction coordinate should deviate from the chosen one before the present transition state value of $\xi = 0.49$. However, we observe that the H dissociation now occurs well beyond the transition value of $\xi = 0.49$; $\xi = 0.65$ is well beyond the transition state, at a free energy which is already lower than that of the reactants. Therefore, even though we cannot rule out the possibility that a better choice of reaction coordinate would in fact yield a lower barrier, we do not consider this very likely. We are aware, though, that our barrier free energy of 50 kJ/mol should strictly be considered an upper bound.

The important conclusion remains that the direct CH mechanism is a very likely mechanism for the oxidation by FeO^{2+}.

The barrier that we have found is considerably higher than the 2 kJ/mol found in the microsolvated gas phase. This is an interesting solvent effect, which, as mentioned earlier, has an electronic origin: the dielectric screening effects of the solvent lead to a relative upshift of the one-electron levels of the 2+ charged Fe complex, most notably the LUMO, which is the major acceptor orbital for charge donation out of the C–H σ bonding orbital of the methyl group. In this way, the solvent weakens the charge transfer interaction between the C–H bond orbital and the FeO^{2+} LUMO, which is the main cause of the C–H bond weakening and breaking. This solvent effect is more fully investigated in Chapter 5.

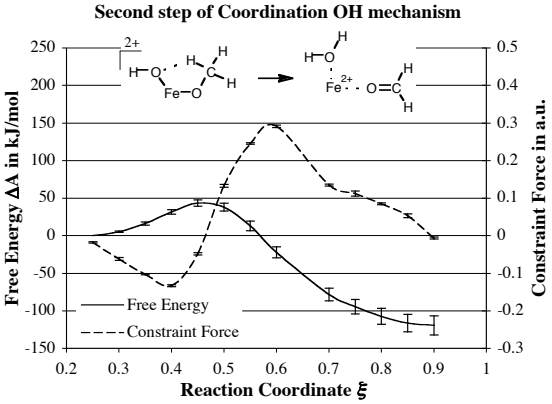

Figure 4.11 *Thermodynamic integration results for the second step of the coordination OH mechanism. The error bars in the free energy curve are based on the hysteresis in the direct OH mechanism and are only indicative.*

4.4.3. The coordination OH mechanism in solution

Finally, we consider the coordination OH mechanism in solution. Before, we tested the stability of the reactant complexes in solution for the direct mechanisms. However, coordination to the iron ion is much stronger than complexation to the oxo of FeO^{2+}. The (microsolvated) gas phase calculations show that water molecules are bound even stronger to the Fe^{IV} of FeO^{2+} than for instance to Fe^{2+} (117 kJ/mol to Fe^{IV} vs. 97 kJ/mol to Fe^{II}). It is therefore to be expected that there will be barriers to replace a coordinated water molecule by a methanol molecule and vice versa. Indeed, we find that the coordination of a methanol molecule to FeO^{2+} in solution is stable for the duration of our simulations (in total circa 70 ps).

More interesting, however, is the behavior of the OH hydrogen of the coordinated methanol molecule. The methanol becomes rather acidic, even more so than the coordinated water molecules. On the time scale of this type of simulation the probability of spontaneous deprotonation is very small, though. As an indirect indication of the acidity of coordinated methanol we can consider the observed lengthening of the O–H bond: For a free methanol molecule in solution the length of the O–H bond during an MD run is 0.99 ± 0.03 Å, and for coordinated methanol it is 1.03 ± 0.05 Å. For the already quite acidic coordinated water molecule (the pK_a of $[FeO(H_2O)_5]^{2+}$(aq) has been estimated to be 2) the values for solvated and coordinated water molecules are 0.99 ± 0.03 Å and 1.01 ± 0.03 Å, respectively. The stronger O–H bond lengthening of the coordinated methanol indicates that it is more acidic. Accordingly, the H atom abstraction of the first reaction step (Figure 4.1c) can be circumvented in solution by proton transfer through the solvent. As a matter of fact, we have found in the gas phase that with one intermediate water molecule the H that was transferred along this short chain could not be identified as pure $H^{\bullet}$ or H^+ in a straightforward manner. In any case, the end result is formally a $[Fe^{IV}OH]^{3+}$ with a coordinated CH_3O^-, i.e. $[Fe^{IV}(CH_3O^-)(OH^-)]^{2+}$. We assume that this H transfer is so

facile that it is not a rate-limiting step. The probability of the alternative, the proton staying in the water solution, depends on the concentration of the system; in our small simulation cell this situation has a very low probability as it would lead to an H^+ concentration of 2 M, giving a pH of –0.3!

So for the thermodynamic integration of the second step of the reaction, the transfer of a methyl hydrogen, we have assumed that H transfer from the hydroxyl group to the oxo oxygen takes place.

The results of the thermodynamic integration of the second reaction step are shown in Figure 4.11. We find a free energy barrier of 44 ± 10 kJ/mol. The height and the position of this barrier in solution are very similar to the energy barrier of 38 kJ/mol in the gas phase. It is interesting that here we have an example in which solvent effects do not change the barrier significantly.

With a barrier of 44 kJ/mol, which is comparable to the 50 kJ/mol of the direct CH mechanism, the coordination OH mechanism seems to have a reasonable probability of occurring. However, the methanol molecule first needs to substitute a water ligand and coordinate to the iron ion, and then its H needs to be transferred via the solvent towards the oxo oxygen, before the second step can take place. Since the competitive direct CH mechanism does not depend on a prior ligand substitution the barrier for ligand substitution may be an important factor in the preference of one reaction path over the other. Although the coordination OH mechanism cannot be ruled out, since ligand substitution can be fast in spite of strong metal–ligand bonds, we expect that the direct CH mechanism will be the most important one for the oxidation by FeO^{2+}.

4.5. Reactions with deprotonated $[FeO(H_2O)_5]^{2+}$

As mentioned before, $[FeO(H_2O)_5]^{2+}$ is rather acidic; the pK_a is experimentally unknown but has been estimated at ca. 2.[125] This means that under the usual conditions of the Fenton reaction (optimal pH: 3-5[2,109]) it might be deprotonated. Therefore, we should not only study $[FeO(H_2O)_5]^{2+}$, but also its conjugate base: $[FeO(H_2O)_4OH]^+$. We have thus performed further calculations in the gas phase and in solution. We discuss the direct OH, the direct CH, and the coordination OH mechanism in the gas phase, and the direct OH mechanism in solution.

The complexes have several non-equivalent protons, but because deprotonation has a clear deactivating effect as result of the change in net charge, as shown below, we restricted ourselves to demonstrating the effect for removal of a proton from an equatorial water molecule. For the deprotonated version of the second step of the coordination OH mechanism we removed the proton from the OH^- ligand, which it had formed with the oxo oxygen in the first step. This is equivalent to the assumption that the coordinated methanol is more acidic than the coordinated water molecules, and the deprotonated species to be considered is therefore the one in which the hydroxyl H of methanol has been removed (as H^+), leaving only the second step of this mechanism (transfer of a methyl H to the oxo group) to be investigated.

Table 4.2 *Interaction energies in kJ/mol of $[FeO(H_2O)_5]^{2+}$ with water and methanol, compared to the interaction energies of its conjugate base complexes.*

	$FeO–H_2O$	$FeO–HOCH_3$	$FeO–H_3COH$
$[Fe^{IV}O(H_2O)_5]^{2+}$	43 (OO-bond)	57	70
$[Fe^{IV}O(H_2O)_4OH]^{+}$	21 (H-bond)	24	5

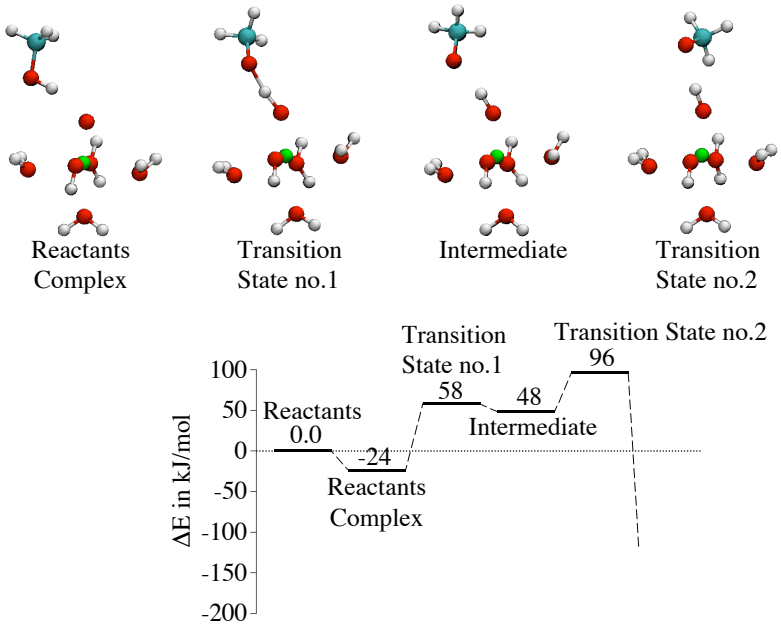

Figure 4.12 *Microsolvated gas phase results for the direct OH mechanism in the deprotonated state. One of the protons of an equatorial water molecule has been removed.*

In the simulations in solution the same (equatorial) proton was removed as in the gas phase. During these simulations no proton exchange between first-shell water molecules was observed.

4.5.1. Gas phase

Going from $[FeO(H_2O)_5]^{2+}$ to $[FeO(H_2O)_4OH]^{+}$, the orbitals shift upwards in energy, and the LUMO is not that extremely low-lying anymore. As a result, the charge transfer interaction with a substrate (methanol or water) is strongly diminished. In fact, the reactants can now form hydrogen bonds, with the oxo oxygen acting as electron donor (H-bond acceptor) by way of the half filled $2\pi^*$ orbitals. The interaction energies drop to 21 kJ/mol for water (now hydrogen bonded), 24 kJ/mol for methanol via the OH group (much closer to typical H-bond strengths), and a mere 5 kJ/mol when

methanol interacts via its CH_3 group, which of course is a very poor H-bond donor (Table 4.2).

In Figure 4.12 the gas phase results are given for the direct OH mechanism with deprotonated FeO^{2+}. As shown in Table 4.2, the complexation at $[FeO(H_2O)_4OH]^+$ is much weaker, caused by the fact that the charge transfer interaction is replaced by a classical hydrogen bond interaction. As a result, the barrier for the abstraction of the OH hydrogen also increases. This barrier becomes rather high (82 kJ/mol at reaction coordinate ξ = 0.55, compared to 22 kJ/mol before), and the second barrier is also considerable, making the reaction less favorable when the ironoxo complex is in a deprotonated state.

For the direct CH mechanism –the most probable mechanism when FeO^{2+} is not deprotonated– the change is even more dramatic (not depicted): In this case, the energy of complexation is reduced from 70 to 5 kJ/mol, and the barrier of the methyl H-abstraction increases from 2 kJ/mol to 39 kJ/mol. The second barrier, the abstraction of the hydroxyl hydrogen, even changes from 0 kJ/mol to 202 kJ/mol, so the direct CH mechanism is completely inhibited when a water molecule in the first shell of the iron ion is deprotonated.

For the coordination OH mechanism deprotonation of the complex is also disadvantageous for the reaction. As mentioned above, the deprotonated species we consider is the one in which the coordinated methanol has lost a proton. In this case the second step of the reaction consists of transfer of a methyl H to the oxo oxygen. We calculated a barrier of 87 kJ/mol for this second step (vs. 38 kJ/mol before).

Apparently, for all mechanisms, a *relatively* high pH (relative to pK_a = 2), at which deprotonated states start to become abundant, is disadvantageous for the reaction. This fits in with the fact that the Fenton reaction is optimally performed in acidic solution, pH = 3-5. Too high pH would of course be problematic anyway, since ironhydroxide complexes are not soluble in basic solutions.

4.5.2. Solution

For completeness, we also performed one series of Car-Parrinello simulations in solution with the deprotonated reactant (the conjugate base) $[FeO(H_2O)_4OH]^+$. These simulations were performed for the direct OH mechanism. In this case, the reactants complex was stable during a test simulation of 15 ps, in contrast to what we found before for the complexation to $[FeO(H_2O)_5]^{2+}$. With the conjugate base, a stable hydrogen bond is formed with the oxo oxygen as H-bond acceptor (electron donor), which is, apparently, much less influenced by the solvent than the charge transfer interaction in the normal case.

The results of the thermodynamic integration are shown in Figure 4.13. The intermediate product turns out to be even more unstable in the deprotonated state than it was in the protonated state. As a consequence in all simulations beyond ξ = 0.6 the molecules react back to the reactants via a chain mechanism. In these simulations, a hydrogen atom of one of the ligands (either a water ligand or an OH^- ligand) is

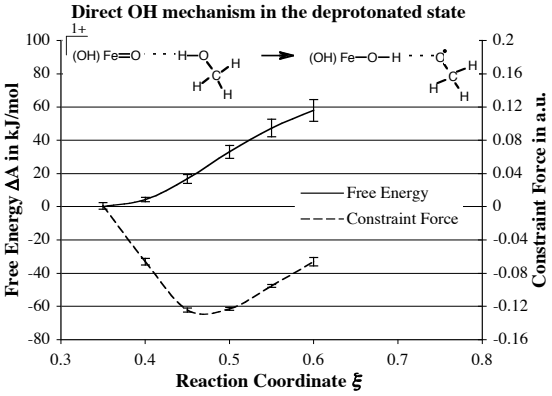

Figure 4.13 *Thermodynamic integration results for the first step of the direct OH mechanism in the deprotonated state. The intermediate product is very unstable and makes it impossible to complete the series. The error bars in the free energy curve are based on the hysteresis in the ordinary protonated state and are only indicative.*

transferred to the $CH_3O^{\bullet}$ radical via solvent water molecules, resulting in reformation of the reactants. The simulations beyond $\xi = 0.6$ could thus not be performed and the series could not be completed. Nevertheless, the trend is clear: in a relatively basic solution FeO^{2+} is even less likely to abstract the OH hydrogen for the direct OH mechanism than in an acidic solution.

In conclusion, we find that deprotonation weakens the reactivity of $[FeO(H_2O)_5]^{2+}$ for the direct CH and OH mechanisms, and also for the coordination OH mechanism. Especially for the direct mechanisms the effect of deprotonation has a similar electronic origin as the effect of solvation. Deprotonation changes the overall charge from +2 to +1. This causes a relative upshift of the LUMO, which strongly diminishes the peculiarly strong charge transfer interaction of the very low-lying FeO^{2+} LUMO with the organic substrate. Long-range dielectric screening effects of the solvent have the same effect: the charge transfer interaction is weakened because the LUMO of FeO^{2+} is shifted upwards more than the orbital levels of the neutral organic substrate. The effect of deprotonation is less striking in solution, because, once the charge transfer interaction is weakened, another upshift of the LUMO has much less effect.

4.6. Conclusion

We have studied the mechanism of the oxidation of methanol by FeO^{2+} in water, as a prototype for alcohol oxidation in the Fenton chemistry. We find the direct CH mechanism to have the highest probability. In this mechanism, the methanol molecule first forms a complex bond with the oxo group with a methyl C–H bond in an approximately linear configuration to the Fe–O bond. The C–H bond is then attacked as the first step. In the gas phase this mechanism has a spectacularly low barrier of only 2

kJ/mol (and the second step, the transfer of the OH hydrogen, even occurs without barrier). In solution the Helmholtz free energy barrier has been estimated to have an upper bound of 50 kJ/mol; the second step still occurs spontaneously. The first step of methanol oxidation via the direct CH mechanism is similar to the one in methane oxidation, where in this case an OH ligand and a weakly bound $^{\bullet}CH_2OH$ radical are formed, but the second step is not the "rebound mechanism" of OH binding to the $^{\bullet}CH_2OH$ radical, to form a di-alcohol. Instead, the H of the hydroxyl group of methanol is transferred without barrier to the OH ligand to form an H_2O ligand. This H transfer occurs through the solvent via a Grotthuss diffusion mechanism.

The high reactivity of the ironoxo complex towards aliphatic bonds like the methanol C–H bonds can be explained by the very low-lying up-spin LUMO of FeO^{2+}, which is the Fe–O $3\sigma^*$ orbital. This orbital reaches spatially beyond the occupied orbitals and makes the ironoxo ion very open to reaction at the oxo site. As a result, FeO^{2+} is a very strong electron acceptor, rather than being a hydrogen bond acceptor (in which case it would have to act as electron donor): a molecule that comes close enough to form a hydrogen bond starts to interact with the LUMO, and forms a strong charge transfer bond instead. The charge transfer from the C–H bonding orbital into the $3\sigma^*$ activates the C–H bond. The charge transfer increases when the C–H bond is stretched, which compensates for the strain energy and lowers the barrier even more, enabling easy abstraction of a hydrogen atom.

We have observed that the solvent effects on the barriers of the direct mechanisms are very large (50 kJ/mol in water solvent vs. 2 kJ/mol in the gas phase for the direct CH mechanism). A similar large increase in the barrier was observed in the methane to methanol oxidation by aqueous FeO^{2+} (from 14 kJ/mol to 92 kJ/mol).[106] We stress that this is not a display of a systematic problem in the microsolvated gas phase calculations, but it is caused by a very specific solvation effect. When the system is brought into solution, the orbitals of the positively charged FeO^{2+} shift upwards relative to those of the neutral methanol due to the screening of the solvent, and, as a result, the charge transfer interaction with the low-lying $3\sigma^*$ LUMO weakens. In turn, the activation of the methanol bonds is less pronounced and the reaction barriers increase.

Among the other mechanisms of Figure 4.1, we have been able to rule out the direct OH mechanism and the coordination CH mechanism. However, the coordination OH mechanism cannot be ruled out. Although the gas phase barrier for hydrogen transfer from the OH group of coordinated methanol to the oxo oxygen is over 100 kJ/mol, the introduction of a bridging water molecule lowers the gas phase barrier to 31 kJ/mol. The second step of H abstraction from the CH_3 group has a barrier of 38 kJ/mol.

In solution the easy hydrolysis of the coordinated methanol plays a role. Because of the high acidity of the Fe^{IV} complexes, we envisage easy transfer of the hydroxyl H to the FeO^{2+}, possibly along a chain of water molecules. The Helmholtz free energy barrier of the second step becomes 44 ± 10 kJ/mol and is close to the energy barrier of 38 kJ/mol in the gas phase. This barrier makes the coordination OH mechanism competitive with the direct CH mechanism with its free energy barrier of 50 kJ/mol

(upper bound). However, it should be kept in mind, that the coordination OH mechanism can only become operative after a water/methanol ligand substitution.

Because $[FeO(H_2O)_5]^{2+}$ is rather acidic (pK_a = 2), it could very well be deprotonated, and therefore we also studied the reactivity of its conjugate base: $[FeO(H_2O)_4OH]^{+}$. However, for all the mechanisms of Figure 4.1, the reaction barriers become higher upon deprotonation. Clearly, the conjugate base of $[FeO(H_2O)_5]^{2+}$ is much less reactive, and relatively basic conditions will slow down the reaction. This relates well to the fact that a low pH is needed for the Fenton reaction (optimal pH = 3-5). Of course, too high pH would hamper the reaction anyway due to precipitation of iron hydroxides.

The decreased reactivity of the conjugate base of $[FeO(H_2O)_5]^{2+}$, especially for the direct mechanisms, has the same cause as the increase of the barriers in solution compared to the gas phase: the deprotonation makes the orbitals shift upwards in energy and, as a result, the reactivity decreases. Finally, this also explains why in the deprotonated case the solvent effect is much smaller: The screening effects are smaller due to the smaller charge (+1 instead of +2), and the $3\sigma^*$ orbital is already shifted upwards due to the lowering of the positive charge, diminishing the charge transfer interaction.

5.

Properties of FeO^{2+}: electronic structure and solvation effects*

Abstract:

An electronic structure analysis has been performed of the action of solvated FeO^{2+}, $[FeO(H_2O)_5]^{2+}$ as a hydroxylation catalyst. It was found that the oxo end of FeO^{2+} does not form hydrogen bonds (as electron donor and H-bond acceptor) with H-bond donors nor with aliphatic C–H bonds, but it activates C–H bonds as an electron acceptor. It is extremely electrophilic, to the extent that it can activate even such poor electron donors as aliphatic C–H bonds, the C–H bond orbital acting as electron donor in a charge transfer type of interaction. Lower lying O–H bonding orbitals are less easily activated by FeO^{2+}.

The primary electron accepting orbital of FeO^{2+} in a water environment is the $3\sigma^{*\uparrow}$ orbital, an antibonding combination of Fe-$3d_{z^2}$ and O-$2p_z$, which is very low-lying relative to the $2\pi^{*\uparrow}$, compared with, for example, the σ^* orbital in O_2 relative to its π^*. This is ascribed to relatively small Fe-$3d_{z^2}$ with O-$2p_z$ overlap, due to the nodal structure of the $3d_{z^2}$.

The hydrogen abstraction barrier is very low in the gas phase, but it is considerably enhanced in water solvent. This is shown to be due to strong screening effects of the dielectric medium, leading to relative destabilization of the levels of the charged $[FeO(H_2O)_5]^{2+}$ species compared to those of the neutral substrate molecules, making it a less effective electron acceptor. The solvent directly affects the orbital interactions responsible for the catalytic reaction.

* This chapter is based on: M.J. Louwerse and E.J. Baerends, *Phys. Chem. Chem. Phys.* **9** (2007) 156-166.

5.1. Introduction

The oxoiron(IV) ion, FeO^{2+}, has long been known to be the active center in heme iron enzymes such as cytochrome P450.[95,99] Its activity is generally ascribed to the hydrogen abstraction/oxygen rebound mechanism proposed about 30 years ago by Groves and co-workers.[107,108] There is also evidence for some non-heme iron enzymes,[98,101] including bleomycin,[138] and iron containing zeolites like FeZSM-5,[139] that the active intermediates are iron-oxo species. Nonetheless, in particular in the classical Fenton reaction[1] (oxidation by H_2O_2 catalyzed by ferrous ions in aqueous solution), the presence and role of ferryl ion has been the subject of long debate.[5,6,9,10] DFT calculations have indicated that in Fenton chemistry the production of an FeO^{2+} intermediate seems to be thermodynamically favorable over production of $OH^{\bullet}$ radicals,[14] which was later substantiated by Car-Parrinello molecular dynamics simulations in water solution.[15-17] On the other hand, the occurrence of FeO^{2+} in Fenton chemistry has very recently been thrown into doubt.[41] The issue appears far from settled.[9]

Significantly, the presence of the FeO^{2+} moiety has been experimentally established over the past years in a number of non-heme enzymes and complexes. Que and co-workers have characterized and studied the catalytic activity of FeO^{2+} with tetradentate and pentadentate nitrogen lone pair ligands[103,105] (see also Feringa et al.[104]). Very recently the pentaaquaferryl ion was unequivocally characterized experimentally,[41] and its activity as an oxygen atom transfer reagent demonstrated. The electronic structure of the bare FeO^{2+} (and FeO^{+}) have been the subject of several investigations,[113-115,140] some in connection with gas phase studies of reactivity.[110,111,113-115] Many discussions of the electronic structure of non-heme complexes of FeO^{2+} have appeared in recent years.[117-124]

The purpose of the present chapter is twofold. First, we will give a detailed electronic structure explanation of the remarkable capability of the ferryl ion to hydroxylate even the strong aliphatic C–H bonds, in terms of the nature and energies of the participating molecular orbitals (MOs). Secondly, we will address the issue of the much higher barrier to reaction that has been found in aqueous solution for reaction of FeO^{2+} with methane[106] and methanol (Chapter 4), compared to the reaction of the microsolvated complex ($[FeO(H_2O)_5]^{2+}$) in the gas phase.

To set the stage, we display in Table 5.1 a sample of the interaction energies and reaction barriers obtained for simple substrate molecules like methane,[106] methanol (Chapter 4), and hydrogen peroxide[117] and for the interaction with water, calculated in the gas phase and in solution. The reaction barriers are for hydrogen abstraction, the first step in the rebound mechanism for hydroxylation. In Figure 5.1 some of the reactant complexes are depicted. In Figure 5.2 the precise bonding distances and angles are given.

Table 5.1 *Interaction energies and hydrogen abstraction barriers for molecules interacting with $[FeO(H_2O)_5]^{2+}$ in the gas phase and in solution. The height of the barriers is measured with respect to the reactant complexes. The label "CH_3OH" denotes a methanol molecule that is interacting via its CH_3 group (Figure 5.1b) and "$HOCH_3$" is a methanol molecule interacting via its OH group (Figure 5.1c). Energies are given in kJ/mol. The free energies in water solution have an estimated error bar of 10 kJ/mol.*

	CH_4	CH_3OH	$HOCH_3$	H_2O	H_2O_2
Gas phase:					
Interaction energy	–9	–70	–57	–43	–81
H-abstraction barrier	23	2	22	–	7
Water solution:					
Free energy barrier	95	47	84	–	–

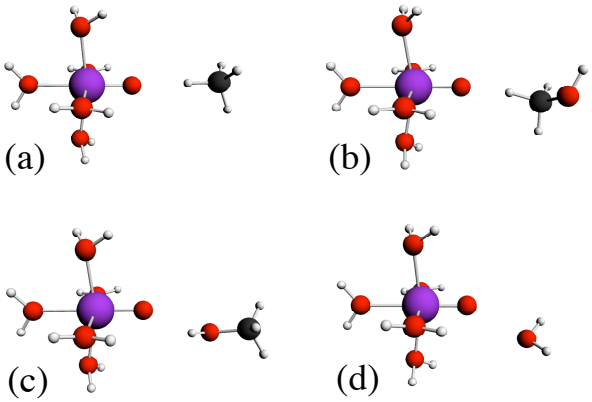

Figure 5.1 *Pictures of the complexes under study. (a) Methane interacts with $[FeO(H_2O)_5]^{2+}$ in a linear configuration. (b,c) Methanol can interact with $[FeO(H_2O)_5]^{2+}$ either via its methyl group (b) or via its hydroxyl group (c), in both cases leading to a very strong interaction. (d) In the gas phase water rotates its oxygen atom towards the oxo oxygen of FeO^{2+} to make an O–O interaction.*

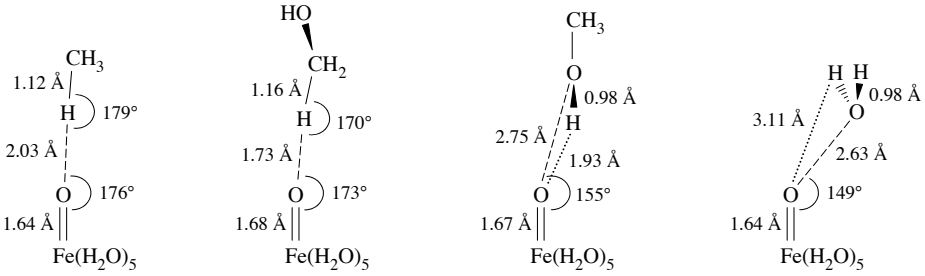

Figure 5.2 *Distances and angles in the optimized complexes of $[FeO(H_2O)_5]^{2+}$ with methane, methanol, and water, respectively.*

Table 5.1 contains results that demand an explanation. In the first place, except for methane, the interactions with FeO^{2+} are rather strong: the interactions of water, methanol, and hydrogen peroxide vary from 43 to 81 kJ/mol, which is 2 to 4 times the strength of an average hydrogen bond. Remarkably, although methanol interacts rather strongly via its methyl group with the FeO^{2+} ion, the interaction of methane is much weaker.

Methanol may also bind with its hydroxyl group to FeO^{2+}, in which case the bonding is 13 kJ/mol weaker than for bonding with the methyl group. However, the interaction is not by hydrogen bond donation to the oxo ligand of the $[FeO(H_2O)_5]^{2+}$ complex, and neither is that the case for bonding of water. This can be recognized in the orientation of the molecules: the interaction is primarily with the lone pairs on the oxygen atoms of water and methanol.

A very salient feature of Table 5.1 is the strong increase of the transition state barrier for the hydrogen abstraction in water solution compared to the extremely small barriers in the gas phase. These barriers in solution have been obtained from Car-Parrinello molecular dynamics, using the technique of thermodynamic integration along the reaction path. They therefore represent free energy barriers.

We will rationalize these findings with the help of electronic structure considerations. In their seminal work, Schröder, Schwarz, Shaik, and co-workers have explained the electronic structure and the reactivity of the related FeO^{+} ion in the gas phase.[113-115] They have stressed the analogy of the electronic structure and the reactivity of FeO^{+} to that of the O_2 molecule: it is a bi-π-radical, and in the optimal reaction path spin-crossings occur leading to a two-state-reactivity (TSR) mechanism.

However, for FeO^{2+} we will identify as the particular electronic structure feature that lends it its special role in oxygenation catalysis, the availability of an extremely low-lying empty acceptor orbital, the $3\sigma^*$ orbital, an antibonding combination of the Fe-$3d_{z^2}$ and the O-$2p_z$. In fact, this low-lying σ^* LUMO makes FeO^{2+} more analogous to the F_2 molecule than to O_2, F_2 also being highly reactive owing to a low-lying σ^* acceptor orbital. FeO^{2+} is extremely electrophilic indeed. It activates C–H bonds by acting as an electron acceptor to the C–H σ bonding orbital, even though this orbital is low-lying and in principle a very poor donor orbital. The activation does not at all involve donation of electrons into the C–H σ^* orbital; in fact, such donation does not even proceed into the O–H σ^* orbital, which is the reason the oxo oxygen does not participate in hydrogen bonding (as H-bond acceptor).

The large solvent effect on the barrier height cannot be understood simply from different solvation stabilization of reactants and transition state. We will show that it is caused by modification of the electronic structure mechanism of the reaction by the solvent environment. The relevant orbital levels of $[FeO(H_2O)_5]^{2+}$ and of the substrate molecules undergo differential shifts in solution, which modifies interaction strengths and reaction barriers. This is another example of the important role the solvent may play in modifying orbital interaction patterns, as also recently observed in a calculation of p*K*a's in water.[141]

5.2. Methods

All calculations have been performed with the ADF (Amsterdam Density Functional) package[60-63] using the BLYP[65,66] density functional. All electrons are included in the calculations and large STO basis sets are used, which are available in the ADF library of standard basis sets,[60] namely the QZ4P set (a quadruple-ζ basis set with four sets of polarization functions) for iron and the TZ2P set (a triple-ζ basis sets with two sets of polarization functions) for the other atoms. Additionally, the calculations were corrected for relativistic effects using the Zero-Order Regular Approximation (ZORA)[64] approach.

First, the calculations were performed in the gas phase with the first coordination shell of water molecules around the iron ion included in the calculations, resulting in $[FeO(H_2O)_5]^{2+}$. Secondly, for the calculations in solution the same penta-aqua oxo complexes were used, and the solvent was modeled as a dielectricum, using the Conductor-like Screening Model (COSMO)[142,143] as implemented[144] in ADF. As parameters for the COSMO model the following radii were used: 1.6 Å for Fe^{2+}, 1.7784 Å for O, 1.3 Å for H, and 1.4 Å for the solvent molecules. The dielectric constant used was 78.4. We have verified that this model for the solvent yields the same effects as found in Ref. 106 and Chapter 4, where explicit solvent water molecules have been included which were treated fully quantum mechanically. The COSMO model is used to demonstrate that the observed solvent effects can be attributed to long-range dielectric screening effects.

We analyze the bonding of this $[FeO(H_2O)_5]^{2+}$ complex with water, methane, and methanol, respectively, using the fragment orbital analysis as it is implemented in the ADF package.[145] For each complex the geometry is first optimized, and in this optimized geometry each complex is divided into two fragments: the $[FeO(H_2O)_5]^{2+}$ complex and the H_2O, CH_4, or CH_3OH molecule. For these fragments the molecular orbitals are calculated, and then the total electronic structure is recalculated based on the fragment orbitals. In this way the contributions of the fragment orbitals to the complex molecular orbitals are found. Also, the interaction energy can be decomposed[145-147] into Pauli repulsion, electrostatic interaction, and orbital interactions between the fragments plus the energy cost to deform the fragments from their optimized geometries in the isolated fragment to the geometry they obtain in the complex.

The fragment orbital analysis can only be performed with one set of orbitals on each fragment, i.e. the ones obtained in spin-restricted calculations on the fragments. It cannot use simultaneously two sets of orbitals, such as the $\uparrow$ and $\downarrow$ spinorbitals obtained in spin-unrestricted calculations. Therefore for the $[FeO(H_2O)_5]^{2+}$ fragment the spin-restricted orbitals were determined. The proper $S = 2$ ground state was then prepared by assigning the correct spin-unrestricted electron occupations (excess $\uparrow$ spin electrons, see next section). This ground state, however, lacks the energy lowering ("spin polarization") from further self-consistent optimization of the spinorbitals. This leads to a systematic overestimation of the interaction energy by an amount of 28-29 kJ/mol (depending on the exact fragment geometry). We corrected the orbital

interaction term for this overestimation, so that this energy term and the total bond energy properly reflect the energy with respect to the spin polarized $[FeO(H_2O)_5]^{2+}$ complex. All reported values in this chapter for orbital interactions and total interactions have been corrected in this manner.

The energy levels of the substrate molecules are strongly influenced by the net charge of the ironoxo complex and shift down considerably when these molecules approach the charged complex. Even though orbital interaction diagrams are only qualitative, the orbital levels should convey an intuitive grasp of the orbital mixings, and therefore the abovementioned shift should at least qualitatively be taken into account. So in the orbital schemes in Figure 5.7, Figure 5.9, and A1-A4 (Appendix A) the water, methane, and methanol orbitals are all shifted (in each case all levels by the same constant) from the isolated molecule values. The constant is determined as the average shift of the non-interacting orbitals of a substrate molecule as calculated in the complex. Note that the shift can differ for different molecules, presumably because the bonding distances are different.

When such a shifted HOMO starts to mix with the FeO^{2+} LUMO, the relative levels of these two orbitals changes somewhat more, because of the charge transfer that occurs. Therefore, the abovementioned shift, as depicted in the figures and given in the tables, is only qualitative. In the final self-consistent field, the substrate HOMO will be slightly lower in energy and the FeO^{2+} LUMO slightly higher.

5.3. Results: transition state barriers for hydrogen abstraction in the gas phase

5.3.1. Electronic structure of gas phase FeO^{2+} and $[FeO(H_2O)_5]^{2+}$

First we will discuss the FeO^{2+} species itself. In Figure 5.3a a schematic orbital diagram is shown for the FeO^{2+} species in the gas phase. A detailed description of the composition of these orbitals can be found in Table 1 of Ref. 117. The 1σ orbital is not involved in the bonding, it is practically 100% O-2s. The iron and the oxygen atoms form bonding and antibonding orbitals of σ symmetry, 2σ ($d_{z^2} + p_z$) and $3\sigma*$ ($d_{z^2} - p_z$) and of π symmetry, 1π ($d_{xz,yz} + p_{x,y}$) and $2\pi^*$ ($d_{xz,yz} - p_{x,y}$), where we take the Fe–O bond as the z axis. Although in transition metal complexes the antibonding combinations are commonly denoted as the (formally) “d orbitals”, we note that in this case the orbitals are actually strong mixtures, indicating almost covalent bonds.[117] In fact, the bonding combinations 2σ and 1π are the ones with the larger d contributions (53% d_{z^2} and 67% $d_{xz,yz}$, respectively). The d_δ orbitals ($d_{x^2-y^2}$ and d_{xy}), on the other hand, are purely nonbonding.

The 2σ and 1π are doubly occupied, with both spin ↑ and spin ↓ electrons, but the $2\pi^*$ is only occupied with spin ↑ electrons, as in O_2. Since the d_δ orbitals are also only occupied with ↑ electrons, there are four unpaired ↑ spin electrons, i.e. $S = 2$. The surplus of ↑ electrons causes a strong stabilizing field due to the exchange interaction, so all ↑ levels are considerably lower than the corresponding ↓ levels.

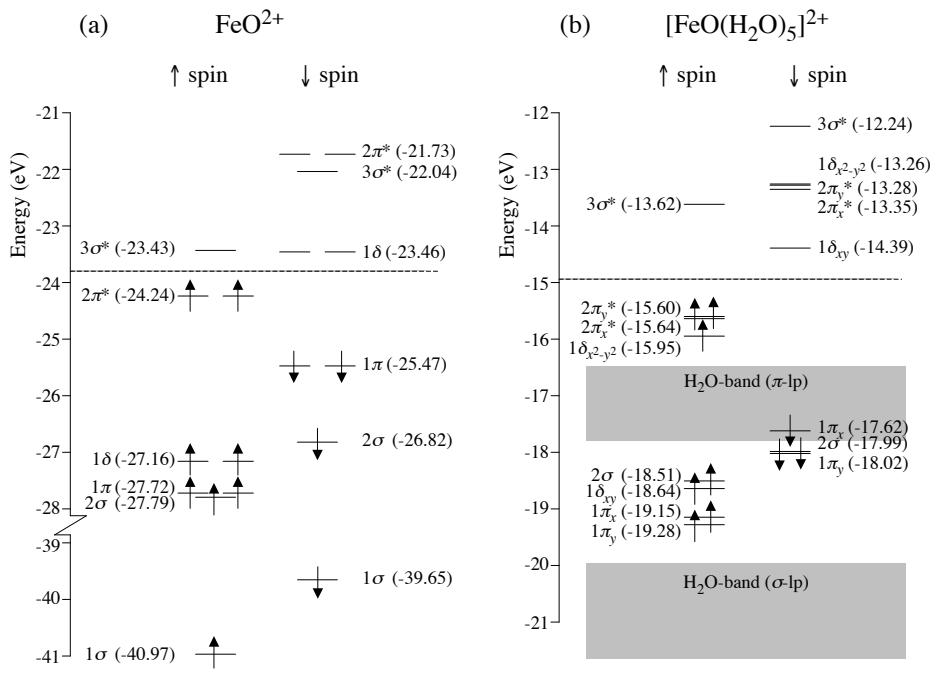

Figure 5.3 *Orbital level diagram for bare FeO^{2+} and for the FeO orbitals in $[FeO(H_2O)_5]^{2+}$. Both molecules are in the S = 2 ground state. Because of the high spin state, there is a large energy difference between ↑ and ↓ spin orbitals. In both cases the lowest empty orbital that is involved in Fe–O bonding is the $3\sigma^{*\uparrow}$ orbital.*

The $3\sigma^{*\uparrow}$ is the lowest unoccupied orbital and the important frontier orbital of this moiety. The empty ↓ spin d_δ orbitals are actually at practically the same energy, but will not play a role since they are not involved in the Fe–O bonding, and will be shielded from an incoming substrate molecule by the equatorial ligands. The $2\pi^{*\downarrow}$ orbitals and the $3\sigma^{*\downarrow}$ are also low-lying empty orbitals (the important orbitals for the case of FeO^+), but these orbitals are less important as acceptor orbitals than the $3\sigma^{*\uparrow}$, since they are roughly 1 eV higher in energy. The $3\sigma^{*\uparrow}$ orbital has considerable amplitude at the oxo end (it has 48% O-$2p_z$ character, *versus* 37% Fe-d_{z^2}). Its particularly low energy and the large amplitude at the oxo group cause it to act as an electron acceptor in strong charge transfer interactions, even with relatively low-lying donor orbitals such as the C–H bonding orbital. As we will see below, this gives FeO^{2+} its unique capability to activate such bonds.

Due to its occupation pattern ($1\pi^4 2\pi^2$) and TSR mechanism, FeO^+ has been compared to O_2.[113-115] Because for FeO^{2+} there is no TSR mechanism, but instead the reactivity is driven by the very low-lying empty σ^* orbital, FeO^{2+} is more analogous to the F_2 molecule.

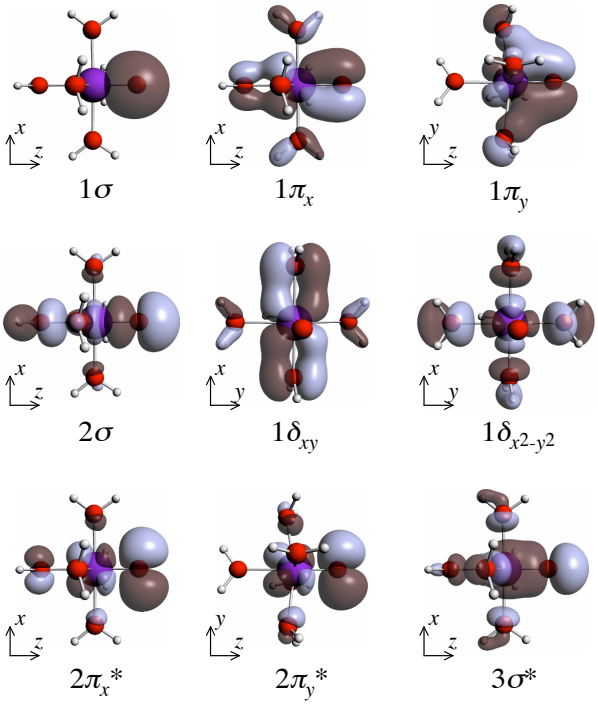

Figure 5.4 *Pictures of the FeO orbitals in the $[FeO(H_2O)_5]^{2+}$ complex. Depicted are the ↑ orbitals; for the ↓ orbitals the mixing with the water orbitals is somewhat different. The plane of drawing is the xz plane (Fe–O is along the z axis). For the $1\delta_{xy}$ and $1\delta_{x^2-y^2}$ orbitals the plane of drawing is the equatorial (xy) plane and for $1\pi_y$ and $2\pi_y^*$ it is the yz plane.*

Of course, the interaction with a substrate molecule will be modified when the FeO^{2+} is surrounded by ligands. In Figure 5.3b we give the level scheme for $[FeO(H_2O)_5]^{2+}$, and in Figure 5.4 the orbitals are depicted. A complete description of all molecular orbitals in this complex can be found in Table 2 of Ref. 117. In the level scheme, two blocks with H_2O lone pair levels are indicated, in between the FeO^{2+}-derived levels: the $\sigma(2a_1)$ lone pairs and the $\pi(1b_2)$ lone pairs.

The main change in the oxoiron(IV) levels with respect to the bare FeO^{2+} is for the d_δ levels. The $d_{x^2-y^2}$, with lobes along the axes, is pushed up by antibonding interaction with the σ lone pairs of the equatorial H_2Os, cf. the antibonding character displayed in Figure 5.4 for the $d_{x^2-y^2}$. As already highlighted in Ref. 117, the higher lying π lone pairs of the equatorial H_2O push the d_{xy} orbitals down in a bonding interaction, as clearly visible in Figure 5.4 for the d_{xy} orbital. As a consequence, there is a large splitting (2.7 eV) between the $d_{x^2-y^2}{}^{\uparrow}$ and $d_{xy}{}^{\uparrow}$ orbitals. The situation is different for the higher lying unoccupied $d_{x^2-y^2}{}^{\downarrow}$ and $d_{xy}{}^{\downarrow}$ orbitals. These orbitals are both pushed up by antibonding interactions with the H_2O lone pairs, the $d_{xy}{}^{\downarrow}$ somewhat less by the π interaction with the π lone pairs than the $d_{x^2-y^2}{}^{\downarrow}$ by the σ interaction with the σ lone

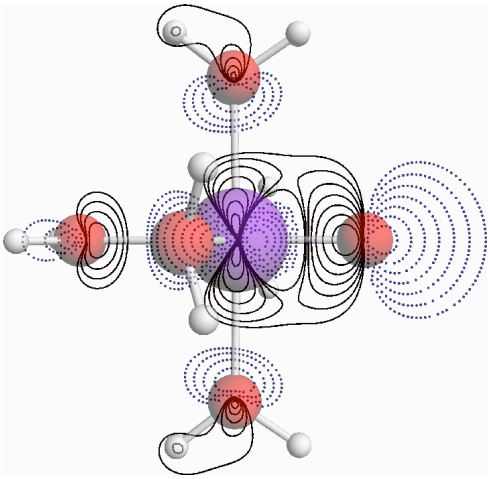

Figure 5.5 *Contour plot of the $3\sigma^{*\uparrow}$ orbital of $[FeO(H_2O)_5]^{2+}$ in the plane of the Fe–O bond. There is both bonding and antibonding overlap between the Fe-$3d_{z^2}$ and the O-$2p_z$ orbitals, explaining the low energy of this antibonding orbital.*

pairs. As a result, the $d_{x^2-y^2}{}^{\downarrow}$ and $d_{xy}{}^{\downarrow}$ levels are split by only 1.1 eV, and the $d_{xy}{}^{\downarrow}$ is clearly the lowest lying empty orbital.

As noted before, the d_δ orbitals, although important for the interaction with the water ligands, do not play a role in the interaction with substrate molecules. However, the effects we have been discussing are important for the spin state of the system. When more strongly σ donating equatorial ligands are used, the $d_{x^2-y^2}{}^{\uparrow}$ may be pushed above the $d_{xy}{}^{\downarrow}$, so that the lowest state would correspond to an empty $d_{x^2-y^2}{}^{\uparrow}$ and occupied $d_{xy}{}^{\downarrow}$. The d_{xy} is then doubly occupied, and the total spin becomes $S = 1$ (only two unpaired $2\pi^*$ electrons), with the consequence that there is less relative stabilization of the $\uparrow$ spin levels. Because the $d_{x^2-y^2}{}^{\uparrow}$ and $d_{xy}{}^{\downarrow}$ levels are not involved in the Fe–O bond, nor in the interaction with substrate molecules, one may assume that the spin-state of FeO^{2+} is not playing a crucial role in its reactivity.[118] However, because the energy level of the $3\sigma^{*\uparrow}$ orbital is of prime importance for the reactivity (as we will show), the decrease in the stabilization of the $\uparrow$ levels when the spin-state changes may still have an important effect on the chemistry.

Another change induced by the H_2O ligands, in which the *axial* water ligand plays a role, is the relative destabilization of the $3\sigma^{*\uparrow}$ with respect to the $2\pi^{*\uparrow}$ and $2\pi^{*\downarrow}$ orbitals. As the precise energy level of the $3\sigma^{*\uparrow}$ orbital is very important, the axial ligand could play a major role in influencing the reactivity of FeO^{2+}. In the case of water ligands the $3\sigma^{*\uparrow}$ remains the most important acceptor orbital, but one could also conceive of ligand environments where the role of the $3\sigma^{*\uparrow}$ and the $2\pi^{*\downarrow}$ orbitals is reversed, leading again to the TSR mechanism as found for FeO^{+}; this has been found, for instance, in the case of cytochrome P450.[99]

We will return to the role of ligands other than H_2O in Chapter 6.

We emphasize that the interaction of substrate molecules with FeO^{2+} is not by way of hydrogen bonding to the oxo oxygen. To act as a H-bond acceptor, FeO^{2+} would have to be able to donate electrons into the σ^* orbital of the O–H bond of the H-bond donor. The $2\pi^{*\uparrow}$ orbital is the only available orbital which would be suitable for this type of interaction. It is, however, so low-lying that it cannot set up effective hydrogen bonds; moreover, the $2\pi^*$ is only half occupied (with $\uparrow$ spin electrons). All interactions with $[FeO(H_2O)_5]^{2+}$ are by way of a charge transfer into the $3\sigma^{*\uparrow}$ orbital.

In view of the importance of the $3\sigma^{*\uparrow}$ orbital for the action of FeO^{2+} as strong electron acceptor, we give a contour plot in Figure 5.5 of the $3\sigma^{*\uparrow}$ orbital of $[FeO(H_2O)_5]^{2+}$. The $3\sigma^*$ orbital is an antibonding combination of the d_{z^2} orbital of Fe and the p_z orbital of the oxo oxygen. There is some hybridization at the O which yields the $3\sigma^*$ a pronounced outward lobe. However, the antibonding of the O-$2p_z$ with d_{z^2} is mitigated by the positive overlap that the p_z can obtain with the equatorial torus of the d_{z^2}. This bonding effect is clearly visible in Figure 5.5. As a result, the overlap between the d_{z^2} and the O-$2p_z$ is only 0.10 (e.g. in O_2 the p_z–p_z overlap is 0.23), and as a result of that, the $3\sigma^*$ orbital is lower in energy than one would generally expect for an antibonding p_z–p_z σ^* orbital: the present $3\sigma^{*\uparrow}$ orbital is only 2.0 eV above the $2\pi^{*\uparrow}$ orbitals, while for O_2, for instance, the gap is 9.2 eV, and for the very reactive F_2 it is still 3.3 eV.

5.3.2. The substrate molecules: methane, methanol and water

A few comments on the frontier orbitals of the substrate molecules water, methane, and methanol are in order. In the figures and tables, we use the orbital energies of these molecules in exactly the configurations they have in the complexes with $[FeO(H_2O)_5]^{2+}$, see Figure 5.1. That means, for instance, that for methane one of the C–H bonds is elongated, so that the degeneracy among the T_2 set of C–H bonding orbitals is lifted, and the orbital most localized on the elongated C–H is at higher energy (–9.07 eV) compared to the other still degenerate orbitals (–9.35 eV). In water the frontier orbitals are the σ and π lone pairs, at –9.25 eV (σ lone pair) and at –7.15 eV (π lone pair). The frontier orbitals of water, methane, and methanol are depicted in Figure 5.6.

Methanol has an particularly interesting HOMO. It is a π^* antibonding combination of a π orbital (with respect to the H–O–C plane) at the OH group and a minus combination of C–H bonding orbitals at the CH_3 group. On account of its antibonding character, this orbital is relatively high lying (–6.00 eV), and therefore more amenable to interaction with the LUMO of FeO^{2+} (both via the OH and the CH lobes) than the HOMOs of the other substrate molecules. Analogous to water, there is also a σ lone pair (in the H–O–C plane), which is the HOMO–1 at –7.83 eV. It also has considerable amplitude at the CH_3 group.

It is important to note that, due to the antibonding interaction between the C–H bonds and the π lone pair at oxygen, the HOMO of methanol is much higher in energy than the HOMO of methane, although both have partly C–H bond character. As a result, methanol has C–H bond character (20-25%, depending on the geometry) in a

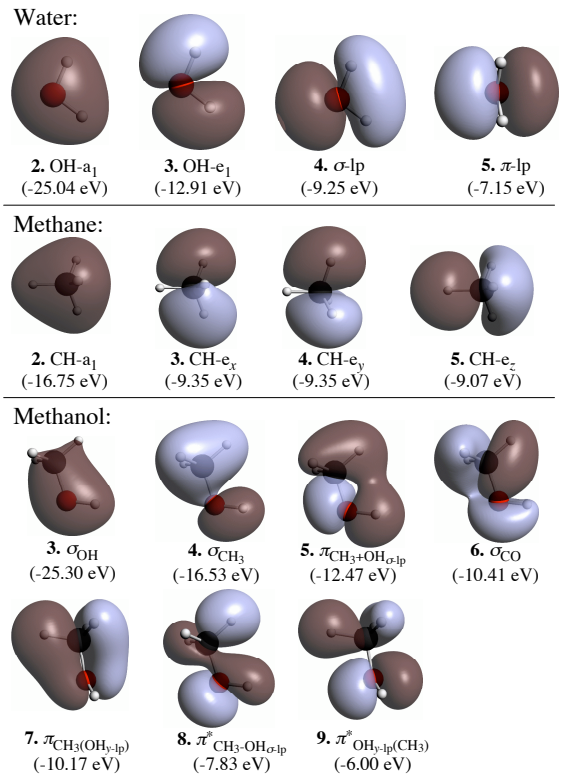

Figure 5.6 *Occupied molecular orbitals of water, methane, and methanol. The geometries of the molecules are taken from the optimized complexes with* $[FeO(H_2O)_5]^{2+}$ *(N.B. the methanol is taken from the CH-bonded complex). The 1s orbitals of the oxygen and carbon atoms are left out of the picture. Note that for different orbitals the molecules may be depicted in different orientations.*

relatively high-lying orbital, which makes the C–H bonds of methanol easier to activate than the C–H bonds of methane.

5.3.3. Interaction of $[FeO(H_2O)_5]^{2+}$ with methane, methanol, and water

The geometries of the optimized complexes are shown in Figure 5.2. The bonding with the C–H bonds of methane and methanol leads to a practically linear Fe–O···H–CR_3 arrangement, but the OH-bonded methanol and the water molecule interact at an angle with the Fe–O bond. However, for all four complexes we studied, the potential energy surfaces are very flat between linear and bent geometries, and the precise geometries are likely to be determined by subtle electrostatic effects; the overlap with the $3\sigma^{*\uparrow}$ orbital of $[FeO(H_2O)_5]^{2+}$ is hardly influenced by these angles.

Note that both the water and the OH-bonded methanol are interacting via their oxygen π lone pairs (the HOMO's). Water rotates to optimize the overlap with its lone

pair, but even the interaction of methanol occurs via its O-2p_π orbital. Indeed, the hydrogen is more or less in between the two oxygen atoms, but it does not point directly to the oxo oxygen and the overlapping orbital is the O-2p_π orbital of methanol. When we force the methanol into an orientation analogous to the orientation of the water molecule, the energy is only marginally higher.

For complexes of $[FeO(H_2O)_5]^{2+}$ with substrate molecules the bonding interaction is characterized by a charge transfer from the HOMO of the substrate molecule into the $3\sigma^{*\uparrow}$ LUMO of FeO^{2+}. We studied the interactions with water, methane, and methanol. The important difference between these molecules, causing the differences in interaction strengths seen in Table 5.1, is the energy of the HOMO: the HOMO can interact more strongly with the unoccupied acceptor orbital when it lies at higher energy. The activation of a C–H bond by electron donation out of the C–H bonding orbital is usually weak due to the low energy of this type of orbital. However, the $3\sigma^{*\uparrow}$ LUMO of $[FeO(H_2O)_5]^{2+}$ is particularly low-lying, as explained before, and is therefore capable of this feat.

The double positive charge of $[FeO(H_2O)_5]^{2+}$ makes it difficult to compare the $3\sigma^*$ energy to that of the HOMOs of the neutral substrate molecules. In Figure 5.7 a schematic picture is shown of the orbital interaction diagrams for the interactions of $[FeO(H_2O)_5]^{2+}$ with methanol, methane, and water. In this schematic picture, only the $\uparrow$ spin orbitals are drawn, and for the $[FeO(H_2O)_5]^{2+}$–molecule complex only the molecular orbitals resulting from the HOMO–LUMO interactions are included. The net positive charge on the $[FeO(H_2O)_5]^{2+}$ unit stabilizes the orbitals of the substrate molecules when they approach (see Section 5.2), and this lowering is reproduced in the figure. Detailed orbital interaction diagrams and tables with the mixing percentages for all orbitals are given in Appendix A.

The important quantities are the mixing percentages with which the fragment orbitals enter the complex orbitals. For CH_4, the (shifted) HOMO lies sufficiently far below the FeO^{2+} LUMO that only a small (but unmistakable) admixture of 11% of the $3\sigma^{*\uparrow}$ into the C–H bond orbital occurs, corresponding to a complexation energy of only –9 kJ/mol. For methanol, the HOMO is at considerably higher energy than the CH_4 HOMO, so a much stronger charge transfer into the $3\sigma^{*\uparrow}$ may be expected. Indeed, both for complexation with a C–H bond (–70 kJ/mol), and complexation with oxygen lone pairs (–57 kJ/mol), the bonds are much stronger than for CH_4. For water the shifted HOMO energy lies in between those of CH_4 and CH_3OH, and the charge transfer interaction is similar to that of CH_4, leading to a very comparable orbital interaction energy. The large difference in the strength of the complexation of water compared to methane (–43 kJ/mol vs. –9 kJ/mol) is a result of the electrostatic interaction (see discussion below). We stress again that the water–oxo bond is *not* a hydrogen bond, but a charge transfer from the HOMO of water into the LUMO of FeO^{2+}.

We now substantiate our picture of the bonding in these cases, in particular the importance of the donor–acceptor orbital interactions, with the data given in Table 5.2

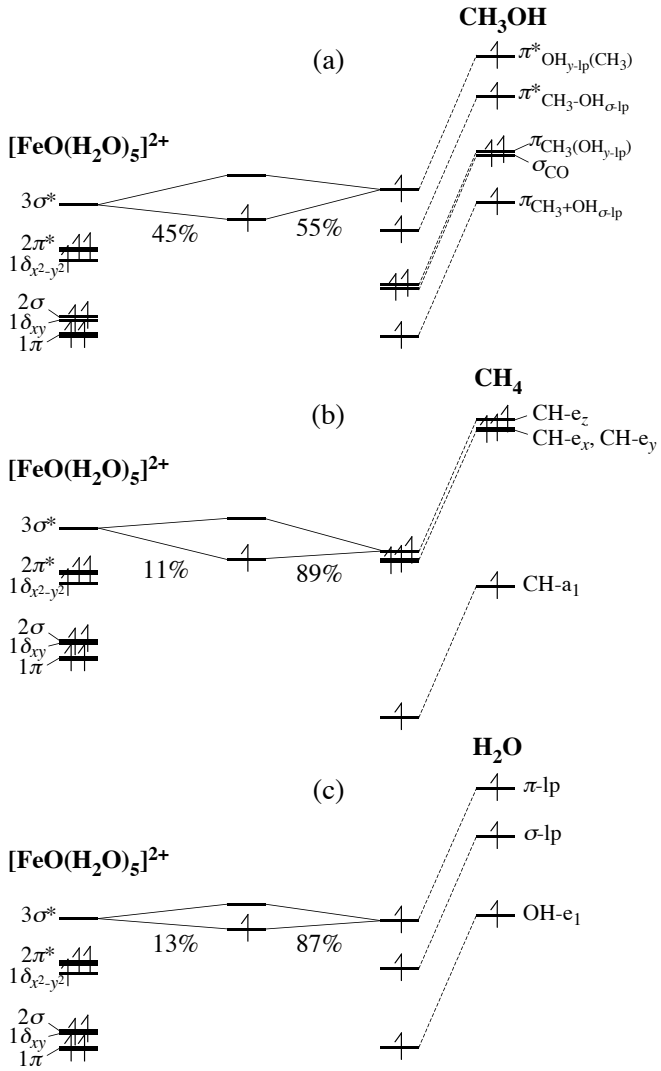

Figure 5.7 *Schematic orbital interaction diagrams for interactions with $[FeO(H_2O)_5]^{2+}$, with only ↑ electrons shown. To the right the orbital energies of the isolated substrate molecules, and in the next columns the stabilized orbital energies due to the approach to the charged $[FeO(H_2O)_5]^{2+}$, see text. Only the mixings of the substrate HOMOs with the $[FeO(H_2O)_5]^{2+}$ LUMO are indicated. The complete diagrams are given in Appendix A.*

Table 5.2 *Energy decomposition of the interactions of methane, methanol, and water with* $[FeO(H_2O)_5]^{2+}$ *in optimized geometries of the reactant complexes. Energies are given in kJ/mol.*

	$FeO–CH_4$	$FeO–CH_3OH$	$FeO–HOCH_3$	$FeO–OH_2$
Deformation energy	3	29	20	2
Pauli repulsion	31	93	30	22
Electrostatic interaction	–11	–36	–6	–35
Orbital interaction	–31	–155	–100	–32
Total bonding energy	–9	–70	–57	–43

and Table 5.3. In Table 5.2, the total interaction energy is decomposed into deformation energy (the energy required to deform a free molecule to the geometry it has in the complex), Pauli repulsion, electrostatic interactions, and orbital interactions (here corresponding to the charge transfer interaction). In Table 5.3 the charge transfer is further analyzed. We have tried to quantify the effect of the 2+ charge of the FeO^{2+} on the HOMO orbital energies of methane, methanol, and water in the manner indicated earlier (the amount by which the orbitals shift is estimated by taking the average shift of the non-interacting orbitals for each molecule). Also, the overlap of the HOMO of the small molecule with the LUMO of $[FeO(H_2O)_5]^{2+}$ has been calculated, as this influences the total strength of the interaction. The trends in the orbital interaction term in the interaction energy can be rationalized using these data.

When we compare methane to methanol (both interacting via their C–H bond), we see a huge difference in the strength of the orbital interaction. This is a direct result of the fact that the HOMO of methanol is at higher energy, also after the stabilization by the 2+ charge, resulting in an orbital interaction of 155 kJ/mol for methanol, versus 31 kJ/mol for methane. This effect is partly canceled by the larger deformation energy and larger Pauli repulsion. This is quite typical: stronger orbital interactions that lead to stronger bonding also lead to shorter bond lengths. So the bonding distance is slightly shorter in the case of methanol, causing larger deformation energies and larger Pauli repulsion. This partly counterbalances the stronger orbital interaction, but methanol nevertheless binds many times stronger than methane, purely because of the difference in the relative orbital energies.

When methanol interacts with FeO^{2+} via its OH group, the orbital interaction is some 55 kJ/mol weaker. This is because in this orientation the overlap of the π^* HOMO of methanol and the $3\sigma^*$ LUMO of FeO^{2+} is considerably smaller (0.017 *versus* 0.045*)*. Naturally, the orbital levels are virtually the same as in the CH-bonding configuration, and since in the final self-consistent field there is near degeneracy between the $3\sigma^*$ and the (stabilized) HOMO of methanol, in both cases the amount of mixing comes close to 50%. But, because of the smaller overlap, the strength of the orbital interaction is weaker in the OH-bonding complex. Note that because of the

Table 5.3 *HOMO–LUMO mixing and interaction energies in the reactant complexes. The HOMO orbital energies of the isolated molecules were all calculated in the optimized geometries of the reactant complexes. The energy of the* $3\sigma^{*\uparrow}$ *orbital of* $[FeO(H_2O)_5]^{2+}$ *is –13.6 eV. For the estimates of the shifted HOMO energies of the substrate molecules in the field of* $[FeO(H_2O)_5]^{2+}$*, see the text.*

	CH_4	CH_3OH	$HOCH_3$	H_2O
HOMO (isolated molecule)	–9.1 eV	–6.0 eV	–6.0 eV	–7.1 eV
Shifted HOMO in field of 2+ charge	–14.1 eV	–13.0 eV	–12.8 eV	–13.7 eV
Overlap of HOMO with FeO LUMO	0.057	0.045	0.017	0.035
Admixing of FeO LUMO	11 %	45 %	42 %	13 %
Orbital interaction	–31 kJ/mol	–155 kJ/mol	–100 kJ/mol	–32 kJ/mol
Total interaction	–9 kJ/mol	–70 kJ/mol	–57 kJ/mol	–43 kJ/mol
H-abstraction barrier	23 kJ/mol	2 kJ/mol	22 kJ/mol	–

weaker bonding as result of the weaker orbital interaction, the Pauli repulsion is also weaker and the deformation energy smaller, so the net difference with the CH-bonding complex is diminished to only 13 kJ/mol.

Finally, we consider the interaction of $[FeO(H_2O)_5]^{2+}$ with a water molecule. In this case, in the optimized geometry, the water molecule orients its π lone pair, the HOMO, towards the FeO^{2+}. Comparing to methane, we note that the orbital energy of the water HOMO is more favorable, but the overlap is less favorable, and the orbital interaction strength of 32 kJ/mol is very similar to the 31 kJ/mol of methane. However, since water has a dipole, the electrostatic interaction with the charged $[FeO(H_2O)_5]^{2+}$ is much stronger, and the Pauli repulsion is smaller (smaller overlaps), so the total interaction energy (–43 kJ/mol) is significantly larger than for methane.

5.3.4. Bond activation

We have proposed a model for the reactivity of FeO^{2+} based on its ability to accept electron charge in its low-lying LUMO. We were also able to explain differences in interaction energies with various substrates on the basis of the relative orbital energies of the species involved. We will now relate this result to the height of the reaction barriers for hydrogen abstraction as given in Table 5.3. These barriers were calculated by optimizing the transition state for hydrogen abstraction, and were found to be extremely low, ranging from only 2 kJ/mol to 23 kJ/mol.

The effectiveness of the C–H bond activation by FeO^{2+}, by charge transfer from the HOMO of the substrate molecule into the LUMO of FeO^{2+}, will depend on the relative orbital energies. For methanol, with its high-lying HOMO, the charge transfer is so large in the transition state that almost a full electron is transferred. As the HOMO of

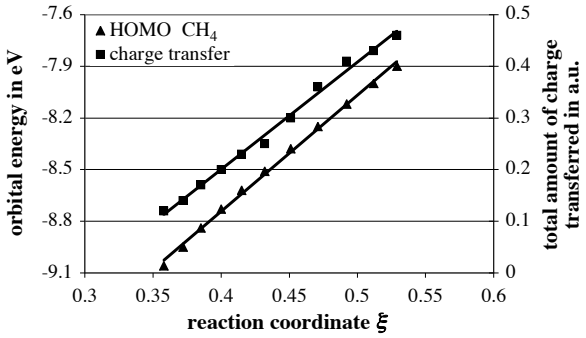

Figure 5.8 *Charge transfer (Mulliken gross population in 3σ* LUMO) during hydrogen abstraction from CH_4 by $[FeO(H_2O)_5]^{2+}$, plotted up to the transition state. For the definition of the reaction coordinate, see text. The orbital energy of the CH_4 HOMO is also displayed.*

methanol has a large contribution from the C–H bond, this means that the C–H bond is considerably weakened. The O–H bond of methanol is much less activated by the charge transfer interaction with FeO^{2+} simply because the O–H bond is not contributing to the HOMO (see Figure 5.6).

For methane it seems surprising that the C–H bond is activated at all, as the complexation energy and the charge transfer in the reactants complex is small. Nevertheless, the hydrogen abstraction barrier is still as low as 23 kJ/mol, because during the stretching of the C–H bond the charge transfer strongly increases and stabilizes the transition state. When the C–H bond lengthens, its orbital energy increases strongly, so in the transition state the charge transfer is much stronger than in the reactants complex. We followed the charge transfer during the reaction, as shown in Figure 5.8. The reaction coordinate ξ was defined as the relative position of the hydrogen between the carbon and the oxygen atoms:

$$\xi = \frac{R_{CH} \cos \angle_{HCO}}{R_{CO}} \tag{5.1}$$

ξ was varied from 0.36 (the value in the reactants complex) to 0.53 (the transition state). At each step the rest of the geometry was optimized. It can be seen that the energy level of the HOMO of free methane increases almost linearly with the reaction coordinate, and the charge transfer correlates perfectly with the orbital energy.

5.4. Results: The effect of solvation on charge transfer and transition state barriers

We have noticed on previous occasions (Ref. 106 and Chapter 4) that in water solution the barrier for hydrogen abstraction is much higher than in the gas phase. This effect was found in Car-Parrinello MD calculations, where the solvent water molecules were represented explicitly and quantum mechanically. An increase of the barrier in

solution compared to gas phase, which often occurs with charged reactants, is usually caused by less solvation stabilization in the transition state compared to the reactants complex. In Ref. 106, the possibility was considered that this differential solvation was causing the barrier increase. However, this could not be established unambiguously as the source of the solvent effect in the present case. We will now consider how the insight we have gained in the electronic structure aspects of the reaction, help us to understand the significant solvent effect for the hydrogen abstraction reaction.

In water solution the net charge of the $[FeO(H_2O)_5]^{2+}$–molecule complex will induce a reaction field in the solvent, which leads to a destabilization of the orbitals relative to the gas phase. So all orbitals, both of the oxoiron complex itself and of the coordinated substrate molecule, shift upwards in energy. However, one may expect this effect to be largest close to the charged centre. In that case, the orbitals of $[FeO(H_2O)_5]^{2+}$, including its $3\sigma^*$ LUMO, are more destabilized than the orbitals of the substrate molecule. Of course, such a change in the relative energies of the orbitals of the two moieties would imply a change in the charge transfer interaction, resulting in a weakening of the interaction strength and of the stabilization of the transition state. In this model, the water solvent directly affects the electronic interactions and hence the reactivity of $[FeO(H_2O)_5]^{2+}$. The effect is not caused by specific interactions of water molecules with the reactants complex and the transition state, but is purely caused by long-range dielectric screening effects of the bulk solvent on the relative level positions of the reactants. Therefore, it should already occur when the solvent is represented by a polarizable continuum model.

To investigate this model, we have repeated the calculations of the reactants complexes and the transition states with a modelled dielectricum around the reactants, using a Conductor-like Screening Model (COSMO). The dielectric constant has been chosen as that of water, $\varepsilon = 78.4$. In these calculations we used the same penta-aqua oxo complexes and transition states as before, only now surrounded by a dielectricum and reoptimized in this environment.

Figure 5.9 contains the geometrical parameters of the reactants complexes in the COSMO environment. The distance between the oxo group and the H of the substrate is much larger than without dielectricum (compare to Figure 5.2). This is in agreement with the much smaller interaction energies, as given in Table 5.4. This table also shows that the transition state barriers have strongly increased. The hydrogen abstraction barrier increases in the solvent by 69, 33, and 51 kJ/mol for methane, methanol CH-bonded, and methanol OH-bonded, respectively.

When the solvation is taken into account, simulated with the COSMO model, the complexation of methanol (at the OH group) and water appears to change qualitatively, occurring via the O–H bonds rather than the oxygen lone pairs. However, a hydrogen bond does not form; the interaction is a charge transfer in both cases (from the substrate molecule into the $3\sigma^*$ orbital of FeO^{2+}).

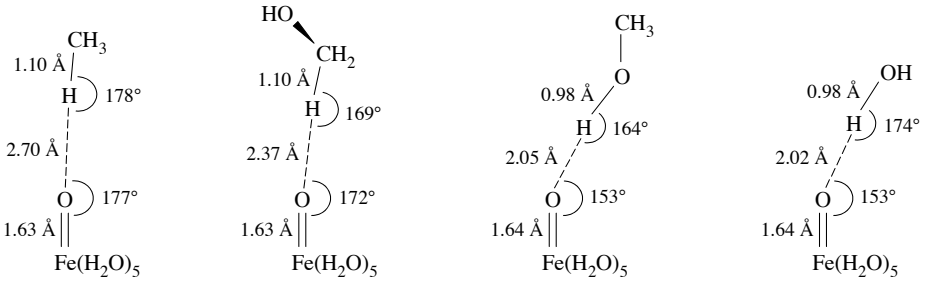

Figure 5.9 *Distances and angles in the $[FeO(H_2O)_5]^{2+}$ complexes with methane, methanol, and water, respectively, optimized in the presence of the COSMO ($\varepsilon = 78.4$) environment.*

To verify that the solvent indeed acts by way of differential level shifts of the ironoxo complex and the substrate molecules, Table 5.4 gives the orbital energies of the relevant frontier orbitals, and Figure 5.10 shows orbital interaction diagrams for gas phase and solvated systems in the case of methanol interacting with $[FeO(H_2O)_5]^{2+}$. Table 5.4 shows that the orbital energies of the isolated neutral substrate molecules in the COSMO calculation differ very little from the gas phase values in Table 5.3. The energy levels of these orbitals shifted by the field of the $[FeO(H_2O)_5]^{2+}$ species are also given, again using the lower lying non-bonding orbitals to obtain an estimate for this shift. Remarkably, the downward shift is now almost negligible, so the screening effect of the solvent on the 2+ charge of $[FeO(H_2O)_5]^{2+}$ is apparently very effective. This means that the orbitals of the substrate molecules are lying considerably higher (5-7 eV) in the COSMO-surrounded complexes compared to the complexes in the gas phase, cf. Table 5.4. However, the $3\sigma^{*\uparrow}$ of charged $[FeO(H_2O)_5]^{2+}$ shifts upwards even more, from –13.6 eV in the gas phase to –5.4 eV in the COSMO environment. So there is a considerable differential shift of the substrate levels and the $[FeO(H_2O)_5]^{2+}$ levels upon COSMO solvation: the latter have undergone a relative destabilization with respect to the substrate orbitals. As a result, the $3\sigma^{*\uparrow}$ of $[FeO(H_2O)_5]^{2+}$ is no longer an effective acceptor orbital for the HOMO of methanol. The effect is quite large, the admixture of the $3\sigma^{*\uparrow}$ into the methanol HOMO in the reactants complex, which was quite strong in the gas phase (45%), is strongly reduced, to only 2% in water solution, with a concomitant reduction in complexation energy from –70 to only –9 kJ/mol.

Such a small complexation energy in the solvent environment does not mean that the transition state cannot be lowered considerably by charge transfer interaction with $[FeO(H_2O)_5]^{2+}$. As previously observed, during the reaction the C–H bond is elongated and the corresponding orbital shifts upward. It will then start to interact more strongly with the $3\sigma^{*\uparrow}$ LUMO of $[FeO(H_2O)_5]^{2+}$, so there will be a much larger interaction energy of methanol with $[FeO(H_2O)_5]^{2+}$ in the transition state, leading to the still modest barrier of 35 kJ/mol.

The weakened complexation interactions in the calculations with the COSMO dielectricum agree with observations in the Car-Parrinello simulations with explicit

Table 5.4 *Influence of water solvation (modeled by a COSMO dielectricum) on the charge transfer interaction. In the COSMO environment, the orbital energy of the $3\sigma^{*\uparrow}$ orbital of $[FeO(H_2O)_5]^{2+}$ is –5.4 eV.*

	CH_4	CH_3OH	$HOCH_3$	H_2O
HOMO (isolated molecule in solvent)	–9.2 eV	–6.2 eV	–6.2 eV	–7.1 eV
Shifted HOMO in field of 2+ charge	–9.3 eV	–6.3 eV	–6.3 eV	–7.2 eV
Admixing of FeO LUMO	0 %	2 %	0 %	0 %
Orbital interaction	–2 kJ/mol	–14 kJ/mol	–8 kJ/mol	–5 kJ/mol
Total interaction	–6 kJ/mol	–9 kJ/mol	–6 kJ/mol	–19 kJ/mol
H-abstraction barrier	92 kJ/mol	35 kJ/mol	73 kJ/mol	–

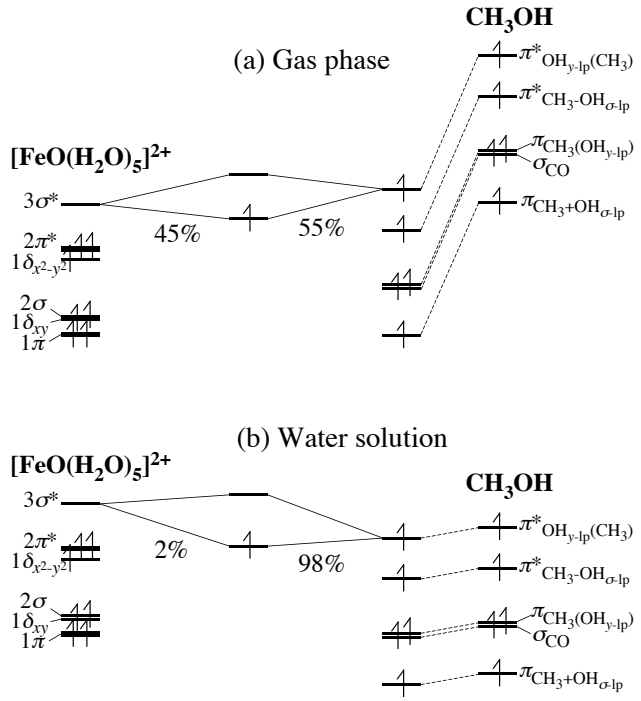

Figure 5.10 *Schematic orbital interaction diagrams showing the effect of water solution on the interactions of $[FeO(H_2O)_5]^{2+}$. The net charge is shielded by the dielectric effect of the solvent, causing the orbitals to shift upwards in energy. Because this shift is largest for the charged fragment, $[FeO(H_2O)_5]^{2+}$, the methanol orbitals are relatively stabilized.*

Table 5.5 *Reaction barriers for hydrogen abstraction by $[FeO(H_2O)_5]^{2+}$ in solvents with varying dielectric constants, modeled with the COSMO model. Dielectric constants are used for vacuum (1), chloroform (4.8), ethanol (24.3), and water (78.4).*

	CH_4	CH_3OH	$HOCH_3$
$\varepsilon = 1$	23	2	22
$\varepsilon = 4.8$	77	17	54
$\varepsilon = 24.3$	90	32	70
$\varepsilon = 78.4$	92	35	73

water molecules: Although the interaction energy could not be measured in the simulations, it was observed that none of the substrates formed a stable complex with FeO^{2+}, and each substrate was replaced by a water molecule. This is in agreement with interactions of 6-9 kJ/mol for methane and methanol and 19 kJ/mol for water (Table 5.4).

The reaction barriers found in the COSMO calculations compare very well, both for methane and for methanol, with the free energy barriers found in the Car-Parrinello simulations. This indicates that entropy effects are fairly small and that the solvation effect can indeed be explained from the effect of the dielectric screening on the electronic structure mechanism of the reaction.

It has been suggested that solvents with smaller dielectric constants, which will exhibit smaller screening effects, may be expected to lower the barrier for hydrogen abstraction considerably compared to water.[106] We have verified this conjecture by calculating the barrier for our model substrates with increasingly less polar solvents, represented in the COSMO model with dielectric constants 24.3 (ethanol) and 4.8 (chloroform). For simplicity we neither changed the first coordination sphere ligands (water molecules) nor the COSMO parameter for the radius of the solvent molecules. Table 5.5 displays the calculated barriers. In agreement with our explanation for the mechanism of the solvent effect, the barriers are considerably lowered, in particular for the low dielectric constant of 4.8 (chloroform). However, the effect for ethanol solvent is small. A more effective method, possibly in combination with tuning the dielectric effect of the solvent, may be to influence the precise energy level of the $3\sigma^*$ orbital by varying the ligands, in particular the axial ligand. This is investigated in Chapter 6.

5.5. Conclusion

The formal description of iron(IV)oxo as Fe^{4+} and O^{2-} suggests that the oxo oxygen would be nucleophilic. However, the FeO bond in FeO^{2+} has a strong covalent character, and FeO^{2+} actually turns out to be an extremely electrophilic (acidic) species. Therefore, it is not capable of acting as an electron donor and forming hydrogen bonds with H-bond donors. Its extreme electrophilicity makes FeO^{2+} an electron acceptor even for poor electron donors such as C–H bond orbitals. Strong charge transfer interactions are established, in which charge is donated out of the HOMO (the C–H bond orbitals) of a substrate into the $3\sigma^{*\uparrow}$ LUMO of FeO^{2+}. As a

result of the considerable charge transfer (up to 50%) out of the C–H bond, the C–H bond is strongly activated for the rebound mechanism in hydroxylation of C–H bonds.

The actual strength of the interaction and the effectiveness of the activation depend on the precise level of the HOMO of the incoming molecule: When all occupied orbitals of the substrate molecule are significantly lower lying in energy than the FeO^{2+} LUMO, the charge transfer is only moderate, and so is the activation. However, when the substrate HOMO lies at equal energy or even higher than the FeO^{2+} LUMO, a huge charge transfer occurs. Typically, the transition state is stabilized even more, because the C–H bond orbital shifts upwards as result of the C–H bond lengthening that occurs in the transition state, leading to surprisingly low reaction barriers. For gas phase $[FeO(H_2O)_5]^{2+}$ the hydrogen abstraction barriers range from a stunning 2 kJ/mol for methanol to 23 kJ/mol for methane.

We have analyzed the electronic structure origin of the remarkably effective electron acceptor property of FeO^{2+}. Of course, the effect of the 2+ charge is important, though reduced by screening effects of the solvent (see below). However, the LUMO of FeO^{2+} is particularly low because the antibonding character of the σ^* of FeO^{2+} is less strong than the antibonding character in, for instance, a $2p_z$–$2p_z$ antibonding orbital. The σ^* is therefore not driven up to such high energies as for instance the $2p_z$–$2p_z$ antibonding orbital of O_2.

As a result, the chemistry of FeO^{2+} is completely driven by this low-lying σ^* orbital. The related FeO^{+} ion is believed to react via a two-state-reactivity (TSR) mechanism and is commonly compared with the O_2 molecule (being a bi-π-radical),[113-115] and for FeO^{2+} complexed with a heme group, for instance in cytochrome P450, the same mechanism has been suggested.[99] However, for high-spin FeO^{2+} the extremely low-lying empty σ^* orbital is much more important than the bi-π-radical character. In this respect FeO^{2+} is more analogous to the F_2 molecule.

We elaborate further on the differences between low-spin or high-spin and heme or non-heme FeO^{2+} in Chapter 6.

The gas phase barriers for the hydrogen abstraction by $[FeO(H_2O)_5]^{2+}$ are much lower than those in water solvent (see Ref. 106 and Chapter 4). This difference is not caused by specific (H-bond) interactions of outer sphere water molecules, but by long range screening effects of the dielectric medium, which are rather strong for a 2+ charged species like $[FeO(H_2O)_5]^{2+}$. The polarization of the dielectricum affects the relative orbital energies. The $3\sigma^*$ LUMO of $[FeO(H_2O)_5]^{2+}$, which was so effective in the C–H bond activation in the gas phase, is shifted almost out of reach for the substrate HOMOs by the solvation. This finding highlights the sensitivity of the activation of C–H bonds to a truly low-lying acceptor orbital, which in the form of the FeO^{2+} $3\sigma^{*\uparrow}$ is present in the gas phase, but is much less available in solution. Of course, when the C–H bond is lengthened and the C–H bonding orbital rises in energy, the interaction with $3\sigma^*$ does set in, and the hydrogen abstraction barrier, although much higher than in the gas phase, is still relatively modest, in particular for methanol in the CH-bonded geometry.

We emphasize that instead of the more common solvation effect of different solvation energies for reactants and transition state, here the solvent influences directly the electronic structure mechanism of the reaction. Since it is a long-range screening effect, an implicit solvent model of solvation (like COSMO) suffices to account for this effect almost quantitatively. The solvation effect occurs via a relative shift of the $3\sigma^{*\uparrow}$ orbital, strongly influencing the charge transfer. A similar effect, in either direction, could be achieved by varying the ligands, especially the axial ligand. Based on our results, the effect of such variations can be predicted from the resulting relative energy level of the $3\sigma^{*\uparrow}$ orbital of the FeO^{2+} moiety. This is further investigated in Chapter 6.

In this work, we have neglected the possible effect of counter anions. When close to the ironoxo complex (otherwise they are screened by the polar solvent), they could have a similar effect as the described solvation effect, as the negative charges also shift the orbitals upward in energy. However, the relative shift of the FeO^{2+} orbitals and the substrate orbitals would strongly depend on the precise position of these counter anions, and could result in an effect in either direction.

Ultimately, insight, derived from the electronic mechanism, into how the solvent affects the reactivity, and how the reactivity can be tuned by ligand effects, may help in the design of useful catalysts based on FeO^{2+} or other metaloxo species. Understanding the solvation effects is a key element in this process.

6.

The role of equatorial and axial ligands in promoting the activity of FeO^{2+} catalysts in alkane hydroxylation*

Abstract:

The influence of surrounding ligands on the alkane hydroxylation activity of FeO^{2+} has been studied. Both the energetic position of the FeO^{2+} $3\sigma^{*\uparrow}$ orbital and the spin state of the system (which in turn also affects the $3\sigma^{*\uparrow}$ energy) depend on the surrounding ligands. We present results of Density Functional Theory (DFT) calculations performed on a series of gas phase complexes of composition $[FeO(H_2O)_n(L)_{5-n}]^{2+}$ (n = 4, 1, 0), derived from the aqueous $[FeO(H_2O)_5]^{2+}$ by substitution of ligand water molecules with L = NH_3, CH_3CN, H_2S, and BF_3. The calculations reveal that the high-spin (quintet) state is favored by weaker σ-donating equatorial ligands, consistent with the literature. The high-spin configuration is more reactive because of significant exchange stabilization of the crucial $3\sigma^{*\uparrow}$ orbital. Once the quintet state is formed by a judicious choice of *equatorial* ligands, the reactivity can be fine-tuned by modulating the energy of the $3\sigma^*$ by varying the nature of the *axial* ligand. A linear relation between the σ donor properties of the axial ligand (estimated from the magnitude of the orbital interaction between σ lone pair and the $3\sigma^*$ orbital) and the activation barrier for the abstraction reaction is observed, and is related to a "push effect" of the σ donors that destabilizes the $3\sigma^*$. We propose that species with enhanced activation properties for hydrogen abstraction relative to $[FeO(H_2O)_5]^{2+}$ might be obtainable by either replacing the axial ligand with a σ donor weaker than H_2O or by preventing ligands from coordinating to iron in an axial position.

---

* This chapter is based on: L. Bernasconi, M.J. Louwerse, and E.J. Baerends, *Eur. J. Inorg. Chem.* **2007** (2007) 3023-3033.

6.1. Introduction

Reactions mediated by iron-containing oxygenases have been studied for over 30 years.[9,101,148,149] In heme (porphyrin) containing enzymes, high-valent ironoxo intermediates were recognized early, in Compounds I and II of catalases, peroxidases, and the cytochromes P450.[150-159] Also in various non-heme iron protein catalyzed processes, high-valent metal states have been postulated as intermediates.[160-163] For non-heme iron proteins, however, only recently the involvement of an ironoxo species has been conclusively proved, specifically in the catalytic cycle of the taurine/α-ketoglutarate dioxygenase (TauD) enzyme.[164-166] Notably, this compound has an $S = 2$ (quintet) ground state,[167] at variance with the $S = 1$ (triplet) state invariantly observed in model porphyrin and non-porphyrin systems, a fact that has been related to the local geometry of the metal coordination environment.[168]

The highly reactive nature of oxoiron intermediates hampers their isolation as stable species, making spectroscopic methods and theoretical studies important sources of information on their structure and mechanistic roles. A number of biomimetic polydentate non-heme ligands, such as 1,4,8,11-tetramethyl-1,4,8,11-tetraaza-cyclotetradecane (TMC)[105,169] and *N*,*N*-bis(2-pyridylmethyl)-*N*-bis(2-pyridyl)methyl-amine (N4Py),[103] have been synthesized recently for stabilizing high-valent iron states, and have been extensively studied since.[170,171] Various ironoxo complexes, with room temperature lifetimes ranging from seconds to days, have been generated and identified spectroscopically, and, to date, three of them have been characterized crystallographically.[169,170,172,173]

In our theoretical work we focus on the *reactivity* of ironoxo species. In Chapter 5, we have discussed the reactivity of $[FeO(H_2O)_5]^{2+}$, and we have shown the importance of its $3\sigma^{*\uparrow}$ orbital, also recognized in the work of Decker et al.[122] In the current chapter, we discuss how different ligands can be chosen to promote the reactivity. We will explain why the high-spin ($S = 2$) species are stronger oxidants than the low-spin ($S = 1$) ones, and how the spin state is determined by the equatorial ligands. Furthermore, we will show how the reactivity can be further regulated via the axial ligand, raising possibilities to create exceedingly strong reagents.

An important issue is the presence and role of different spin states of iron-oxo complexes. The presence of different spin states is a key element in the work on two-state reactivity (mostly of FeO^+) by Schröder, Shaik, Schwarz, and coworkers.[115,116,174] Various computational studies of $S = 2$ Fe^{IV}-oxo systems have appeared (e.g. Refs. 14,117,119,123,175). Schöneboom et al.[176] have applied DFT and various correlated ab initio methods to five-coordinate C_{4v} $[FeO]^{2+}$ complexes. In subsequent work,[124] Neese examined in detail the interplay between triplet and quintet states on the structure, energy, and spectroscopic properties of $[FeO(NH_3)_5]^{2+}$ using (hybrid) DFT and multireference configuration interaction methods. The main factor governing the relative stability of the triplet versus quintet ground state in this simple system was found to be the strength of the equatorial ligand field. The triplet state was found to be lower in energy in the equilibrium geometry (with a distance between the

metal centre and the equatorial N atoms ($R_{FeN_{eq}}$ = 2.062 Å), whereas a lower-energy quintet state was found at larger distances ($R_{FeN_{eq}}$ = 2.203 Å). Very little influence from the *axial* ligand on the triplet–quintet separation was observed. Furthermore, the length and strength of the Fe^{IV}–O bond was found to be similar for the two spin states. On the basis of DFT calculations, it has also been observed that an $S = 1 \rightarrow S = 2$ spin transition would radically change the spectroscopic properties of a $[FeO(TMC)(X)]^{2+}$ species, yet leaving the nature of the Fe^{IV}–O bond essentially unmodified.[119,177]

Although these studies demonstrate that the $S = 1 \rightarrow S = 2$ spin transition has but little effect on the stability of the Fe^{IV}–O bond, this phenomenon has important implications for the *catalytic activity* of $Fe^{IV}O$-containing species. In general, non-heme enzymes (typically $S = 2$) are more reactive than heme ones (typically $S = 1$). The fact that in non-heme iron enzymes the metal ion is in a high-spin state while heme enzymes as well as all known synthetic $Fe^{IV}O$ complexes (with the exception of $[FeO(H_2O)_5]^{2+}$) are low-spin[101] is explained by the weaker ligand field in the non-heme systems. Although it is well recognized that high-spin complexes are more reactive than the low-spin ones, a straightforward explanation seems to be lacking still; we will address this issue in the present chapter.

Not only the equatorial ligands, but also the axial ligand trans to the oxo group affects the reactivity. A classical example of the influence of the axial ligand on the activity of metal centers in enzymes is the "push effect" in the dioxygen cleavage reaction catalysed by cytochrome P450,[178-181] to yield the elusive Compound I.[156,157,176,182-184] A strong electron donation from the thiolate ligand in the proximal site of the heme was first proposed in 1976[178] to be solely responsible for the highly efficient O–O breaking ability of P450.

Although experimental findings have provided some support for this hypothesis,[179,181] a complete model for the catalytic activity of P450 is currently still lacking,[185] and various additional factors (e.g. the presence of potassium ions or specific amino acid residues in the vicinity of the heme site, hydrogen bonds with a proximal cysteine ligand, involvement of a reductase enzyme promoting the electron transfer) may contribute to the regulation of its activity. Isolating and characterizing the role of axial ligand effects on the catalytic activity may therefore provide insight into the relative importance of the different factors promoting reactions catalysed by FeO-containing enzymes.

In studying activation effects toward hydrogen atom abstraction from weak C–H bonds induced by substitution of the *axial* NCMe with CF_3COO^- in the synthetic $S = 1$ complex $[FeO(TMC)(NCMe)]^{2+}$, Rohde and Que[105] advanced the hypothesis that this ligand substitution may be able to induce a weakening of the ligand field and provide access to the more reactive $S = 2$ surface. This study of $[FeO(TMC)(CF_3COO)]^+$, a subsequent one devoted to similar non-heme complexes with anionic ligands, $[FeO(TMC)(NCS)]^+$ and $[FeO(TMC)(N_3)]^+$,[186] and the recent theoretical work of Kamachi et al.[187] devoted to activation effects in the first step of the cyclohexane hydroxylation reaction induced by anionic ligands coordinated to an $Fe^{IV}O$ porphyrin

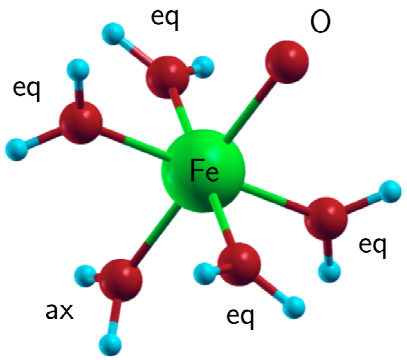

Figure 6.1 *Structure of* $[FeO(H_2O)_5]^{2+}$. *Equatorial and axial ligands are indicated. O is the O(oxo) atom.*

π-cation radical, confirm the remarkable importance of axial ligands in modulating the activity of iron-oxo complexes in organic oxidations.

In the current chapter, we analyze the effects of ligand substitution in simple gas-phase systems of composition $[FeO(H_2O)_n(L)_{5-n}]^{2+}$, with L = NH_3, CH_3CN, H_2S, and BF_3. As for the precursor species $[FeO(H_2O)_5]^{2+}$, in these systems the metal ion is surrounded by a distorted octahedral coordination environment of C_{2v} symmetry, with four equatorial ligands in roughly planar geometry and one axial ligand in trans position to the oxo ion (Figure 6.1). The aim of this study is to gauge the relative importance of axial versus equatorial ligands in: (a) favoring either a low (S = 1) or high (S = 2) spin state; (b) influencing the ability of the system to abstract a hydrogen atom from a methane molecule. We also address the issue of the origin of the higher reactivity in S = 2 versus S = 1 complexes in alkane hydroxylations.

The results are organized as follows. In Section 6.3.1, we study the role of equatorial and axial ligands in influencing the relative stabilities of high- and low-spin states of the compounds $[FeO(H_2O)_n(NH_3)_{5-n}]^{2+}$. In Section 6.3.2, we analyze the hydrogen atom transfer reaction from a methane molecule to each of the latter compounds (corresponding to the first step in $Fe^{IV}O$-catalyzed aliphatic hydroxylations[9]). We verify the more reactive nature of high-spin complexes, which has experimentally often been observed. Here, it is explained as being caused by the strong exchange stabilization of the crucial $3\sigma^{*\uparrow}$ acceptor orbital in high-spin complexes with weak equatorial ligand fields. In Section 6.3.3, we study the manner in which the energy of the latter orbital can be modified by varying the nature of the axial ligand in (high-spin) compounds of composition $[FeO(H_2O)_4(L_{ax})]^{2+}$. The $3\sigma^{*\uparrow}$ is pushed up by stronger σ donors at the axial coordination site, which leads to reduced reactivity. This effect in the high-spin complexes is opposite to the push effect that has been identified in the *low-spin* $Fe^{IV}O$ porphyrin π-cation radical.

The general rules emerging from our study are, first, that weak-field equatorial ligands are needed to obtain the high-spin state, in order to enhance the good acceptor properties (electrophilic nature) of $[L_5FeO]^{2+}$ through stabilization of the acceptor

orbital. Secondly, even higher efficiency of hydrogen atom transfer from methane than in reactions involving $[FeO(H_2O)_5]^{2+}$ might be achievable by occupying the axial coordination site with a weaker donor ligand (or even an electron acceptor), or by leaving it unoccupied and enforcing a square-planar equatorial coordination for iron.

6.2. Computational details

Calculations were performed using ADF[60-62] with a QZ4P basis set for iron and a TZ2P basis set for all other atoms. All electrons were treated explicitly. Relativistic effects were included using the Zero-Order Regular Approximation (ZORA).[64] In the majority of the calculations exchange-correlation effects were described at the BLYP[65,66] level of theory.

Standard generalized gradient corrections (GGAs), as well as the local density approximation, are known to disfavor high-spin states in Fe^{II} and Fe^{III} complexes, as opposed to hybrid and some meta-GGA functionals.[127,128,188] For this reason, in determining the most stable spin state for the ground state of each of the complexes examined, we performed additional full geometry optimization using the OPBE functional, a combination of the OPTX[189] and the PBE[190] functionals. OPBE has been shown to yield spin state relative stabilities comparable to hybrid and meta-GGA prescriptions.[100,127]

6.3. Results and discussion

6.3.1. Ligand induced spin transition in $[FeO(H_2O)_n(NH_3)_{5-n}]^{2+}$ complexes

Detailed discussions of the electronic structure of FeO^{2+} and of its "microsolvated" counterpart $[FeO(H_2O)_5]^{2+}$ (**1**) are given in Chapter 5 and in Refs. 14, 117, and 122. The characteristic one-electron spectrum of $[FeO(H_2O)_5]^{2+}$ in its quintet ground state (Figure 5.3) shows significant stabilization of the majority spin (↑) orbitals, caused by the exchange field generated by four unpaired ↑ electrons. For the $d_{xy}^{\uparrow}/d_{xy}^{\downarrow}$ pair there are additional sources for the especially large gap (see below). Overlap of 3d and O(oxo)-2p orbitals leads to bonding/antibonding pairs of σ symmetry (2σ: $d_{z^2}+p_z$, doubly occupied; $3\sigma^*$: $d_{z^2}-p_z$, virtual) and π symmetry (1π: $d_{xz,yz}+p_{x,y}$, doubly occupied; $2\pi^*$: $d_{xz,yz}-p_{x,y}$, singly occupied). The d orbitals of δ symmetry, $d_{x^2-y^2}$ and d_{xy}, cannot mix by symmetry with O-$2p_z$ orbitals; they are one hundred percent d (in FeO^{2+}) and Fe–O nonbonding.

We pay some attention to the electrons in the d_δ orbitals, since these electrons, although they occupy orbitals that are not involved in the Fe–O bonding and therefore might seem to be mere spectator electrons for reactions involving the Fe–O bond, in fact will be seen to determine the spin state of the system in the various ligand environments, and therefore play an important (albeit indirect) role in the reactivity. The $d_{xy}/d_{x^2-y^2}$ pair with ↑ spin (both singly occupied) are degenerate in bare FeO^{2+}, but the degeneracy is lifted in the $[FeO(H_2O)_5]^{2+}$ complex by antibonding interactions of the $d_{x^2-y^2}$ orbital with the σ lone pairs of the equatorial water molecules and by bonding interactions of the d_{xy} orbital with their π lone pairs.[117] Overall, these contributions

bring about a difference in energy of 2.69 eV between the occupied orbitals $d_{xy}^{\uparrow}$ and $d_{x^2-y^2}^{\uparrow}$. The gap between the corresponding unoccupied orbitals $d_{xy}^{\downarrow}$ and $d_{x^2-y^2}^{\downarrow}$ is much smaller (1.13 eV), since they are both above the water lone pairs and are both pushed up (only the $d_{xy}^{\downarrow}$ less so by the weaker π interactions than the $d_{x^2-y^2}^{\downarrow}$ by the stronger σ interactions). Nevertheless, the fact that $d_{xy}^{\uparrow}$ is pushed down, on top of being stabilized by the exchange field of the excess $\uparrow$ spin electrons, and the $d_{xy}^{\downarrow}$ is pushed up, on top of being less stabilized by the exchange field, leads to the particularly large gap of 4.25 eV between this $\uparrow/\downarrow$ pair.

We consider now the substitution of the ligand water molecules with ammonia molecules to yield axially mono-substituted $[FeO(H_2O)_4(NH_3)]^{2+}$ (**1a**), equatorially substituted $[FeO(NH_3)_4(H_2O)]^{2+}$ (**1 b**), and the fully ammoniated complex $[FeO(NH_3)_5]^{2+}$ (**1c**). The Kohn-Sham levels for these complexes are shown in Figure 6.2. The mono-substituted complex **1a** was found to possess a quintet ground state, albeit the difference in energy between quintet and triplet was found to decrease compared to the all-water complex **1** (Table 6.1). Consistent with Ref. 127, we find the BLYP functional to underestimate the absolute value of the quintet–triplet energy difference as compared to OPBE. The two do, however, yield a ground state with the same multiplicity in all complexes. For **1b** and **1c** the triplet state appears to be preferred, although the difference in energy between the two spin states, particularly in the fully ammoniated system, is small. So, in agreement with the results of Ref. 124, we find here that the spin state of the complex is almost completely determined by the nature of the equatorial ligands: electron-donating ligands in equatorial position favor the low-spin triplet state.

The reason is simple. Equatorial substitution selectively affects the energy of orbitals extending in the *xy* plane. Since the σ lone pair of NH_3 is more electron-donating than the σ lone pair of H_2O, an orbital like $d_{x^2-y^2}$ with antibonding σ interactions with the ligands is strongly destabilized, and the $d_{x^2-y^2}^{\uparrow}$ moves in the orbital spectrum close to the $3\sigma^{*\uparrow}$ (Figure 6.3). It actually becomes so high-lying that it loses its electron to the empty, now lower lying $\downarrow$ spin orbital $d_{xy}^{\downarrow}$. It should be noted that the effect of equatorial NH_3 substitution is different for the d_{xy} orbitals of $\uparrow$ and $\downarrow$ spin. The $d_{xy}^{\uparrow}$ loses the pushing down effect of the higher lying π lone pairs of the equatorial waters and moves up, like $d_{x^2-y^2}^{\uparrow}$ did; the $d_{xy}^{\downarrow}$ loses the pushing up effect of the lower lying water π lone pairs and moves down, so that it even more readily accepts the electron of the destabilized $d_{x^2-y^2}^{\uparrow}$. The electron transfer from $d_{x^2-y^2}^{\uparrow}$ to $d_{xy}^{\downarrow}$ entails a spin flip, with the effect that the stabilizing exchange field for the $\uparrow$ spin orbitals becomes smaller, which provides an additional relative destabilization of $d_{x^2-y^2}^{\uparrow}$ with respect to $d_{xy}^{\downarrow}$. This spin flip leaves only two unpaired $\uparrow$ spin electrons in the $2\pi^*$ orbitals, hence a triplet state. We note that, finally, the $d_{xy}^{\uparrow}$ and $d_{xy}^{\downarrow}$, which are both occupied, have now a much reduced gap (ca. 0.7 eV) compared to the initial gap of 4.2 eV. The remaining gap reflects the remaining exchange stabilization of the two excess $\uparrow$ spins in the $2\pi^*$ orbitals. Since electron transfer from the $d_{x^2-y^2}^{\uparrow}$ to the $d_{xy}^{\downarrow}$ orbital occurs between orbitals with nonbonding Fe–O character, the stability of the Fe^{IV}–O

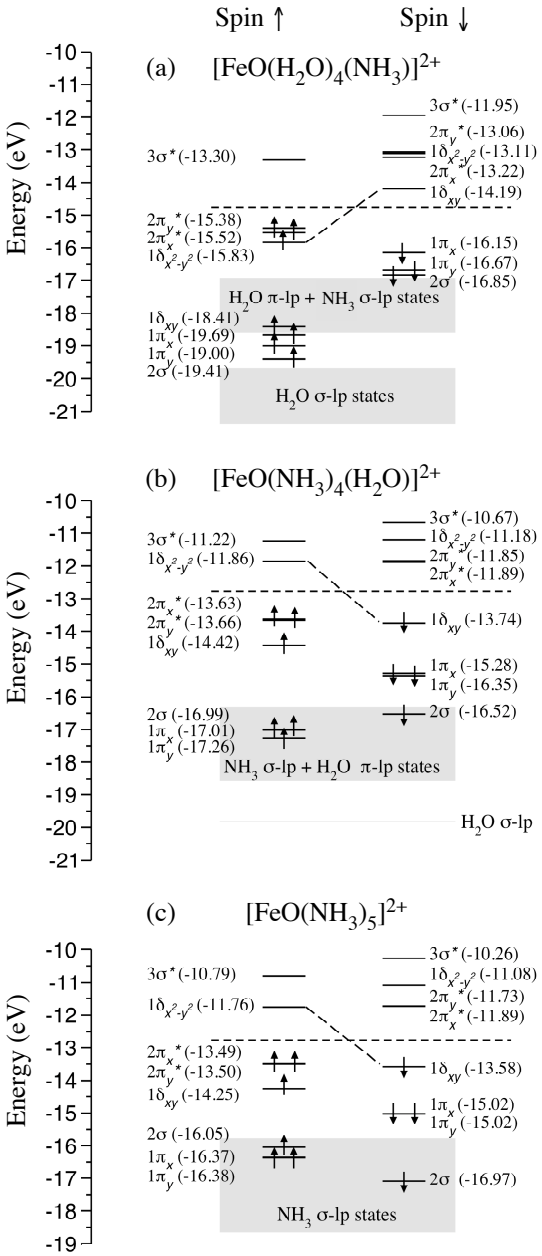

Figure 6.2 *Kohn-Sham energy levels of axially (top), equatorially (centre), and fully NH_3-substituted $[FeO(H_2O)_n(NH_3)_{5-n}]^{2+}$ (n = 4, 1, 0) complexes. The first system is in a quintet ground state, the second and third in a triplet. Oblique dashed lines indicate the energy difference between $1\delta_{x^2-y^2}{}^{\uparrow}$ and $1\delta_{xy}{}^{\downarrow}$ orbitals. See main text for details.*

Table 6.1 *Second and third columns: differences between quintet (S = 2) and triplet (S = 1) ground state energies of* $[FeO(H_2O)_n(NH_3)_{5-n}]^{2+}$. *Data refer to fully optimized geometries for each spin state. Fourth through eighth column: BLYP energies of selected Kohn-Sham spin orbitals in the ground state with the most stable spin multiplicity (S = 2 for* ***1*** *and* ***1a****, S = 1 for* ***1b*** *and* ***1c****). o and e indicate occupied and empty orbitals, respectively. Note the change in occupations in going from* ***1a*** *to* ***1b****. All values are in eV.*

		BLYP	OPBE	$1\delta_{x^2-y^2}{}^{\uparrow}$	$2\pi_x{}^{*\uparrow}$	$2\pi_y{}^{*\uparrow}$	$1\delta_{xy}{}^{\downarrow}$	$3\sigma^{*\uparrow}$
1	$[FeO(H_2O)_5]^{2+}$	–0.280171	–1.131758	–15.95 *o*	–15.64 *o*	–15.60 *o*	–14.39 *e*	–13.62 *e*
1a	$[FeO(H_2O)_4(NH_3)]^{2+}$	–0.206509	–0.697896	–15.83 *o*	–15.52 *o*	–15.38 *o*	–14.19 *e*	–13.30 *e*
1b	$[FeO(H_2O)(NH_3)_4]^{2+}$	0.523687	0.139269	–11.86 *e*	–13.63 *o*	–13.66 *o*	–13.74 *o*	–11.22 *e*
1c	$[FeO(NH_3)_5]^{2+}$	0.443386	0.049770	–11.76 *e*	–13.49 *o*	–13.50 *o*	–13.58 *o*	–10.79 *e*

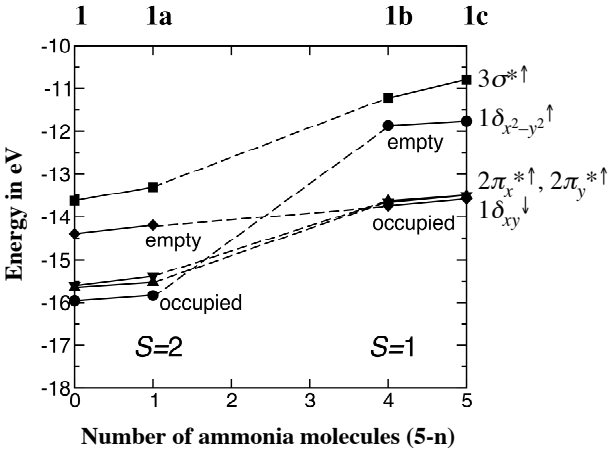

Figure 6.3 *Energies of selected spin orbitals of* $[FeO(H_2O)_n(NH_3)_{5-n}]^{2+}$ *as a function of the number of ammonia molecules (5–n) in the complex. Lines are guides for the eye.*

Table 6.2 *Selected bond distances in Å in* $[FeO(H_2O)_n(NH_3)_{5-n}]^{2+}$ *(n = 5, 4, 1, 0) complexes. All geometries have been optimized in both high- and low-spin states. Subscripts ax and eq refer to ligands in axial and equatorial positions, respectively. For equatorial distances, averages over four values are reported.*

		$\langle O_{eq}–Fe\rangle$		$O_{ax}–Fe$		$\langle N_{eq}–Fe\rangle$		$N_{ax}–Fe$		Fe–O	
		S = 1	*S* = 2	*S* = 1	*S* = 2	*S* = 1	*S* = 2	*S* = 1	*S* = 2	*S* = 1	*S* = 2
1	$FeO(H_2O)_5]^{2+}$	2.000	2.106	2.117	2.091	–	–	–	–	1.627	1.621
1a	$[FeO(H_2O)_4(NH_3)]^{2+}$	2.018	2.121	–	–	–	–	2.173	2.147	1.641	1.636
1b	$[FeO(H_2O)(NH_3)_4]^{2+}$	–	–	2.215	2.153	2.079	2.232	–	–	1.633	1.627
1c	$[FeO(NH_3)_5]^{2+}$	–	–	–	–	2.087	2.244	2.221	2.173	1.647	1.641

bond is barely affected.[119,124,177] This is confirmed by the Fe^{IV}–O bond length changing no more than ~0.02 Å for different compositions and/or spin states (Table 6.2). The spin flip nevertheless has a crucial effect on the reactivity, because of the loss of (part of) the exchange stabilization of the $3\sigma^{*\uparrow}$ orbital. The role of the $3\sigma^{*\uparrow}$ orbital in the reactivity is discussed in the following sections.

Substitution of only the axial water molecule in **1** with ammonia has a very moderate destabilizing effect (upshift of 0.1-0.3 eV) for all orbitals of π and δ symmetry (Figure 6.3), consistent with the fact that their wavefunctions have zero overlap with the σ lone pair of the axial NH_3. Replacement of the axial water molecule with ammonia, however, does more visibly affect orbitals with lobes along the z axis (the Fe–O bond axis) like the 2σ which is pushed down by the higher lying NH_3 lone pair by ca. 1 eV, and the $3\sigma^*$ orbital, which is pushed up by ca. 0.3 eV. In fact, the overall orbital energy pattern is little affected by substitution of only the axial water molecule, and this substitution is not in itself able to induce a transition from high- to low-spin multiplicity, although a small destabilization of the $S = 2$ state versus $S = 1$ is observed, possibly caused by changes in the geometry of the equatorial ligand environment (Table 6.2). In either spin state, the effects of axial ligands on the energy of the $3\sigma^*$ orbital (pushing up in case of stronger donors) will have a similar effect on the reactivity. This will be discussed in Section 6.3.3.

Overall, the $S = 2 \rightarrow S = 1$ spin conversion upon equatorial NH_3 substitution has the effect of raising the axial $3\sigma^{*\uparrow}$ orbital away from the vicinity of the Fermi energy. This fact will be shown to bear remarkable consequences on the electron-acceptor properties of the coordinated FeO^{2+} group.

6.3.2. Ligand effects on hydrogen abstraction from methane

Alkane hydroxylation by $Fe^{IV}O^{2+}$ species follows a rebound mechanism.[9,106,107,191] First, one hydrogen atom is abstracted from the substrate to yield $Fe^{III}OH^{2+}$ and a carbon radical. The latter then collapses onto the hydroxyl oxygen. In Chapter 5, it has been emphasized that the ability of FeO^{2+} to promote hydrogen abstraction is directly connected to its electrophilic character: the FeO···HR bond is established by electron donation out of the R–H bonding orbitals into a low-lying acceptor orbital on FeO^{2+}, namely the $3\sigma^{*\uparrow}$ orbital.

Analysis of the interaction between $[FeO(H_2O)_5]^{2+}$ and various substrate molecules (CH_4, CH_3OH, and H_2O) has indeed shown that the $3\sigma^{*\uparrow}$ orbital plays a cardinal role in driving hydrogen abstractions (see Chapter 5). In all these cases, the abstraction reaction was found to follow an identical pattern, involving as first step the formation of a $[FeO(H_2O)_5]^{2+}$–substrate encounter complex. The bonding energy of the complex, ranging from 9 (CH_4) to 70 (CH_3OH) kJ/mol, reflects the amount of interaction between the donor orbital (HOMO) of the substrate and the $3\sigma^{*\uparrow}$ orbital of $[FeO(H_2O)_5]^{2+}$. In the case of methane, the in-phase combination of one of the T_2 molecular orbitals and the $3\sigma^{*\uparrow}$ orbital has 89% T_2 and 11% $3\sigma^{*\uparrow}$ character. This situation corresponds to a partial transfer of an electron from the donor to the acceptor. In the more tightly bound methanol complex the mixing of donor and $3\sigma^{*\uparrow}$ in their

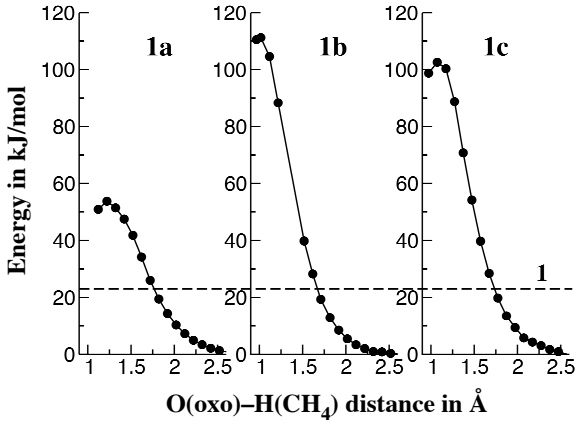

Figure 6.4 *Energy barriers for C–H bond cleavage in axially (**1a**), equatorially (**1b**), and fully (**1c**) NH_3-substituted $[FeO(H_2O)_5]^{2+}$. The total energy of the $[FeO(H_2O)_n(NH_3)_{5-n}]^{2+}$ + CH_4 complex is represented here as a function of the constrained O(oxo)–H distance. The energy of the reactant complex is taken as zero point of the energy scale. The dashed line indicates the barrier height for $[FeO(H_2O)_5]^{2+}$ (**1**).*

bonding combination is 55 – 45%, indicating that the electron is almost equally shared between the donor orbital and the $3\sigma^{*\uparrow}$ orbital. In both the methane and methanol complexes, the donor orbital is essentially a C–H σ bond. Partial promotion of an electron to the $3\sigma^{*\uparrow}$ orbital thus results in a weakening of this bond. Since the overall reaction brings about the net transfer of one electron from the substrate to $[FeO(H_2O)_5]^{2+}$ via a concerted bond breaking (substrate–H) and bond formation (H–OFe),[9] partial electron transfer in the reactants corresponds to a starting electronic structure more similar to the transition state, hence to a lower activation barrier. The stronger the electron-sharing interaction between the substrate molecule and $[FeO(H_2O)_5]^{2+}$ in the encounter complex, the more facile is then the abstraction of the hydrogen atom from the substrate.

Here, we evaluate the effect of various ligands on the energy of the $3\sigma^{*\uparrow}$, and we confirm that the reactivity of the complex can be regulated this way.

We show in Figure 6.4 abstraction barriers for the reaction of CH_4 with the axially, equatorially, and fully ammoniated complexes **1a**, **1b**, and **1c**. The energy of the $3\sigma^{*\uparrow}$ orbital is 0.32 (in **1a**), 2.4 (in **1b**), and 2.8 eV (in **1c**) higher than in the ammoniated complex **1** (Table 6.1). These complexes are representative of (a) an $S = 2$ system (the complex **1a**) with moderate $3\sigma^{*\uparrow}$ destabilization (as compared to the all-water complex **1**), and (b) two $S = 1$ systems (the complexes **1b** and **1c**) with large and comparable $3\sigma^{*\uparrow}$ destabilization. Reaction profiles were obtained by (unconstrained) preliminary optimization of the encounter complex followed by constrained reduction of the O(oxo)–H distance. For each value of the constraint, a full geometry optimization was carried out. The reaction barrier for hydrogen abstraction is defined here as the

difference in total energy between the transition state (at the maximum of each curve) and the energy of the reactant complex. We computed barriers of 54, 111, and 103 kJ/mol for **1a**+CH_4, **1b**+CH_4, and **1c**+CH_4, respectively. These should be compared to the value for the **1**+CH_4 abstraction reaction, 23 kJ/mol (Table 5.1). Overall, a decrease in the reaction rate is therefore observed in the sequence **1** > **1a** > **1b** ≈ **1c**.

The transition to the triplet ground state as result of equatorial substitution (i.e. going from **1** to **1b**) raises the height of the barrier roughly by a factor of four. Substitution of the axial water molecule, both in **1** and **1b** has, by contrast, only a moderate effect. This trend mirrors the moderate destabilization of the $3\sigma^{*\uparrow}$ orbital, 0.3 eV (**1** → **1a**) and 0.4 eV (**1b** → **1c**), to be compared to the much larger effect of equatorial substitution and spin flip, e.g. 2.5 eV for **1a** → **1c**. We do observe, however, that, although the $3\sigma^{*\uparrow}$ destabilization is moderate in both **1** → **1a** and **1b** → **1c**, the latter substitution (axial ligand) results in a much larger increase in the reaction barrier. This is the only case in which no correlation is observed between the $3\sigma^{*\uparrow}$ orbital energy and the reaction barrier, and this indicates that in triplet compounds the reactivity is no longer *exclusively* determined by the $3\sigma^{*\uparrow}$ orbital alone. The ability of the $3\sigma^{*\uparrow}$ orbital to act as an electron accepting orbital depends in the first place on its energy relative to the donating orbital of the substrate, for which the energy of acceptor orbital and the donor orbital should be compared in the same conditions (geometry, overall charge, etc.) as in the starting reactant complex. A second factor contributing to the donor–acceptor interaction is the spatial distribution of the $3\sigma^{*\uparrow}$ orbital. Since the electron transfer occurs at the oxygen side of the FeO group and the $3\sigma^{*\uparrow}$ orbital arises from a combination of the Fe-$3d_{z^2}$ and the O(oxo)-$2p_z$ orbital, the large contribution from the latter (ca. 50%) results in enhanced in-phase overlap of the $3\sigma^{*\uparrow}$ with the donor orbital.

For a given substrate, the variation of the energy of the $3\sigma^{*\uparrow}$ orbital in the $[L_5FeO]^{2+}$ complex caused by ligand replacement or other environmental changes provides a qualitative index of reactivity. An upward shift of the $3\sigma^{*\uparrow}$ orbital results in larger activation barriers. The changes that induce a rise in the orbital energy of $3\sigma^{*\uparrow}$ lead to a concomitant reduction of the amplitude of the $3\sigma^{*\uparrow}$ orbital at the oxo side. Axial substitution pushes the $3d_{z^2}$ up directly, and equatorial substitution does so indirectly by causing a spin flip and a weaker exchange field. The relative contributions of Fe-$3d_{z^2}$ to the acceptor orbital $3\sigma^{*\uparrow}$ therefore increase along the sequence **1** → **1a** → **1b** → **1c**, varying as 37%, 42%, 52%, 51%, and those of O(oxo)-$2p_z$ diminish, 48%, 30%, 25%, 23%, respectively. So there is a progressive localization of the orbital on the metal centre and a consequent decrease in the ability to overlap with the donor on the O(oxo) side. Both factors, the higher orbital energy of the $3\sigma^{*\uparrow}$ orbital and the decreasing amplitude at the oxo side, work in the same direction in increasing the activation barrier.

We note that this model, using only the $3\sigma^{*\uparrow}$ acceptor orbital and the C–H bonding orbital as donor, applies strictly only to those FeO^{2+} complexes in which the $3\sigma^{*\uparrow}$ orbital is the only important acceptor orbital. This only holds for a quintet ground state. The $S = 2 \rightarrow S = 1$ transition not only destabilizes the $3\sigma^{*\uparrow}$, decreasing its electron

Table 6.3 *BLYP Kohn-Sham orbital energies (in eV) for optimized complexes of composition* $[FeO(H_2O)_4(L_{ax})]^{2+}$*, where* L_{ax} *indicates the axial ligand.*

	$1\delta_{x^2-y^2}{}^{\uparrow}$	$2\pi_x{}^{*\uparrow}$	$2\pi_y{}^{*\uparrow}$	$3\sigma^{*\uparrow}$	$1\delta_{xy}{}^{\downarrow}$	$1\delta_{x^2-y^2}{}^{\downarrow}$	$2\pi_x{}^{*\downarrow}$	$2\pi_y{}^{*\downarrow}$
$[FeO(H_2O)_5]^{2+}$	–15.95	–15.64	–15.60	–13.62	–14.39	–13.26	–13.35	–13.28
$[FeO(H_2O)_4(NH_3)]^{2+}$	–15.83	–15.52	–15.38	–13.30	–14.19	–13.11	–13.22	–13.06
$[FeO(H_2O)_4(H_2S)]^{2+}$	–15.70	–15.54	–14.85	–13.68	–14.27	–13.12	–13.32	–13.25
$[FeO(H_2O)_4(CH_3CN)]^{2+}$	–15.23	–15.07	–15.07	–12.90	–13.66	–12.57	–12.84	–12.83
$[FeO(H_2O)_4(BF_3)]^{2+}$	–16.15	–16.03	–15.98	–14.13	–14.58	–13.44	–13.71	–13.65
$[FeO(H_2O)_4(o)]^{2+}$	–16.64	–16.64	–16.48	–14.78	–15.19	–13.91	–14.32	–14.13

acceptor ability, but it also opens an alternative electron transfer channel through the now lower lying $2\pi_x{}^{*\downarrow}$ and $2\pi_y{}^{*\downarrow}$ orbitals (Figure 6.3, **1b** and **1c**). An incoming substrate molecule might then interact with the $3\sigma^{*\uparrow}$ and $2\pi_{x,y}{}^{*\downarrow}$ simultaneously, leading to an Fe–O–H angle considerably smaller than the 180° we have observed in the quintet state investigated in Chapter 5. The proximity of the empty $2\pi_{x,y}{}^{*\downarrow}$ orbitals, even in the quintet state, will make the energy surface of the reactant complex, and probably also of the transition state, rather flat with respect to the Fe–O–H angle.

6.3.3. Axial ligand influence on reactivity

We showed in the previous sections that: (1) the spin state of a complex $[FeO(L_{eq})_4(L_{ax})]^{2+}$ is determined by the nature of the equatorial ligands (L_{eq}) alone; (2) the quintet ground state is more reactive than the triplet in hydrogen abstractions; (3) the reactivity of the quintet ground state is driven by transfer of an electron to a low-lying $3\sigma^{*\uparrow}$ orbital; (4) the axial ligand (L_{ax}) regulates the reactivity of the complex by inducing relatively minor (few tenths of an eV) shifts in the energy of the $3\sigma^{*\uparrow}$ orbital. In this section we address the issue of how the latter effect can be directed to tuning the reactivity of an Fe^{IV}–O complex in C–H bond cleavage.

We examined a series of simple systems $[FeO(H_2O)_5]^{2+}$ in which either the axial or the equatorial ligand water molecules were substituted with CH_3CN or H_2S and that carried the same charge. Similar to the $[FeO(H_2O)_n(NH_3)_{5-n}]^{2+}$ complexes described above, a transition to a triplet ground state was observed for $L_{eq} = CH_3CN$, irrespective of the nature of L_{ax}. The situation is far less clear in the H_2S-substituted complexes, for which energy differences between the quintet and triplet states after equatorial substitution are within 0.02 eV. In both CH_3CN and H_2S complexes, however, replacement of only the axial ligand was not sufficient to favor the triplet over the quintet state, similar to NH_3 substitution, OPBE quintet–triplet energy differences being ~0.4 and ~0.2 eV in the CH_3CN and H_2S complexes, respectively. In particular, we observed an overall change of no more than ~0.2 eV in the energy difference between $1\delta_{xy}{}^{\downarrow}$ and $1\delta_{x^2-y^2}{}^{\uparrow}$ as a result of the replacement of the axial ligand (Table 6.3).

Replacement of the axial ligand in $[FeO(H_2O)_4(L_{ax})]^{2+}$ was found to decrease slightly the energy of the $3\sigma^{*\uparrow}$ orbital in the case of H_2S (–0.06 eV) and to increase it by 0.72 eV in the case of CH_3CN. The relative $3\sigma^{*\uparrow}$ contribution to the in-phase

Table 6.4 *Percentage $3\sigma^{*\uparrow}$ character in the in-phase $3\sigma^{*\uparrow}$–e_z orbital overlap for methane complexes (% $3\sigma^{*\uparrow}$) in reactant complex (RC) and transition state (TS) geometries. Percentage contribution of σ lone pair (or e_1 in $[FeO(H_2O)_4(BF_3)]^{2+}$) to $3\sigma^{*\uparrow}$ (% Ax-σ-lp). C–H bond cleavage barrier (ΔE_{TS}, in kJ/mol) for hydrogen abstraction from CH_4.*

	% $3\sigma^{*\uparrow}$		% Ax-σ-lp	ΔE_{TS}
	RC	TS		
$[FeO(H_2O)_5]^{2+}$	11	46	1.71	23
$[FeO(H_2O)_4(NH_3)]^{2+}$	7	52	4.95	54
$[FeO(H_2O)_4(H_2S)]^{2+}$	10	49	1.94	25
$[FeO(H_2O)_4(CH_3CN)]^{2+}$	7	49	3.06	41
$[FeO(H_2O)_4(BF_3)]^{2+}$	25	54	< 1	7
$[FeO(H_2O)_4(o)]^{2+}$	34	48	0	1

$3\sigma^{*\uparrow}$–e_z orbital combination is very similar in the H_2O and H_2S complexes (11% and 10% respectively) as well as in the CH_3CN and NH_3 complexes (both 7%). C–H cleavage reaction barriers vary according to the sequence $[FeO(H_2O)_4(H_2S)]^{2+} \approx [FeO(H_2O)_5]^{2+} < [FeO(H_2O)_4(CH_3CN)]^{2+} < [FeO(H_2O)_4(NH_3)]^{2+}$.

This mirrors the total amount of $3\sigma^{*\uparrow}$–e_z orbital interaction in the reactant complex and, to a lesser extent, the absolute energy of the $3\sigma^{*\uparrow}$ orbital. The initial $3\sigma^{*\uparrow}$–e_z orbital interaction is a good index of reactivity, since in all complexes the transition state is characterized by an equal distribution of the electron between the donor and acceptor orbitals (Table 6.4), which will be obtained more readily if the starting point is more strongly mixed. The overall height of the activation barrier is therefore correlated with the $3\sigma^{*\uparrow}$ contribution to the CH_4–$[FeO(H_2O)_4(L_{ax})]^{2+}$ charge-transfer state; the larger this quantity the lower the activation barrier.

We have verified now that a stronger σ-donating axial ligand decreases the ability of a $[FeO(H_2O)_4(L_{ax})]^{2+}$ complex to promote C–H bond breaking, and that a ligand with a σ-donating character comparable to that of water (H_2S) leaves it virtually unchanged. It is therefore reasonable to expect that a ligand with no σ-donor character might be able to revert the trend in reactivity observed above and yield an even higher reactivity than that obtained with all-water ligands.

For this reason we studied the compound $[FeO(H_2O)_4(BF_3)]^{2+}$, where, as before, the electron-deficient BF_3 ligand occupies the axial position. Although this species was found to be stable in the gas phase, we do not address here the issue of its stability either with respect to $[FeO(H_2O)_5]^{2+}$ or as a solvated species. The BF_3 molecule coordinates to the metal centre through one of the fluorine atoms with a Fe–F–B angle of 141.1°. The $3\sigma^{*\uparrow}$ orbital (Figure 6.5) exhibits a nodal structure analogous to the one observed in $[FeO(H_2O)_5]^{2+}$, with one of the B–F bonding orbitals of BF_3 replacing the σ lone pair of H_2O, and its energy is 0.51 eV lower than in the latter species. For this system we computed a C–H dissociation barrier of only 7 kJ/mol, which is consistent with the large $3\sigma^{*\uparrow}$ stabilization.

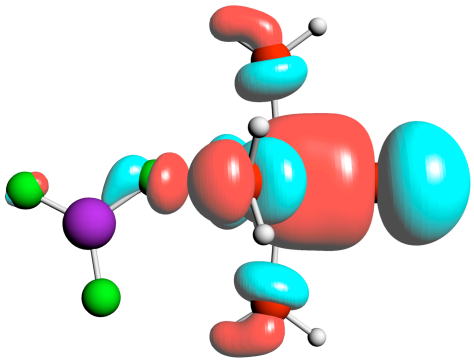

Figure 6.5 *$3\sigma^{*\uparrow}$ orbital in $[FeO(H_2O)_4(BF_3)]^{2+}$. The BF_3 molecule, axially coordinated to $Fe^{IV}O^{2+}$, is at the left-hand side of the figure. Note that the C_3 axis of the BF_3 ligand is not perpendicular to the z axis, and one of the B–F bonds is roughly oriented toward the metal centre.*

Finally, we consider a hypothetical $[FeO(H_2O)_4(o)]^{2+}$ complex in which the axial ligand is removed, and the O–Fe–O angles (where O stands for the oxygen atoms of the remaining ligands) are constrained to their values as in $[FeO(H_2O)_5]^{2+}$. Owing to the absence of an antibonding combination with orbitals of the axial ligand, the energy of the $3\sigma^{*\uparrow}$ orbital is further lowered compared to the BF_3 complex to 1.16 eV below its value in $[FeO(H_2O)_5]^{2+}$. The C–H bond cleavage occurs with virtually no barrier, the activation energy being lower than 1 kJ/mol. In the reactant complex, the donor orbital of CH_4 carries a substantial $3\sigma^{*\uparrow}$ character (34%, versus 53% e_z character), which is roughly three times as much as in the $[FeO(H_2O)_5]^{2+} + CH_4$ complex.

In Figure 6.6 we show activation barriers as a function of the percentage σ lone pair character of the axial ligand (or the e_1 orbital in the case of BF_3) in the $3\sigma^{*\uparrow}$ orbital. The latter quantity can be taken as measure of the overall "push" (or destabilization) experienced by the $3\sigma^{*\uparrow}$ orbital because of the presence of a σ-donating ligand. For the $S = 2$ complexes considered in this work, this quantity varies from 0 (for $[FeO(H_2O)_4(o)]^{2+}$) to 4.95% (for $[FeO(H_2O)_4(NH_3)]^{2+}$), and the C–H activation barriers are shown here to depend on it linearly (with a correlation coefficient ~0.98).

It is interesting to observe that Rohde and Que[105] have found that the axial NCMe ligand in $[FeO(TMC)(L_{ax})]^{2+}$ leads to lower reactivity than the axial carboxylate ligand CF_3COO^-. These are low-spin complexes due to the equatorial nitrogen donor coordination by the TMC ligand, and the carboxylate substitution may, as suggested by the authors, lead to relative stabilization of the high-spin $S = 2$ state, so that the latter becomes more easily accessible (possibly along the reaction path, in a two-state reactivity process). We do indeed find the difference between the $S = 1$ ground state and the $S = 2$ state in **1c** to be very small (BLYP) or vanishing (OPBE). However, we should note that the experimental observation corresponds to the expected effect of a weaker ligand field from the carboxylate than from the NCMe ligand, leading to reduced destabilization of the $3\sigma^{*\uparrow}$. Overall, the activation effect observed in Ref. 105

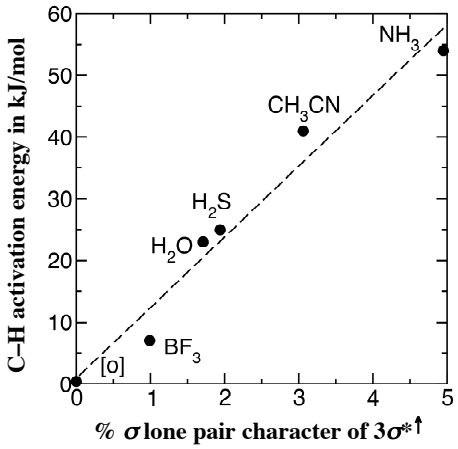

Figure 6.6 *C–H bond cleavage energy barrier as a function of percentage σ lone pair contribution to the $3\sigma^{*\uparrow}$ orbital in isolated $[FeO(H_2O)_4(L_{ax})]^{2+}$ complexes. The nature of L_{ax} is indicated, and "[o]" represents the complex with removed axial ligand. The dashed line (with slope 11.47 kJ/mol and intercept at 0.89 kJ/mol) has been obtained by linear regression from the calculated values.*

is therefore fully consistent with the molecular orbital model of reactivity described here.

For porphyrin-based compounds the inverse effect has been reported.[187] However, in these systems the $3\sigma^{*\uparrow}$ orbital seems to play no role, and, therefore, this effect is unrelated to the effect we report here for high-spin compounds. We note that the porphyrin systems are much less reactive than the systems we discuss.

6.4. Conclusions

We have highlighted the electronic structure features explaining the extraordinary reactivity of the $Fe^{IV}O^{2+}$ group in the oxidation of aliphatic C–H bonds: (a) a very low-lying acceptor orbital interacts with the C–H bonding orbital which acts as a donor; (b) in high-spin complexes, the energy of the $3\sigma^{*\uparrow}$ acceptor orbital is lowered by the exchange field of the excess ↑ spin electrons, leading to enhanced reactivity.

The empty $3\sigma^{*\uparrow}$ ($3d_{z^2}$–$2p_z$) orbital is the most important acceptor orbital, being low-lying and having a large amplitude at the oxo ligand. We have detailed that the nonbonding electrons in the d_δ orbitals $3d_{x^2-y^2}$ and $3d_{xy}$ (perpendicular to the Fe–O axis) are not just spectator electrons. When a ligand-induced switching occurs from the unpaired spin electron configuration $(3d_{x^2-y^2}{}^{\uparrow})^1(3d_{xy}{}^{\uparrow})^1$ to the spin-paired configuration $(3d_{xy})^2$, the lowering of the spin multiplicity from $S = 2$ to $S = 1$ makes the exchange field of the unpaired spin up electrons considerably less stabilizing, and the empty $3\sigma^{*\uparrow}$ shifts up. It then less readily accepts electrons from the C–H bonding orbital, hence the low-spin state $S = 1$ will yield a higher activation energy in the hydrogen abstraction step.

The spin state is determined by the ligand environment, in particular by the equatorial ligand field acting on the $d_{x^2-y^2}$ orbital. We analyzed a series of compounds of composition $[FeO(L_{eq})_4(L_{ax})]^{2+}$ derived from $[FeO(H_2O)_5]^{2+}$ ($S = 2$) by substitution of water with ligands with enhanced or decreased σ donor capability. For all complexes, there are two possible ground states of different spin multiplicity (quintet or triplet) lying close in energy. The quintet ground state was found to be more stable for $[FeO(H_2O)_5]^{2+}$ and all the systems in which only the axial water molecule is replaced. The triplet ground state is favored by stronger σ-donating ligands (e.g. $L_{eq} = NH_3$). These ligands push the $3d_{x^2-y^2}{}^{\uparrow}$ up, so that it becomes favorable for it to shed its electron into the originally empty $3d_{xy}{}^{\downarrow}$ orbital, where it can pair up with the electron in the $3d_{xy}{}^{\uparrow}$.

Whereas the equatorial ligands have the most important effect, determining the spin state, the *axial* ligand (trans to the oxo ligand) directly interacts with the crucial acceptor orbital $3\sigma^{*\uparrow}$ and affects its energy and shape. Therefore, the catalytic properties can be fine-tuned by varying the σ donor properties of the axial ligand alone. Changes in the orbital energy of ~1 eV or less may result in variations of up to 100 kJ/mol in the C–H bond cleavage activation barrier. We also proved that axial ligands with decreased σ donor ability enhance the catalytic properties of $[FeO(H_2O)_5]^{2+}$-derived systems by decreasing the energy of the $3\sigma^{*\uparrow}$ orbital and favoring its overlap with a suitable donor orbital of the substrate. We also proved the existence of a linear relation between the magnitude of the mixing between $3\sigma^{*\uparrow}$ and the axial ligand orbital responsible for its destabilization. The effect of the axial ligand can be optimally tuned by modifying its σ donor properties. In the absence of σ donation (as in the hypothetical $[FeO(H_2O)_4(o)]^{2+}$ + CH_4 system), the C–H bond cleavage process occurs almost spontaneously.

In summary, optimal electronic properties for C–H bond activation and hydroxylation require a high-spin state, which is favored by equatorial ligands with a weak ligand field, such as H_2O. A weak axial ligand field is similarly favorable, once the high-spin state is stabilized by a suitable equatorial field. These findings are consistent with the high catalytic activity of non-heme enzymes with flexible ligand environments and oxygen donor ligands rather than nitrogen lone pairs, such as TauD. The 2-His-1-carboxylate facial triad in the active site of the latter system consists of an equatorial ligand set with only one nitrogen donor, the other equatorial ligands being oxygen based (e.g. H_2O). The remaining histidine ligand coordinates the metal centre through a nitrogen donor in the axial site, a situation that is, according to our analysis, not optimal. A carboxylate ligand instead of a nitrogen donor in the axial position would in principle be more favorable, which is also in accordance with the results of Ref. 105. The insights gained in this work may be helpful in devising catalytic species for homogeneous alkane hydroxylation with superior activation properties, as well as in understanding the mechanistic role of oxidation intermediates containing high-valent metal centers with $[FeO(H_2O)_5]^{2+}$-like coordination and supported by a protective framework, such as zeolites[139] or oxygenated EDTA/Fe complexes in aqueous solution.[192-194]

Appendix A:

Orbital mixings in FeO^{2+}–substrate interactions

In Chapter 5, we propose a model for the reactivity of FeO^{2+} based on the relative energies of the LUMO of FeO^{2+} and the HOMOs of incoming molecules. Chapter 5 is provided with simplified schematic orbital diagrams of the interactions of $[FeO(H_2O)_5]^{2+}$ with methane, methanol, and water. In this Appendix, the complete orbital interaction diagrams for these interactions (Figure A1-A4) and tables with the mixings of all interacting orbitals (Table A1-A4) are given.

The orbitals of $[FeO(H_2O)_5]^{2+}$ and of the substrate molecules are depicted in Figure 5.4 and Figure 5.6.

In the orbital interaction diagrams (Figure A1-A4), the energy levels of the fragments in the geometry of the interacting complex plus the energy levels of the resulting molecular orbitals are given, showing the orbital mixing resulting from our fragment analysis. For the $[FeO(H_2O)_5]^{2+}$ fragment the levels of the *spin-restricted* orbitals are drawn, for technical reasons explained in Section 5.2. For the incoming molecule the shift of the orbitals caused by the net charge of the complex is also depicted. In the middle two columns of the diagrams the levels of the resulting *unrestricted* molecular orbitals are drawn.

For clarity, the energy levels mainly associated with the FeO^{2+} moiety itself are drawn in black; levels mainly associated with the water molecules of the first solvation shell (see also Table 2 of Ref. 16) are drawn in grey. Note that all grey levels are implicitly filled with electrons, though not depicted.

For the connecting lines different styles have been used: For levels that are not mixed between the two fragments the connecting lines are dashed grey. These levels are relatively unperturbed by the interaction with the other fragment. For occupied levels that are interacting (Pauli repulsion) the connecting lines are dashed black. Finally, for interactions of occupied orbitals with unoccupied orbitals, i.e. interactions that contribute to the bonding interaction, the connecting lines are solid black.

In the corresponding tables (Table A1-A4) mixing percentages of the orbitals are given. In these tables, the orbitals that contribute to the bonding interaction (interactions of the HOMOs of the incoming molecules with the LUMO of $[FeO(H_2O)_5]^{2+}$) are presented in bold. For each interacting orbital (through Pauli repulsion or charge transfer), percentages are given for the contribution of $[FeO(H_2O)_5]^{2+}$ orbitals and of orbitals of the incoming molecule. Values labeled "empty" represent relative contributions from empty fragment orbitals. Note that added to an orbital name, the label "empty" means that the molecular orbital is empty.

For the precise interpretation of the FeO^{2+} orbital contributions to the molecular orbitals, we performed an additional fragment analysis in which the $[FeO(H_2O)_5]^{2+}$ fragment was partitioned into a FeO^{2+} and 5 water fragments. This was done because

there is substantial spurious mixing of the $[FeO(H_2O)_5]^{2+}$ orbitals during complexation, caused by changing first-shell water contributions. In the fourth and fifth columns of the tables the resulting contributions of FeO^{2+} orbitals and of water orbitals are given. Note that occasional mixing of the 2σ and the $3\sigma^*$ orbitals is an effect of the axial water ligand and is not caused by the interaction with the incoming molecule.

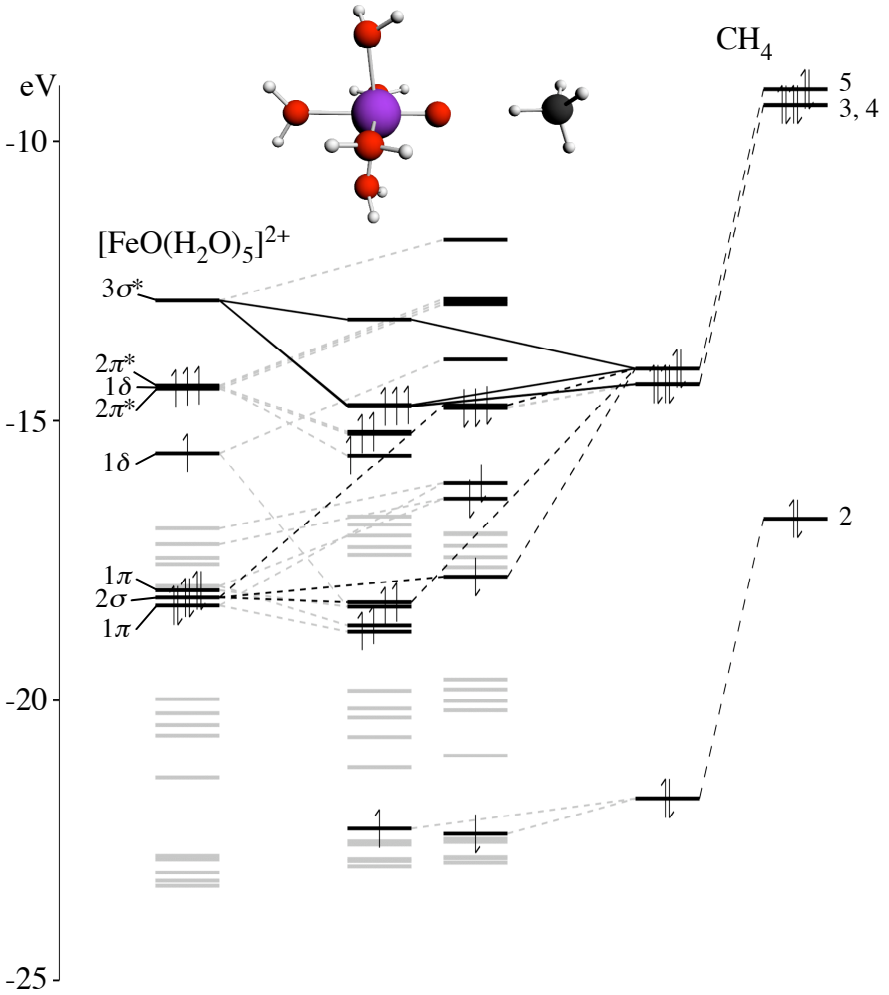

Figure A1 *Orbital interaction diagram for the interaction of* $[FeO(H_2O)_5]^{2+}$ *with methane.*

Table A1 *Orbital mixings for the interaction of $[FeO(H_2O)_5]^{2+}$ with methane.*

Orbital	Energy (eV)	% $[FeO(H_2O)_5]^{2+}$ character	Interacting FeO^{2+} orbitals	% First-shell water orbitals	% CH_4 character	CH_4 orbitals
49 ↑ (empty)	**-13.19**	**89% (86% empty)**	**3σ* (72%)**	**16%**	**11%**	**5 (11%)**
48 ↑	**-14.72**	**12% (9% empty)**	**3σ* (6%)**	**4%**	**88%**	**5 (66%)**
			2σ (2%)			**3 (21%)**
						4 (1%)
47 ↑	**-14.74**	**3% (2% empty)**	**3σ* (1%)**	**1%**	**97%**	**4 (63%)**
						3 (23%)
						5 (11%)
46 ↑	**-14.75**	**2% (1% empty)**	**3σ* (1%)**	**1%**	**98%**	**3 (54%)**
						4 (34%)
						5 (9%)
37 ↑	-18.25	98% (0% empty)	2σ (64%)	34%	2%	5 (2%)
44 ↓	-14.72	7% (1% empty)	2σ (6%)	0%	93%	5 (92%)
						3 (1%)
34 ↓	-17.79	95% (1% empty)	2σ (76%)	14%	5%	5 (5%)
			3σ* (5%)			

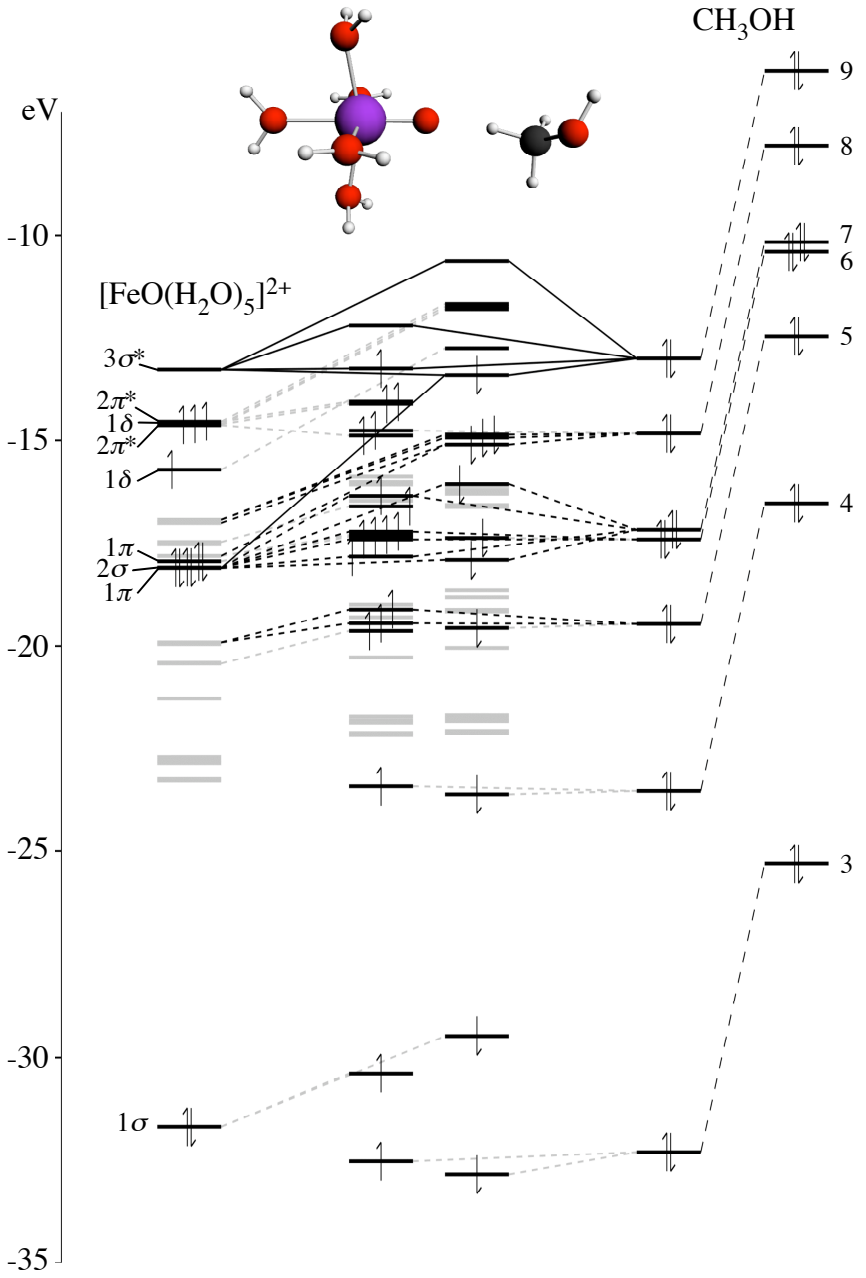

Figure A2 *Orbital interaction diagram for the interaction of* $[FeO(H_2O)_5]^{2+}$ *with methanol interacting via its C–H bond.*

Table A2 *Orbital mixings for the interaction of $[FeO(H_2O)_5]^{2+}$ with methanol interacting via its C–H bond.*

Orbital	Energy (eV)	% $[FeO(H_2O)_5]^{2+}$ character	Interacting FeO^{2+} orbitals	% First-shell water orbitals	% CH_3OH character	CH_3OH orbitals
53 ↑ (empty)	**-12.20**	**55% (50% empty)**	**3σ* (45%) 2σ (2%)**	**9%**	**45%**	**9 (43%) 7 (2%)**
52 ↑	**-13.25**	**47% (46% empty)**	**3σ* (35%)**	**12%**	**53%**	**9 (53%)**
44 ↑	-16.35	48% (3% empty)	2σ (32%)	16%	52%	7 (48%) 9 (2%) 6 (1%)
41 ↑	-17.22	7% (0% empty)	1π (4%) 2σ (1%)	2%	93%	6 (85%) 7 (8%) 8 (1%)
38 ↑	-17.41	96% (0% empty)	1π (71%)	25%	4%	6 (3%) 7 (1%)
37 ↑	-17.82	55% (0% empty)	2σ (29%)	26%	45%	7 (35%) 6 (8%) 5 (2%)
35 ↑	-19.11	91% (0% empty)	2σ (21%)	70%	9%	5 (7%) 7 (1%)
33 ↑	-19.45	12% (0% empty)	2σ (4%)	8%	88%	5 (87%)
53 ↓ (empty)	**-10.63**	**98% (97% empty)**	**3σ* (80%)**	**18%**	**2%**	**9 (1%)**
48 ↓	**-13.41**	**10% (1% empty)**	**2σ (8%)**	**2%**	**90%**	**9 (88%) 7 (2%)**
47 ↓	-14.86	38% (0% empty)	1π (31%)	7%	62%	8 (60%) 6 (1%)
46 ↓	-14.93	64% (0% empty)	1π (50%)	14%	36%	8 (36%)
45 ↓	-15.10	97% (0% empty)	1π (83%)	14%	3%	8 (3%)
44 ↓	-16.06	70% (0% empty)	2σ (55%)	14%	30%	7 (19%) 9 (9%) 6 (2%)
37 ↓	-17.91	28% (1% empty)	2σ (16%) 3σ* (3%)	6%	72%	7 (64%) 6 (6%) 5 (2%)

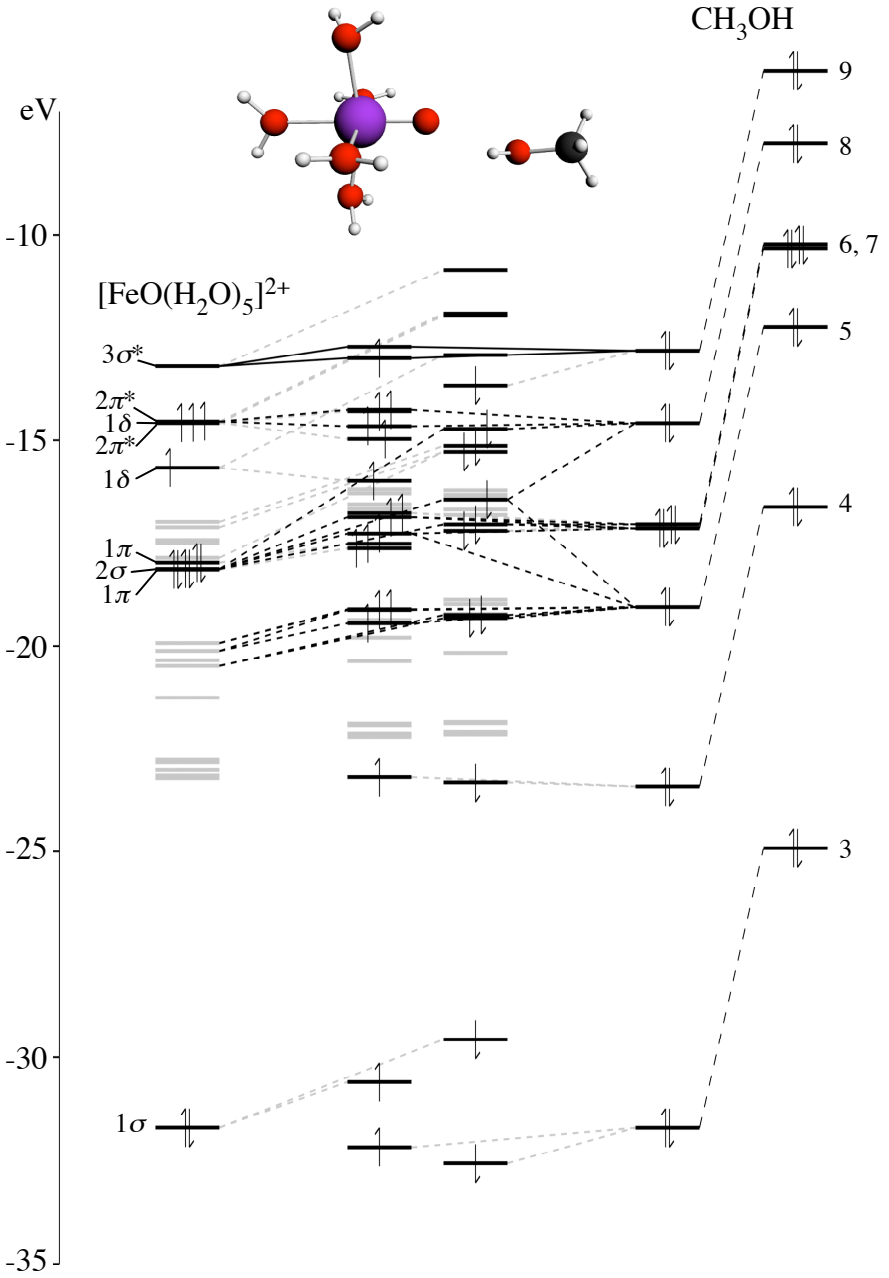

Figure A3 *Orbital interaction diagram for the interaction of* $[FeO(H_2O)_5]^{2+}$ *with methanol interacting via its O–H bond.*

Table A3 *Orbital mixings for the interaction of $[FeO(H_2O)_5]^{2+}$ with methanol interacting via its O–H bond.*

Orbital	Energy (eV)	% $[FeO(H_2O)_5]^{2+}$ character	Interacting FeO^{2+} orbitals	% First-shell water orbitals	% CH_3OH character	CH_3OH orbitals
53 ↑ (empty)	**-12.72**	**57% (55% empty)**	**3σ* (47%)**	**10%**	**43%**	**9 (42%)**
52 ↑	**-13.00**	**42% (42% empty)**	**3σ* (33%)**	**9%**	**58%**	**9 (57%)**
						6 (1%)
51 ↑	-14.26	92% (0% empty)	2π* (87%)	5%	8%	8 (7%)
49 ↑	-14.66	10% (1% empty)	2π* (8%)	2%	90%	8 (87%)
						7 (2%)
						6 (1%)
41 ↑	-16.87	7% (0% empty)	2σ (4%)	3%	93%	7 (58%)
						6 (32%)
						8 (3%)
40 ↑	-17.27	87% (1% empty)	2σ (65%)	23%	13%	6 (7%)
						5 (5%)
						7 (1%)
36 ↑	-19.10	62% (0% empty)	–	62%	38%	5 (37%)
35 ↑	-19.12	58% (0% empty)	–	58%	42%	5 (42%)
33 ↑	-19.45	88% (0% empty)	2σ (21%)	67%	12%	5 (12%)
47 ↓	-14.72	6% (0% empty)	1π (3%)	1%	94%	8 (90%)
			2σ (2%)			7 (3%)
						6 (1%)
41 ↓	-16.44	95% (0% empty)	2σ (41%)	55%	5%	5 (2%)
						6 (2%)
						8 (1%)
38 ↓	-17.05	3% (0% empty)	2σ (2%)	1%	97%	7 (66%)
						6 (26%)
						8 (3%)
						5 (1%)
33 ↓	-19.24	43% (0% empty)	–	43%	57%	5 (57%)
32 ↓	-19.32	65% (0% empty)	2σ (5%)	60%	35%	5 (35%)

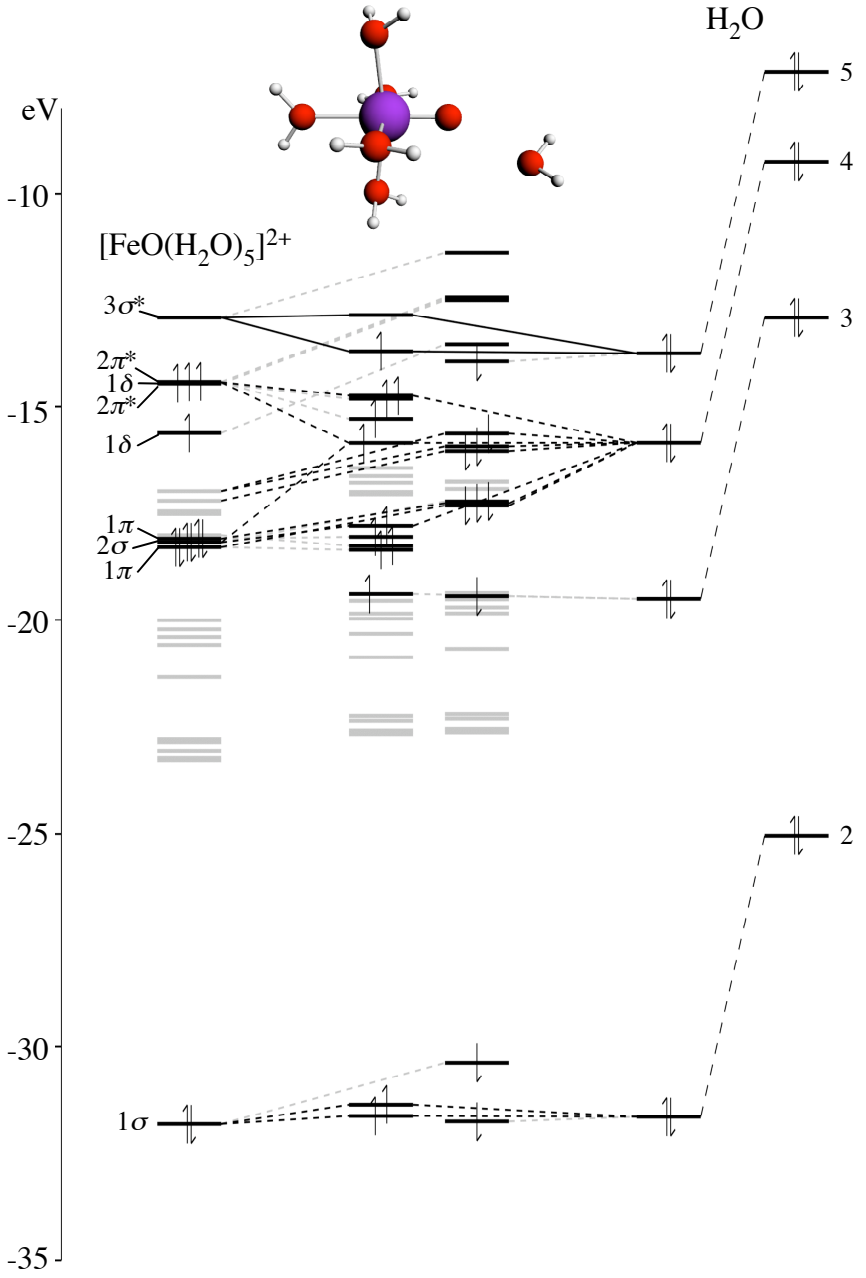

Figure A4 *Orbital interaction diagram for the interaction of* $[FeO(H_2O)_5]^{2+}$ *with water.*

Table A4 *Orbital mixings for the interaction of $[FeO(H_2O)_5]^{2+}$ with water.*

Orbital	Energy (eV)	% $[FeO(H_2O)_5]^{2+}$ character	Interacting FeO^{2+} orbitals	% First-shell water orbitals	% H_2O character	H_2O orbitals
49 ↑ (empty)	**-12.85**	**87% (85% empty)**	**3σ* (71%)**	**16%**	**13%**	**5 (13%)**
48 ↑	**-13.70**	**15% (14% empty)**	**3σ* (10%)**	**5%**	**85%**	**5 (85%)**
47 ↑	-14.74	94% (0% empty)	2π* (90%)	4%	6%	4 (5%) 5 (1%)
44 ↑	-15.85	8% (1% empty)	2π* (5%)	3%	92%	4 (92%)
38 ↑	-17.80	98% (1% empty)	2σ (72%)	26%	2%	4 (2%) 5 (1%)
23 ↑	-31.36	90% (0% empty)	1σ (89%)	0%	10%	2 (10%)
22 ↑	-31.62	10% (0% empty)	1σ (10%)	0%	90%	2 (90%)
43 ↓	-15.63	61% (0% empty)	1π (46%) 2σ (1%)	13%	39%	4 (39%)
42 ↓	-15.93	61% (0% empty)	1π (39%) 2σ (3%)	19%	39%	4 (39%)
41 ↓	-16.04	84% (0% empty)	1π (64%) 2σ (1%)	19%	16%	4 (16%)
36 ↓	-17.26	97% (1% empty)	2σ (24%) 1π (6%)	67%	3%	4 (3%)
35 ↓	-17.32	98% (1% empty)	2σ (15%) 1π (7%)	76%	2%	4 (2%)

Summary

In this thesis, several reactions and reactants that take part in the Fenton reaction have been studied using theoretical calculations, namely DFT calculations and Car-Parrinello simulations. The Fenton reaction is a very elegant and environmentally friendly way to oxidize organic substances using Fe^{2+} ions and hydrogen peroxide (H_2O_2) in water, and has been known since the late 19th century. However, the mechanism by which the Fenton reaction occurs is not completely known, and there has been a long-lasting debate on the subject.

Fenton's reagent is a rather strong but unspecific oxidation catalyst, and its main use is found in the oxidation of wastewater, besides several other industrial applications. Increased knowledge of the mechanism of the Fenton reaction may open the way to development of more specific catalysts based on Fenton's reagent, that share its advantages (being strong and environmentally friendly).

In Chapter 1, we have discussed the debate on the mechanism of the Fenton reaction, which is focused on whether the active intermediate is $OH^{\bullet}$ or FeO^{2+}. In this discussion, usually also other oxidants than H_2O_2 (like HOCl, ROOH, and ROOR) and other solvents than water are incorporated, assuming identical chemistry in all these cases. We have pointed out, though, that most probably the mechanism is different in different systems and may depend on the nature of reactants, the concentration of reactants, the solvent, presence of molecular oxygen, presence of light, and other variables. These variables determine whether the reactive intermediate is $OH^{\bullet}$, FeO^{2+}, or perhaps both. For the system with Fe^{2+} and hydrogen peroxide in water, simulations of Ensing et al. have shown that FeO^{2+} is the active intermediate and $OH^{\bullet}$ is formed only very shortly and not as a free reactant.

In this thesis, we have studied (1) the behavior of an $OH^{\bullet}$ radical in water and whether or not it can diffuse via a Grotthuss diffusion mechanism; (2) the mechanism of the reaction of FeO^{2+} with methanol in water; (3) the influence of water on the reactivity of FeO^{2+}; and (4) the influence of ligands on the reactivity of FeO^{2+}, focusing on the different effects of equatorial and axial ligands.

Before going into the calculations themselves, we have discussed some technical aspects for the simulations in Chapter 2. Firstly, we have discussed the Car-Parrinello method and a recent debate on what should be the best values for the fictitious mass and the timestep in this method. We have shown that it is better to use a much smaller fictitious mass than commonly used and that nevertheless a large timestep can be used. Secondly, we have discussed the Projector Augmented Wave (PAW) method, which we have used in order to obtain an efficient description of the iron ions. The theory *and* the weaknesses of this method are shortly explained, and we have optimized sets of PAW projectors such as to obtain acceptable results for our type of systems. Thirdly, we have given a derivation of the virial equation for calculating the pressure in molecular simulations. We have shown that this equation does not hold in extended systems when non-pair-additive models are used. Sadly, this means that we have not been able to monitor the pressure in our simulations.

Summary

In Chapter 3, the behavior of $OH^{\bullet}$ radicals in water solution has been studied. We have found that, when the BLYP functional is used, $OH^{\bullet}$ makes an O–O hemibond with one of the surrounding waters. This hemibond occupies the unpaired electron of $OH^{\bullet}$ and blocks H atom transfer from surrounding water molecules, making rapid diffusion of $OH^{\bullet}$ via a Grotthuss mechanism unlikely. Although the abundance of the hemibond is believed to be overestimated by the BLYP functional, simulations with corrected models confirm that no hydrogen bonds are formed with the unpaired electron and only very slow Grotthuss diffusion has been observed for the $OH^{\bullet}$ radical.

In Chapters 4, 5, and 6 we have studied the FeO^{2+} species. In Chapter 4, the oxidation of methanol to formaldehyde by $[FeO(H_2O)_5]^{2+}$ has been studied, using both gas phase calculations and simulations in water. We have found that FeO^{2+} attacks specifically at the C–H bond abstracting an $H^{\bullet}$ atom. Subsequently, the OH hydrogen of methanol transfers to the iron complex spontaneously, completing the reaction. Interestingly, in the gas phase the barrier for the first hydrogen abstraction is only a mere 2 kJ/mol, while in solution a free energy barrier of 50 kJ/mol (upper bound) was found. Such a difference was also found before for the oxidation of methane to methanol.

In Chapter 5, the unexpectedly large solvation effects on hydrogen abstraction by FeO^{2+} were further studied by way of an electronic structure analysis. FeO^{2+} turns out to be extremely electrophilic because of a very low-lying $3\sigma^{*\uparrow}$ LUMO. C–H bonding orbitals are slightly higher in energy than this $3\sigma^{*\uparrow}$ LUMO of FeO^{2+}, which causes a large charge donation activating the C–H bond. In water solution, however, the orbitals shift upwards in energy and the difference between the FeO^{2+} and C–H orbitals changes, diminishing the all important charge transfer interaction. This is a very unusual type of solvent effect that opens a way to control the reactivity of FeO^{2+}.

In Chapter 6, we have continued the investigation of how the reactivity of FeO^{2+} complexes can be controlled via their $3\sigma^{*\uparrow}$ orbitals. In this chapter the effect of ligands was investigated and explained by their effect on the $3\sigma^{*\uparrow}$ orbital. We have stressed that the $3\sigma^{*\uparrow}$ orbital is only the important orbital when the system is in a high spin state, which is favored when the equatorial ligands are only weakly σ-donating. Once the high spin ($S = 2$) is guaranteed by a judicious choice of the equatorial ligands, the reactivity can be further controlled by varying the *axial* ligand. Strong σ-donating ligands on the axial position destabilize the $3\sigma^{*\uparrow}$ and decrease its reactivity. Weak σ-donating ligands or an empty place increase the reactivity. Thus, a method has been found to control the reactivity of high-spin FeO^{2+} complexes, both via the solvent and the ligands. Hopefully, these results will accelerate the development of new catalysts based on FeO^{2+} complexes.

Samenvatting

Dit proefschrift behandelt theoretisch onderzoek aan verscheidene reacties en reactanten uit de Fenton reactie, uitgevoerd door middel van DFT berekeningen en Car-Parrinello simulaties. De Fenton reactie is een zeer elegante en milieuvriendelijke manier om organische stoffen te oxideren met behulp van Fe^{2+} (ijzer) ionen en watestofperoxide (H_2O_2) in water. Alhoewel deze reactie al bekend is sinds het einde van de 19e eeuw, is het mechanisme van de reactie nog steeds niet geheel bekend. Over dit mechanisme is derhalve al zeer lang een heftig debat gaande.

Fenton's reagens is een tamelijk krachtige maar onspecifieke oxidatie-katalysator, die voornamelijk wordt toegepast voor het zuiveren van afvalstromen, naast verscheidene andere industriële toepassingen. Verbeterde kennis van het mechanisme van de Fenton reactie zal wellicht de deur openen voor de ontwikkeling van nieuwe katalysatoren die gebaseerd zijn op Fenton's reagens. Nieuwe katalysatoren die eveneens krachtig en milieuvriendelijk zijn maar hopelijk ook geschikt voor meer specifieke oxidaties.

In Hoofdstuk 1 bespreken we de discussie over het mechanisme van de Fenton reactie. Deze discussie is altijd erg gefocusseerd geweest op de vraag of het actieve deeltje nu $OH^{\bullet}$ is of FeO^{2+}. Daarbij zijn vaak ook andere oxidanten dan H_2O_2 (zoals HOCl, ROOH en ROOR) en andere oplosmiddelen dan water meegenomen in de discussie, ervan uitgaande dat de chemie gelijk zou zijn voor al deze systemen. Wij benadrukken echter dat het mechanisme hoogstwaarschijnlijk verschillend is in verschillende systemen en dat het mechanisme af zou kunnen hangen van vele variabelen, zoals de gebruikte reactanten én hun concentraties, het oplosmiddel, de aanwezigheid van zuurstof, de aanwezigheid van licht en nog andere variabelen. Hierdoor wordt uiteindelijk bepaald of het actieve deeltje in de reactie nu $OH^{\bullet}$ is of FeO^{2+}, of in sommige gevallen wellicht beide. Voor het mengsel van Fe^{2+} en waterstofperoxide in water hebben simulaties van Ensing en anderen aangetoond dat het actieve deeltje FeO^{2+} is en dat $OH^{\bullet}$ slechts voor zeer korte tijd wordt gevormd en gebonden blijft aan het reactieve centrum.

In ons onderzoek hebben we (1) het gedrag van $OH^{\bullet}$ in water bestudeerd en met name of $OH^{\bullet}$ kan diffunderen via een Grotthuss diffusie mechanisme; (2) het mechanisme van de reactie van FeO^{2+} met methanol; (3) het effect van water op de reactiviteit van FeO^{2+} en (4) het effect van liganden op de reactiviteit van FeO^{2+}, waarbij het laatste vooral gericht is op de verschillende effecten van equatoriale en axiale liganden.

Voorafgaand aan de berekeningen worden enkele technische aspecten voor de simulaties besproken in Hoofdstuk 2. Ten eerste bespreken we de Car-Parrinello methode en een recent debat over de optimale waarden voor de fictieve massa en de tijdstap in deze methode. We tonen aan dat lagere waarden dan gebruikelijk voor de fictieve massa betere resultaten geven en dat desondanks grote tijdstappen gebruikt kunnen worden. Ten tweede bespreken we de Projector Augmented wave (PAW) methode, nodig voor een goede beschrijving van de ijzer ionen. We leggen kort de

theorie én de zwakke kanten van deze methode uit en we introduceren nieuwe sets van PAW projectoren die we hebben geoptimaliseerd om acceptabele resultaten te geven voor ons type systemen. Tenslotte geven we een afleiding voor de viriaal formule die gebruikt wordt om de druk te berekenen in moleculaire simulaties. We laten daarbij zien dat deze formule niet geschikt is voor "extended" systemen in combinatie met niet paar-additieve modellen. Helaas betekent dit dat we de druk in onze simulaties niet hebben kunnen controleren.

Hoofdstuk 3 behandelt het gedrag van $OH^{\bullet}$ radicalen in waterige oplossing. We hebben ontdekt dat –tenminste wanneer de BLYP functionaal wordt gebruikt voor de simulaties– het $OH^{\bullet}$ radicaal een zuurstof–zuurstof "drie-elektron-binding" vormt met een van de omringende water moleculen. Deze drie-elektron-binding houdt het ongepaarde elektron van het $OH^{\bullet}$ bezet en blokkeert daardoor de afgifte van waterstof atomen van omringende water moleculen aan het $OH^{\bullet}$ radicaal. Hierdoor wordt versnelde diffusie van $OH^{\bullet}$ radicalen door middel van een Grotthuss mechanisme onmogelijk gemaakt.

Alhoewel het overheersende karakter van de drie-elektron-binding waarschijnllijk wordt overschat door de BLYP functionaal, bevestigen simulaties met gecorrigeerde modellen dat er geen waterstof bruggen worden gevormd met het ongepaarde elektron en dat er slechts zeer trage Grotthuss diffusie optreedt bij $OH^{\bullet}$ radicalen.

In de Hoofdstukken 4, 5 en 6 hebben we tenslotte de FeO^{2+} complexen bestudeerd. Hoofdstuk 4 behandelt de oxidatie van methanol naar formaldehyde door $[FeO(H_2O)_5]^{2+}$, zowel in de gasfase als in waterige oplossing. We hebben hierbij ontdekt dat FeO^{2+} specifiek op de C–H binding aanvalt en een $H^{\bullet}$ atoom abstraheert. Vervolgens verloopt de rest van de reactie spontaan waarbij het OH waterstof atoom van methanol ook naar het ijzer complex overstapt. Opvallend genoeg is de reactiebarrière in de gasfase slechts 2 kJ/mol, terwijl in oplossing een vrije energie barrière van 50 kJ/mol werd gevonden. Een dergelijk groot oplosmiddel effect was eerder ook al gevonden voor de oxidatie van methaan naar methanol.

In Hoofdstuk 5 is dit opvallende oplosmiddel effect verder bestudeerd door middel van een elektronenstructuur analyse. Het blijkt dat FeO^{2+} extreem electrofiel is vanwege een zeer laag gelegen $3\sigma^{*\uparrow}$ LUMO. Doordat C–H bindingen enigszins hoger in energie zijn dan deze $3\sigma^{*\uparrow}$ LUMO van FeO^{2+}, treedt er een grote ladingsdonatie op vanuit de C–H binding waardoor de C–H binding geactiveerd wordt. In waterige oplossing echter, verschuiven de orbitalen omhoog in energie en verandert het verschil tussen de FeO^{2+} en C–H orbitalen. Hierdoor verandert het karakter van de interactie en wordt het grote oplosmiddel effect verklaard. Dit type oplosmiddel effect is zeer ongebruikelijk en opent mogelijkheden om de reactiviteit van FeO^{2+} te beïnvloeden.

In Hoofdstuk 6 hebben we verder onderzocht hoe de reactiviteit van FeO^{2+} complexen kan worden beïnvloed via de $3\sigma^{*\uparrow}$ orbitaal. In dit hoofdstuk is het effect van liganden onderzocht en verklaard door hun effect op de $3\sigma^{*\uparrow}$ orbitaal. We benadrukken dat de $3\sigma^{*\uparrow}$ orbitaal alleen de bepalende orbitaal is wanneer het systeem in een hoge spin toestand is, en die wordt bereikt wanneer de equatoriale liganden

slechts zwakke σ-donerende eigenschappen hebben. Als eenmaal een hoge spin (S = 2) is gewaarborgd door een juiste keuze van equatoriale liganden kan de reactiviteit worden geregeld door het axiale ligand te variëren. Hierbij zorgen sterk σ-donerende liganden op de axiale positie voor een destabilisatie van de $3\sigma^{*\uparrow}$ orbitaal en daardoor een verlaagde reactiviteit. Zwak σ-donerende liganden of een lege axiale positie daarentegen verhogen de reactiviteit van het FeO^{2+} complex. Zodoende hebben we dus een methode gevonden om de reactiviteit van S = 2 FeO^{2+} complexen te regelen, zowel door middel van oplosmiddelen als door middel van liganden. De hoop is dat hierdoor de ontwikkeling versneld zal worden van nieuwe industriële katalysatoren die gebaseerd zijn op FeO^{2+} complexen.

Dankwoord

Op dit punt gekomen, wil ik graag iedereen bedanken die dit proefschrift mede mogelijk heeft gemaakt.

Om te beginnen mijn promotor Evert Jan Baerends. Evert Jan, dankjewel dat je dit hele project mogelijk hebt gemaakt en mij daarin hebt begeleid. Ik heb onze samenwerking altijd als erg prettig ervaren en ik heb veel van je geleerd. Ik wil je bedanken dat je me altijd veel vrijheid hebt gegeven, zowel in het onderzoek als als leidinggevende in de periode dat ik overspannen was. Al met al had ik geen betere promotor kunnen wensen.

During this PhD project, I have cooperated with several people, whom I would like to thank as well: Peter Vassilev, you were my first roommate, with whom I discussed a lot of science. Our approach to science (equations versus interpretations) differed a little, but after all our combined effort only improved the results and we have produced some nice articles. So thanks for all that. Johannes Neugebauer, we have also produced some work together, although we worked in different projects. I think this was quite a fruitful cooperation and I must say I have always really enjoyed working with you! Leonardo Bernasconi, you were my next roommate after Peter left. You I want to especially thank for the cooperation that resulted in what is now Chapter 6 of this thesis. I view this as the crown of the thesis and without you this chapter would not exist. Thanks for performing this project even though you initially did not like it; I am really glad we did it. And finally: Carine Michel. Well, we did not really cooperate but you are following up in the same subject, so I simply want to wish you good luck with that.

Ook alle overige collega's en ex-collega's wil ik bedanken voor de goede tijd en vooral voor de enerverende lunch- en koffiepauzes. Ik zie er toch maar vanaf om jullie allemaal bij name te noemen, maar ik wens jullie allemaal het beste toe en heel veel succes!

Op deze plek wil ik ook Lisette Potze noemen: In eerste instantie gewoon een werkcollege studente maar gaande weg een gezellige vriendin die de saaie VU gebouwen een beetje opfleurde. Bedankt voor alle gezellige babbeltjes en natuurlijk de lekkere taartjes!

Tijdens de afgelopen jaren heb ik ook heel wat conferenties en winterscholen bezocht en daar opgetrokken met AIO's van andere theoretische chemie groepen, zoals Anna, Joost, Chretien, Bouke, Elske en anderen. Jullie allemaal bedankt voor de gezellige en interessante ontmoetingen. Ik wil jullie allemaal heel veel succes wensen in jullie verdere carrières. En vooral Joost, aangezien we de komende tijd opnieuw collega's zijn...

Ook Paul de Hoog uit Leiden wil ik bedanken. Het was leuk om jou te begeleiden in weer eens een heel ander project.

Tenslotte gaat mijn dank natuurlijk uit naar familie en vrienden. In eerste instantie naar mijn ouders, broer, zussen en zwagers. Alhoewel jullie weinig invloed hebben

gehad op het promotieonderzoek zelf, is familie altijd belangrijk voor steun op de achtergrond. Jullie zijn gewoon fijne familie en daar hoeft verder niets aan toegevoegd te worden.

Van mijn vrienden wil ik vooral Robert Jan bedanken. We zijn al vele jaren beste vrienden en delen ongeveer alles. Vooral tijdens de jaren van mijn promotieonderzoek heb ik behoorlijk wat werkstress en privé-stress over je heen gestort, dus heel erg bedankt voor alle steun in alles. Gelukkig hebben we in deze jaren ook veel mooie dingen mogen delen, zoals het vinden van twee zeer lieftallige dames, we zijn elkaars ceremoniemeesters geweest en we hopen binnenkort allebei vader te worden. Er komen waarschijnlijk dus nog wel genoeg andere stresssituaties om te delen...

En dan Netty, de eerdergenoemde lieftallige dame! Netty, van mijn promotieonderzoek heb je precies de zwaarste helft meegemaakt. Bedankt voor alle steun en geduld als ik weer eens uitgeput thuis kwam; ik beloof je dat ik niet nog eens aan een proefschrift zal beginnen. Ik hoop dat ons leven samen alleen maar steeds leuker zal worden en verder staat de volgende grote uitdaging gewoon alweer te wachten: het opvoeden van “Ukkie”.

Tenslotte wil ik God bedanken. Hij heeft mij gemaakt en de hersens gegeven om zijn schepping te kunnen bestuderen, dus Hem komt alle eer toe.

Publications

1. **Ab initio molecular dynamics simulation of the $OH^{\bullet}$ radical in liquid water**
   P. Vassilev, M. J. Louwerse, E. J. Baerends
   Chem. Phys. Lett. **398** (2004) 212-216.

2. **The merits of the frozen-density embedding scheme to model solvatochromic shifts**
   J. Neugebauer, M. J. Louwerse, E. J. Baerends, T. A. Wesolowski
   J. Chem. Phys. **122** (2005) 094115-1/13.

3. **Modeling solvent effects on electron-spin-resonance hyperfine couplings by frozen-density embedding**
   J. Neugebauer, M. J. Louwerse, P. Belanzoni, T. A. Wesolowski, E.J. Baerends
   J. Chem. Phys. **123** (2005) 114101-1/11.

4. **Hydroxyl radical and hydroxide ion in liquid water: A comparative electron density functional theory study**
   P. Vassilev M. J. Louwerse and E. J. Baerends
   J. Phys. Chem. B **109** (2005) 23605-23610.

5. **Calculation of pressure in case of periodic boundary conditions**
   M. J. Louwerse, E. J. Baerends
   Chem. Phys. Lett. **421** (2006) 138-141.

6. **Oxidative properties of FeO^{2+}: electronic structure and solvation effects**
   M. J. Louwerse, E. J. Baerends
   Phys. Chem. Chem. Phys. **9** (2007) 156-166.

7. **The role of equatorial and axial ligands in promoting the activity of non-heme oxidoiron(IV) catalysts in alkane hydroxylation**
   L. Bernasconi, M. J. Louwerse, E. J. Baerends
   Eur. J. Inorg. Chem. (2007) 3023-3033.

8. **Oxidation of methanol by FeO^{2+} in water: DFT calculations in the gas phase and ab initio simulations in water solution**
   M. J. Louwerse, P. Vassilev, E. J. Baerends
   J. Phys. Chem. B **112** (2008) 1000-1012.

9. **Influence of the copper coordination geometry on the DNA cleavage activity of Clip-Phen complexes studied by DFT**
P. de Hoog, M. J. Louwerse, P. Gamez, M. Pitié, E. J. Baerends, B. Meunier, J. Reedijk
Eur. J. Inorg. Chem. (2008) 612-619.

Bibliography

(1) Fenton, H. J. H. *Chem. News* **1876**, *33*, 190.
(2) Bishop, D. F.; Stern, G.; Fleischman, M.; Marshall, L. S. *Ind. Eng. Chem. Des. Dev.* **1968**, *7*, 110-117.
(3) Pérez, M.; Torrades, F.; García-Hortal, J. A.; Domènech, X.; Peral, J. *Appl. Catal. B: Environ.* **2002**, *36*, 63-74.
(4) Hage, J. P.; Llobet, A.; Sawyer, D. T. *Bioorganic Med. Chem.* **1995**, *3*, 1383-1388.
(5) Wardman, P.; Candeias, L. P. *Radiat. Res.* **1996**, *145*, 523-531.
(6) Dunford, H. B. *Coord. Chem. Rev.* **2002**, *233*, 311-318.
(7) Rush, J. D.; Koppenol, W. H. *J. Am. Chem. Soc.* **1988**, *110*, 4957-4963.
(8) Koppenol, W. H. *Redox Rep.* **2001**, *6*, 229-234.
(9) Groves, J. T. *J. Inorg. Biochem.* **2006**, *100*, 434-447.
(10) Gozzo, F. *J. Mol. Catal. A: Chem.* **2001**, *171*, 1-22.
(11) Hohenberg, P.; Kohn, W. *Phys. Rev.* **1964**, *136*, B864-B871.
(12) Kohn, W.; Sham, L. J. *Phys. Rev.* **1965**, *140*, A1133-A1138.
(13) Car, R.; Parrinello, M. *Phys. Rev. Lett.* **1985**, *55*, 2471-2474.
(14) Buda, F.; Ensing, B.; Gribnau, M. C. M.; Baerends, E. J. *Chem. Eur. J.* **2001**, *7*, 2775-2783.
(15) Ensing, B.; Buda, F.; Blöchl, P.; Baerends, E. J. *Angew. Chem., Int. Ed.* **2001**, *40*, 2893-2895.
(16) Ensing, B.; Buda, F.; Blöchl, P. E.; Baerends, E. J. *Phys. Chem. Chem. Phys.* **2002**, *4*, 3619-3627.
(17) Ensing, B.; Baerends, E. J. *J. Phys. Chem. A* **2002**, *106*, 7902-7910.
(18) Blöchl, P. *Phys. Rev. B* **1994**, *24*, 17953-17979.
(19) Blöchl, P.; Först, C. J.; Schimpl, J. *Bull. Mater. Sci.* **2003**, *26*, 33-41.
(20) Fenton, H. J. H. *J. Chem. Soc.* **1894**, *65*, 899-904.
(21) Haber, F.; Weiss, J. *Naturwiss.* **1932**, *51*, 948-950.
(22) Bray, W. C.; Gorin, M. H. *J. Am. Chem. Soc.* **1932**, *54*, 2124-2125.
(23) Barb, W. G.; Baxendale, J. H.; George, P.; Hargrave, K. R. *Trans. Faraday Soc.* **1951**, *47*, 462-500.
(24) Bray, W. C. *J. Am. Chem. Soc.* **1938**, *60*, 82-87.
(25) Baxendale, J. H.; Evans, M. G.; Park, G. S. *Trans. Faraday Soc.* **1946**, *42*, 155-169.
(26) Walling, C. *Acc. Chem. Res.* **1975**, *8*, 125-131.
(27) Halliwell, B.; Gutteridge, J. M. C. *FEBS Lett.* **1992**, *307*, 108-112.
(28) Goldstein, S.; Meyerstein, D.; Czapski, G. *Free Radical Biol. Med.* **1993**, *15*, 435-445.
(29) Sawyer, D. T.; Sobkowiak, A.; Matsushita, T. *Acc. Chem. Res.* **1996**, *29*, 409-416.
(30) Kremer, M. L. *Phys. Chem. Chem. Phys.* **1999**, *1*, 3595-3605.

(31) Pignatello, J. J.; Oliveros, E.; MacKay, A. *Crit. Rev. Environ. Sci. Technol.* **2006**, *36*, 1-84.
(32) Barton, D. H. R.; Doller, D. *Acc. Chem. Res.* **1992**, *25*, 504-512.
(33) Barton, D. H. R.; Gastiger, M. J.; Motherwell, W. B. *J. Chem. Soc., Chem. Commun.* **1983**, 41-43.
(34) Yamazaki, I.; Piette, L. H. *J. Am. Chem. Soc.* **1991**, *113*, 7588-7593.
(35) Løgager, T.; Holcman, J.; Sehested, K.; Pederson, T. *Inorg. Chem.* **1992**, *31*, 3523-3529.
(36) Lloyd, R. V.; Hanna, P. M.; Mason, R. P. *Free Radical Biol. Med.* **1997**, *22*, 885-888.
(37) Burkitt, M. J. *Free Radical Research Communications* **1993**, *18*, 43-57.
(38) Walling, C. *Acc. Chem. Res.* **1998**, *31*, 155-157.
(39) Goldstein, S.; Meyerstein, D. *Acc. Chem. Res.* **1999**, *32*, 547-550.
(40) Bossmann, S. H.; Oliveros, E.; Göb, S.; Siegward, S.; Dahlen, E. P.; Payawan, L., Jr.; Straub, M.; Wörner, M.; Braun, A. M. *J. Phys. Chem. A* **1998**, *102*, 5542-5550.
(41) Pestovsky, O.; Stoian, S.; Bominaar, E. L.; Shan, X.; Münck, E.; Que, L., Jr.; Bakac, A. *Angew. Chem., Int. Ed.* **2005**, *44*, 6871-6874.
(42) Kremer, M. L. *Int. J. Chem. Kinet.* **2006**, *38*, 725-736.
(43) Rudakov, E. S.; Volkova, L. K.; Tret'yakov, V. P.; Zamashchikov, V. V. *Kinet. Catal.* **1982**, *23*, 18-25.
(44) Conocchioli, T. J.; Hamilton, E. J., Jr.; Sutin, N. *J. Am. Chem. Soc.* **1965**, *87*, 926-927.
(45) Walling, C.; El-Taliawi, G. M.; Johnson, R. A. *J. Am. Chem. Soc.* **1974**, *96*, 133-139.
(46) Wink, D. A.; Wink, C. B.; Nims, R. W.; Ford, P. C. *Environ. Health Perspect.* **1994**, *102 (Suppl. 3)*, 11-15.
(47) Paczésniak, T.; Sobkowiak, A. *J. Mol. Catal. A: Chem.* **2003**, *194*, 1-11.
(48) Pastore, G.; Smargiassi, E.; Buda, F. *Phys. Rev. A* **1991**, *44*, 6334-6347.
(49) Laasonen, K.; Sprik, M.; Parrinello, M. *J. Chem. Phys.* **1993**, *99*, 9080-9089.
(50) Sprik, M.; Hutter, J.; Parrinello, M. *J. Chem. Phys.* **1996**, *105*, 1142-1152.
(51) Silvestrelli, P. L.; Bernasconi, M.; Parrinello, M. *Chem. Phys. Lett.* **1997**, *277*, 478-482.
(52) Silvestrelli, P. L.; Parrinello, M. *J. Chem. Phys.* **1999**, *111*, 3572-3580.
(53) Izvekov, S.; Voth, G. A. *J. Chem. Phys.* **2002**, *116*, 10372-10376.
(54) Marx, D.; Sprik, M.; Parrinello, M. *Chem. Phys. Lett.* **1997**, *273*, 360-366.
(55) Grossman, J. C.; Schwegler, E.; Draeger, E. W.; Gygi, F.; Galli, G. *J. Chem. Phys.* **2004**, *120*, 300-311.
(56) Kuo, I. F. W.; Mundy, C. J.; McGrath, M. J.; Siepmann, J. I.; VandeVondele, J.; Sprik, M.; Hutter, J.; Chen, B.; Klein, M. L.; Mohamed, F.; Krack, M.; Parrinello, M. *J. Phys. Chem. B* **2004**, *108*, 12990-12998.
(57) Tangney, P. *J. Chem. Phys.* **2006**, *124*, 044111.
(58) VandeVondele, J.; Mohamed, F.; Krack, M.; Hutter, J.; Sprik, M.; Parrinello, M. *J. Chem. Phys.* **2005**, *122*, 014515.

(59) Mills, R. *J. Phys. Chem.* **1973**, *77*, 685-688.
(60) Amsterdam Density Functional program, Theoretical Chemistry, Vrije Universiteit, Amsterdam, URL: http://www.scm.com.
(61) Baerends, E. J.; Ellis, D. E.; Ros, P. *Chem. Phys.* **1973**, *2*, 41-51.
(62) Fonseca Guerra, C.; Snijders, J. G.; te Velde, G.; Baerends, E. J. *Theor. Chem. Acc.* **1998**, *99*, 391-403.
(63) te Velde, G.; Bickelhaupt, F. M.; van Gisbergen, S. J. A.; Fonseca Guerra, C.; Baerends, E. J.; Snijders, J. G.; T., Z. *J. Comput. Chem.* **2001**, *22*, 931-967.
(64) van Lenthe, E.; Baerends, E. J.; Snijders, J. G. *J. Chem. Phys.* **1994**, *101*, 9783-9792.
(65) Becke, A. *Phys. Rev. A* **1988**, *38*, 3098-3100.
(66) Lee, C.; Yang, W.; Parr, R. G. *Phys. Rev. B* **1988**, *37*, 785-789.
(67) Hummer, G.; Grønbech-Jensen, N.; Neumann, M. *J. Chem. Phys.* **1998**, *109*, 2791-2797.
(68) Hünenberger, P. H. *J. Chem. Phys.* **2002**, *116*, 6880-6897.
(69) Swenson, R. J. *Am. J. Phys.* **1983**, *51*, 940-942.
(70) Kudin, K. N.; Scuseria, G. E. *Phys. Rev. B* **1999**, *61*, 16440-16453.
(71) Jacquemin, D.; André, J. M.; Champagne, B. *J. Chem. Phys.* **1999**, *111*, 5306-5323.
(72) Doll, K.; Dovesi, R.; Orlando, R. *Theor. Chem. Acc.* **2004**, *112*, 394-402.
(73) Marx, D.; Hutter, J. In *Modern Methods and Algorithms for Quantum Chemistry*; Grotendorst, J., Ed.; John von Neumann Institute for Computing: Jülich, 2000; Vol. 1, pp 301-449.
(74) Hamad, S.; Lago, S.; Mejìas, J. A. *J. Phys. Chem. A* **2002**, *106*, 9104-9113.
(75) Kim, K. S.; Kim, H. S.; Jang, J. H.; Kim, H. S.; Mhin, B.-J.; Xie, Y.; Schaefer III, H. F. *J. Chem. Phys.* **1991**, *94*, 2057-2062.
(76) Xie, Y.; Schaefer III, H. F. *J. Chem. Phys.* **1993**, *98*, 8829-8834.
(77) Wang, B.; Hou, H.; Gu, Y. *Chem. Phys. Lett.* **1999**, *303*, 96-100.
(78) Zhou, Z.; Qu, Y.; Fu, A.; Du, B.; He, F.; Gao, H. *Int. J. Quantum Chem.* **2002**, *89*, 550-558.
(79) Cabral do Couto, P.; Guedes, R. C.; Costa Cabral, B. J.; Martinho Simões, J. A. *J. Chem. Phys.* **2003**, *119*, 7344-7355.
(80) Nanayakkara, A. A.; Balint-Kurti, G. G.; Williams, I. H. *J. Phys. Chem.* **1992**, *96*, 3662-3669.
(81) Dubey, M. K.; Mohrschladt, R.; Donahue, N. M.; Anderson, J. G. *J. Phys. Chem. A* **1997**, *101*, 1494-1500.
(82) Hand, M. R.; Rodriquez, C. F.; Williams, I. H.; Balint-Kurti, G. G. *J. Phys. Chem. A* **1998**, *102*, 5958-5966.
(83) Vassilev, P.; Hartnig, C.; Koper, M. T. M.; Frechard, F.; van Santen, R. A. *J. Chem. Phys.* **2001**, *115*, 9815-9820.
(84) Marx, D.; Tuckerman, M.; Hutter, J.; Parrinello, M. *Nature* **1999**, *397*, 601-604.
(85) Geissler, P. L.; Dellago, C.; Chandler, D.; Hutter, J.; Parrinello, M. *Chem. Phys. Lett.* **2000**, *321*, 225-230.

(86) Tuckerman, M.; Laasonen, K.; Sprik, M.; Parrinello, M. *J. Chem. Phys.* **1995**, *103*, 150-161.
(87) Tuckerman, M. E.; Marx, D.; Parrinello, M. *Nature* **2002**, *417*, 925-929.
(88) Trout, B. L.; Parrinello, M. *J. Phys. Chem. B* **1999**, *103*, 7340-7345.
(89) de Grotthuss, C. J. T. *Ann. Chim. (Paris)* **1806**, *LVIII*, 54-74.
(90) Bickelhaupt, F. M.; Diefenbach, A.; de Visser, S. P.; de Koning, L. J.; Nibbering, N. M. M. *J. Phys. Chem. A* **1998**, *102*, 9549-9553.
(91) Sodupe, M.; Bertran, J.; Rodriguez-Santiago, L.; Baerends, E. J. *J. Phys. Chem. A* **1999**, *103*, 166-170.
(92) Tuckerman, M. E.; Chandra, A.; Marx, D. *Acc. Chem. Res.* **2006**, *39*, 151-158.
(93) Khalack, J. M.; Lyubartsev, A. P. *J. Phys. Chem. A* **2005**, *109*, 378-386.
(94) VandeVondele, J.; Sprik, M. *Phys. Chem. Chem. Phys.* **2005**, *7*, 1363-1367.
(95) Meunier, B.; de Visser, S. P.; Shaik, S. *Chem. Rev.* **2004**, *104*, 3947-3980.
(96) Costas, M.; Chen, K.; Que, L., Jr. *Coord. Chem. Rev.* **2000**, *200-202*, 517-544.
(97) Solomon, E. I.; Decker, A.; Lehnert, N. *Proc. Natl. Acad. Sci. USA* **2003**, *100*, 3589-3594.
(98) Que, L., Jr. *J. Biol. Inorg. Chem.* **2004**, *9*, 684-690.
(99) Schöneboom, J. C.; Cohen, S.; Lin, H.; Shaik, S.; Thiel, W. *J. Am. Chem. Soc.* **2004**, *126*, 4017-4034.
(100) Groenhof, A. R.; Swart, M.; Ehlers, A. W.; Lammertsma, K. *J. Phys. Chem. A* **2005**, *109*, 3411-3417.
(101) Bassan, A.; Blomberg, M. R. A.; Borowski, T.; Siegbahn, P. E. M. *J. Inorg. Biochem.* **2006**, *100*, 727-743.
(102) Bassan, A.; Blomberg, M. R. A.; Siegbahn, P. E. M. *Chem. Eur. J.* **2003**, *9*, 4055-4067.
(103) Kaizer, J.; Klinker, E. J.; Oh, N. Y.; Rohde, J.-U.; Song, W. J.; Stubna, A.; Kim, J.; Münck, E.; Nam, W.; Que, L., Jr. *J. Am. Chem. Soc.* **2004**, *126*, 472-473.
(104) van den Berg, T. A.; de Boer, J. W.; Browne, W. R.; Roelfes, G.; Feringa, B. L. *J. Chem. Soc., Chem. Commun.* **2004**, *22*, 2550-2551.
(105) Rohde, J.-U.; Que, L., Jr. *Angew. Chem., Int. Ed.* **2005**, *44*, 2255-2258.
(106) Ensing, B.; Buda, F.; Gribnau, M. C. M.; Baerends, E. J. *J. Am. Chem. Soc.* **2004**, *126*, 4355-4365.
(107) Groves, J. T.; McClusky, G. A. *J. Am. Chem. Soc.* **1976**, *98*, 859-861.
(108) Groves, J. T.; Van Der Puy, M. *J. Am. Chem. Soc.* **1976**, *98*, 5290-5297.
(109) http://www.h2o2.com/applications/industrialwastewater/hcho.html and http://www.h2o2.com/applications/industrialwastewater/fentonsreagent.html.
(110) Shiota, Y.; Yoshizawa, K. *J. Am. Chem. Soc.* **2000**, *122*, 12317-12326.
(111) Yumura, T.; Yoshizawa, K. *Organometallics* **2001**, *20*, 1397-1407.
(112) Yoshizawa, K.; Kagawa, Y. *J. Phys. Chem. A* **2000**, *104*, 9347-9355.
(113) Fiedler, A.; Schröder, D.; Shaik, S.; Schwarz, H. *J. Am. Chem. Soc.* **1994**, *116*, 10734-10741.

(114) Schröder, D.; Schwarz, H.; Shaik, S. In *Structure & Bonding: Metal-oxo and metal-peroxo species in catalytic oxidations*; Meunier, B., Ed.; Springer Verlag: Berlin Heidelberg, 2000; Vol. 97, pp 91-123.
(115) Schröder, D.; Shaik, S.; Schwarz, H. *Acc. Chem. Res.* **2000**, *33*, 139-145.
(116) Harris, N.; Shaik, S.; Schröder, D.; Schwarz, H. *Helv. Chim. Acta* **1999**, *82*, 1784-1797.
(117) Buda, F.; Ensing, B.; Gribnau, M. C. M.; Baerends, E. J. *Chem. Eur. J.* **2003**, *9*, 3436-3444.
(118) Decker, A.; Solomon, E. I. *Curr. Opin. Chem. Biol.* **2005**, *9*, 152-163.
(119) Decker, A.; Rohde, J.-U.; Que, L., Jr.; Solomon, E. I. *J. Am. Chem. Soc.* **2004**, *126*, 5378-5379.
(120) Kumar, D.; Hirao, H.; Que, L., Jr.; Shaik, S. *J. Am. Chem. Soc.* **2005**, *127*, 8026-8027.
(121) Decker, A.; Solomon, E. I. *Angew. Chem., Int. Ed.* **2005**, *44*, 2252-2255.
(122) Decker, A.; Clay, M. D.; Solomon, E. I. *J. Inorg. Biochem.* **2006**, *100*, 697-706.
(123) Ghosh, A.; Tangen, E.; Ryeng, H.; Taylor, P. R. *Eur. J. Inorg. Chem.* **2004**, *2004*, 4555-4560.
(124) Neese, F. *J. Inorg. Biochem.* **2006**, *100*, 716-726.
(125) Jacobsen, F.; Holcman, J.; Sehested, K. *Int. J. Chem. Kinet.* **1998**, *30*, 215-221.
(126) de Jong, G. T.; Geerke, D. P.; Diefenbach, A.; Bickelhaupt, F. M. *Chem. Phys.* **2005**, *313*, 261-270.
(127) Swart, M.; Groenhof, A. R.; Ehlers, A. W.; Lammertsma, K. *J. Phys. Chem. A* **2004**, *108*, 5479-5483.
(128) Fouqueau, A.; Mer, S.; Casida, M. E.; Daku, L. M. L.; Hauser, A.; Mineva, T.; Neese, F. *J. Chem. Phys.* **2004**, *120*, 9473-9486.
(129) Frenkel, D.; Smit, B. *Understanding Molecular Simulation*; ACADEMIC PRESS: San Diego, 1996.
(130) Ensing, B.; Meijer, E. J.; Blöchl, P. E.; Baerends, E. J. *J. Phys. Chem. A* **2001**, *105*, 3300-3310.
(131) Sprik, M.; Ciccotti, G. *J. Chem. Phys.* **1998**, *109*, 7737-7744.
(132) den Otter, W. K.; Briels, W. J. *J. Chem. Phys.* **1998**, *109*, 4139-4146.
(133) Flyvbjerg, H.; Petersen, H. G. *J. Chem. Phys.* **1989**, *91*, 461-466.
(134) Mulliken, R. S. *J. Chem. Phys.* **1955**, *23*, 1833-1840.
(135) Hirshfeld, F. L. *Theor. Chim. Act.* **1977**, *44*, 129-138.
(136) Bickelhaupt, F. M.; van Eikema Hommes, N. J. R.; Fonseca Guerra, C.; Baerends, E. J. *Organometallics* **1996**, *15*, 2923-2931.
(137) Newcomb, M.; Le Tadic-Biadatti, M. H.; Chestney, D. L.; Roberts, E. S.; Hollenberg, P. F. *J. Am. Chem. Soc.* **1995**, *117*, 12085-12091.
(138) Karawajczyk, A.; Buda, F. *J. Biol. Inorg. Chem.* **2005**, *10*, 33-40.
(139) Panov, G. I.; Uriarte, A. K.; Rodkin, M. A.; Sobolev, V. I. *Catal. Today* **1998**, *41*, 365-385.

(140) Malykhin, S.; Zilberberg, I.; Zhidomirov, G. M. *Chem. Phys. Lett.* **2005**, *414*, 434-437.
(141) Bernasconi, L.; Baerends, E. J.; Sprik, M. *J. Phys. Chem. B* **2006**, *110*, 11444-11453.
(142) Klamt, A. *J. Phys. Chem.* **1995**, *99*, 2224-2235.
(143) Eckert, F.; Klamt, A. *AIChE J.* **2002**, *48*, 369-385.
(144) Pye, C. C.; Ziegler, T. *Theor. Chem. Acc.* **1999**, *101*, 396-408.
(145) Bickelhaupt, F. M.; Baerends, E. J. In *Reviews in Computational Chemistry*; Lipkowitz, K. B., Boyd, D. R., Eds.; J. Wiley: New York, 2000; Vol. 15, pp 1-86.
(146) Morokuma, K. *J. Chem. Phys.* **1971**, *55*, 1236-1244.
(147) Kitaura, K.; Morokuma, K. *Int. J. Quantum Chem.* **1976**, *10*, 325-340.
(148) Smith, W. L.; DeWitt, D. L.; Garavito, R. M. *Annu. Rev. Biochem.* **2000**, *69*, 145-182.
(149) Bugg, T. D. H. *Tetrahedron* **2003**, *59*, 7075-7101.
(150) Debrunner, P. G. *Hyperfine Interact.* **1990**, *53*, 21-35.
(151) Rutter, R.; Valentine, M.; Hendrich, M. P.; Hager, L. P.; Debrunner, P. G. *Biochemistry* **1983**, *22*, 4769-4774.
(152) Rutter, R.; Hager, L. P.; Dhonau, H.; Hendrich, M.; Valentine, M.; Debrunner, P. *Biochemistry* **1984**, *23*, 6809-6816.
(153) Schulz, C. E.; Devaney, P. W.; Winkler, H.; Debrunner, P. G.; Doan, N.; Chiang, R.; Rutter, R.; Hager, L. P. *FEBS Lett.* **1979**, *103*, 102-105.
(154) Schulz, C. E.; Rutter, R.; Sage, J. T.; Debrunner, P. G.; Hager, L. P. *Biochemistry* **1984**, *23*, 4743-4754.
(155) Hersleth, H.-P.; Ryde, U.; Rydberg, P.; Görbitz, C. H.; Andersson, K. K. *J. Inorg. Biochem.* **2006**, *100*, 460-476.
(156) Omura, T. *Biochem. Biophys. Res. Com.* **1999**, *266*, 690-698.
(157) Denisov, I. G.; Makris, T. M.; Sligar, S. G.; Schlichtung, I. *Chem. Rev.* **2005**, *105*, 2253-2278.
(158) Shaik, S.; Kumar, D.; de Visser, S. P.; Altun, A.; Thiel, W. *Chem. Rev.* **2005**, *105*, 2279-2328.
(159) Behan, R. K.; Green, M. T. *J. Inorg. Biochem.* **2006**, *100*, 448-459.
(160) Nemukhin, A. V.; Topol, I. A.; Cachau, R. E.; Burt, S. K. *Theor. Chem. Acc.* **2006**, *115*, 348-353.
(161) Feig, A. L.; Lippard, S. J. *Chem. Rev.* **1994**, *94*, 759-805.
(162) Que, L., Jr.; Ho, R. Y. N. *Chem. Rev.* **1996**, *96*, 2607-2624.
(163) Solomon, E. I.; Brunold, T. C.; Davis, M. I.; Kemsley, J. N.; Lee, S.-K.; Lehnert, N.; Neese, F.; Skulan, A. J.; Yang, Y.-S.; Zhou, J. *Chem. Rev.* **2000**, *100*, 235-350.
(164) Price, J. C.; Barr, E. W.; Tirupati, B.; Bollinger, J. M., Jr.; Krebs, C. *Biochemistry* **2003**, *42*, 7497-7508.
(165) Price, J. C.; Barr, E. W.; Glass, T. E.; Krebs, C.; Bollinger, J. M., Jr. *J. Am. Chem. Soc.* **2003**, *125*, 13008-13009.

(166) Proshlyakov, D. A.; Henshaw, T. F.; Monterosso, G. R.; Ryle, M. J.; Hausinger, R. P. *J. Am. Chem. Soc.* **2004**, *126*, 1022-1023.
(167) Riggs-Gelasco, P. J.; Price, J. C.; Guyer, R. B.; Brehm, J. H.; Barr, E. W.; Bollinger, J. M., Jr.; Krebs, C. *J. Am. Chem. Soc.* **2004**, *126*, 8108-8109.
(168) Krebs, C.; Price, J. C.; Baldwin, J.; Saleh, L.; Green, M. T.; Bollinger, J. M., Jr. *Inorg. Chem.* **2005**, *44*, 742-757.
(169) Rohde, J.-U.; In, J.-H.; Lim, M. H.; Brennessel, W. W.; Bukowski, M. R.; Stubna, A.; Münck, E.; Nam, W.; Que, L., Jr. *Science* **2003**, *299*, 1037-1039.
(170) Shan, X.; Que, L., Jr. *J. Inorg. Biochem.* **2006**, *100*, 421-433.
(171) Conradie, M. M.; Conradie, J.; Ghosh, A. *J. Inorg. Biochem.* **2006**, *100*, 620-626.
(172) Klinker, E. J.; Kaizer, J.; Brennessel, W. W.; Woodrum, N. L.; Cramer, C. J.; Que, L., Jr. *Angew. Chem., Int. Ed.* **2005**, *44*, 3690-3694.
(173) Bukowski, M. R.; Koehntop, K. D.; Stubna, A.; Bominaar, E. L.; Halfen, J. A.; Münck, E.; Nam, W.; Que, L., Jr. *Science* **2005**, *310*, 1000-1002.
(174) Shaik, S.; Filatov, M.; Schröder, D.; Schwarz, H. *Chem. Eur. J.* **1998**, *4*, 193-199.
(175) Bassan, A.; Blomberg, M. R. A.; Siegbahn, P. E. M. *Chem. Eur. J.* **2003**, *9*, 106-115.
(176) Schöneboom, J. C.; Neese, F.; Thiel, W. *J. Am. Chem. Soc.* **2005**, *127*, 5840-5853.
(177) Lehnert, N.; Ho, R. Y. N.; Que, L., Jr.; Solomon, E. I. *J. Am. Chem. Soc.* **2001**, *123*, 8271-8290.
(178) Dawson, J. H.; Holm, R. H.; Trudell, J. R.; Barth, G.; Linder, R. E.; Bunnenberg, E.; Djerassi, C.; Tang, S. C. *J. Am. Chem. Soc.* **1976**, *98*, 3707-3709.
(179) Dawson, J. H.; Sono, M. *Chem. Rev.* **1987**, *87*, 1255-1276.
(180) Dawson, J. H. *Science* **1988**, *240*, 433-439.
(181) Sono, M.; Roach, M. P.; Coulter, E. D.; Dawson, J. H. *Chem. Rev.* **1996**, *96*, 2841-2888.
(182) Makris, T. M.; von Koenig, K.; Schlichtung, I.; Sligar, S. G. *J. Inorg. Biochem.* **2006**, *100*, 507-518.
(183) Guallar, V.; Friesner, R. A. *J. Am. Chem. Soc.* **2004**, *126*, 8501-8508.
(184) Altun, A.; Guallar, V.; Friesner, R. A.; Shaik, S.; Thiel, W. *J. Am. Chem. Soc.* **2006**, *128*, 3924-3925.
(185) Limberg, C. *Angew. Chem., Int. Ed.* **2003**, *42*, 5932-5954.
(186) Sastri, C. V.; Park, M. J.; Ohta, T.; Jackson, T. A.; Stubna, A.; Seo, M. S.; Lee, J.; Kim, J.; Kitagawa, T.; Münck, E.; Que, L., Jr.; Nam, W. *J. Am. Chem. Soc.* **2005**, *127*, 12494-12495.
(187) Kamachi, T.; Kouno, T.; Nam, W.; Yoshizawa, K. *J. Inorg. Biochem.* **2006**, *100*, 751-754.
(188) Fouqueau, A.; Casida, M. E.; Daku, L. M. L.; Hauser, A.; Neese, F. *J. Chem. Phys.* **2005**, *122*, 044110.
(189) Handy, N. C.; Cohen, A. J. *Mol. Phys.* **2001**, *99*, 403-412.

(190) Perdew, J. P.; Burke, K.; Ernzerhof, M. *Phys. Rev. Lett.* **1996**, *77*, 3865-3868.
(191) Groves, J. T.; Van Der Puy, M. *J. Am. Chem. Soc.* **1974**, *96*, 5274-5275.
(192) Mizuta, T.; Wang, J.; Miyoshi, K. *Inorg. Chim. Act.* **1995**, *230*, 119-125.
(193) Seibig, S.; van Eldik, R. *Inorg. Chem.* **1997**, *36*, 4115-4120.
(194) Bernasconi, L.; Baerends, E. J. *Eur. J. Inorg. Chem.* **2008**, *In press.*